Frequency Domain Based Analysis and Design of Norm-Optimal Iterative Learning Control

by

Xinyi Ge

A dissertation submitted in partial fulfillment
of the requirements for the degree of
Doctor of Philosophy
(Mechanical Engineering)
in The University of Michigan
2017

Doctoral Committee:

Professor Jeffrey L. Stein, Co-Chair
Dr. Tulga Ersal, Co-Chair
Associate Professor Brent Gillespie
Professor Jing Sun

Xinyi Ge

gexinyi@umich.edu

ORCID iD: 0000-0002-4005-4252

ACKNOWLEDGEMENTS

Foremost, I would like to express my sincere gratitude to my advisors, Prof. Jeffrey L. Stein and Dr. Tulga Ersal. Without their excellent guidance, constant support and remarkable patience, I don't think I would ever have finished this work. I am honored to have been their student and deeply grateful for all I have learned from them.

Besides my advisors, I also want to convey my warm and sincere thanks to the rest of my committee members, Prof. Brent Gillespie and Prof. Jing Sun, for their insightful comments and valuable suggestions towards my research. I believe that their insightful feedbacks have led this dissertation to be more thorough and complete.

I also wish to express my gratitude to my fellow lab mates in for the stimulating discussions and for all the fun we have had along my Ph.D journey.

I also would like to thank all my friends in my life. I value their friendship very much and it is their support all the way long that has brought where I am today. Thank you all very much!

Finally, I must express my very profound gratitude to my parents and to my fiancée for providing me with unfailing support and continuous encouragement throughout my years of study and through the process of researching and writing this thesis. This accomplishment would not have been possible without them. Thank you and I always love you!

TABLE OF CONTENTS

LIST OF FIGURES

Figure

ABSTRACT

Frequency Domain Based Analysis and Design of Norm-Optimal Iterative Learning Control

by

Xinyi Ge

Co-Chairs: Jeffrey L. Stein and Tulga Ersal

In this thesis, novel frequency domain based analysis and design methods on Norm-Optimal Iterative Learning Control (NO-ILC) are developed for Single-Input-Single-Output (SISO) Linear Time Invariant (LTI) systems. Modeling errors in general degrade the convergence performance of NO-ILC and hence ensuring Robust Monotonic Convergence (RMC) against model uncertainties is important. Although the robustness of NO-ILC has been studied in the literature, determining the allowable range of modeling errors for a given NO-ILC design is still an open research question. To fill this gap, a frequency domain analysis with a multiplicity formulation of model uncertainty is developed in this work to quantify and visualize the allowable modeling errors. Compared with the traditional formulation, the proposed new uncertainty formulation provides a less conservative representation of the allowable model uncertainty range by taking additional phase information into account and thus allows for a more complete evaluation of the robustness of NO-ILC. The analysis also clarifies how the RMC region changes as a function of NO-ILC weighting terms and therefore leads to several frequency domain design tools to achieve RMC for given model un-

certainties. Along with this frequency domain analysis, rather than some qualitative understanding in the literature, an equation quantitatively characterizing the fundamental trade-off of NO-ILC with respect to robustness, convergence speed and steady state error at each frequency is presented, which motivates the proposed loop-shaping like design methods for NO-ILC to achieve different performance requirements at various frequencies. The proposed analysis also demonstrates that NO-ILC is the optimal solution for general LTI ILC updating laws in the scope of balancing the trade-off between robustness, convergence speed and steady state error.

CHAPTER I

Introduction

1.1 Brief Introduction to Iterative Learning Control

The concept of Iterative Learning Control (ILC) can be attributed to a learning process over a repeated motion. For instance, a shooting athlete aims to shoot the center of the target but the initial attempt is not that satisfying as shown in Fig. 1.1. The athlete learns from this bad result and adjusts the shooting angle so that the next attempt gives a better score. The same learning process repeats every time the athlete makes an attempt and eventually the athlete is able to find the best shooting angle that makes the bullet go right into the center of the target.

Similarly, ILC is a control strategy to improve the tracking performance in systems that repeat the same operation many times. Using the tracking error and control input from the previous iterations of the repeated motion, ILC generates the feed-forward control signal for the subsequent iterations. In the literature, ILC is often interpreted as feedback control in the iteration domain due to the fact that learning controller uses the information from past trials. The standard progression in the tracking error and control input signals over several iterations with the use of ILC is shown in Fig. 1.2. Before the start of each iteration, the ILC learning algorithms use the tracking error and control input signals from previous iterations to generate an updated control input signal for the current iteration to improve system performance. Ideally over

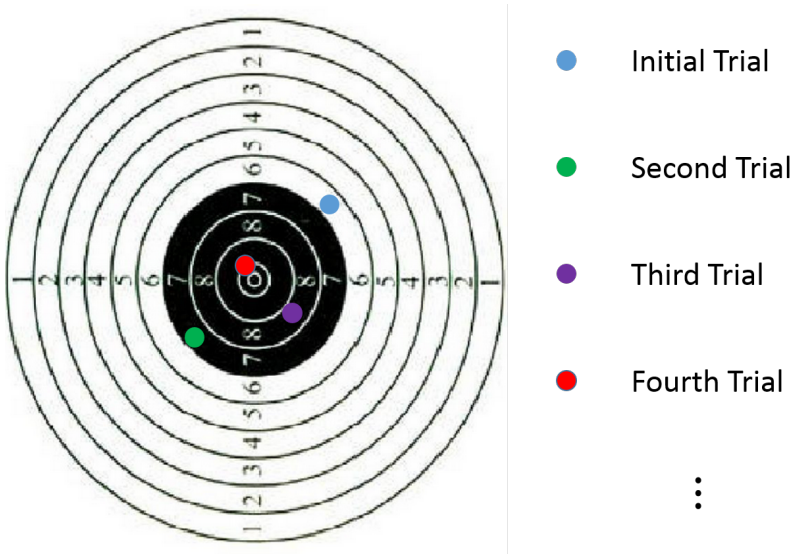

Figure 1.1: Shooting athlete can improve shooting accuracy by repetitive practice

several iterations, this feed-forward control input is optimized such that the tracking error is minimized.

1.2 An Overview of ILC Literature

Since the initial proposition of ILC (*Arimoto et al.*, 1984), a lot of theoretical developments and application based researches have been published in the literature. ILC has been successfully applied in areas where repetitive motions show up naturally, for example, robotics (*Arimoto et al.*, 1984; *Oh et al.*, 1988; *Norrlof*, 2002; *Tayebi*, 2004; *Bouakrif et al.*, 2013), manufacturing (*Bristow and Alleyne*, 2006; *Mishra et al.*, 2007; *Barton and Alleyne*, 2008; *De Roover and Bosgra*, 2000; *Sahoo et al.*, 2007) and chemical processes (*Lee et al.*, 2000; *Gorinevsky*, 2002). Recently, it has also found applications in network-integrated systems for the purpose of eliminating communication delays, e.g., in network control systems (*Pan et al.*, 2006; *Liu et al.*, 2009a) and networked hardware-in-the-loop simulations (*Ersal et al.*, 2014; *Ge et al.*, 2014).

After more than 30 years of development, several books (*Ahn et al.*, 2007c; *Bien and Xu*, 2012; *Xu and Tan*, 2003; *Xu et al.*, 2007; *Owens*, 2016) and survey papers

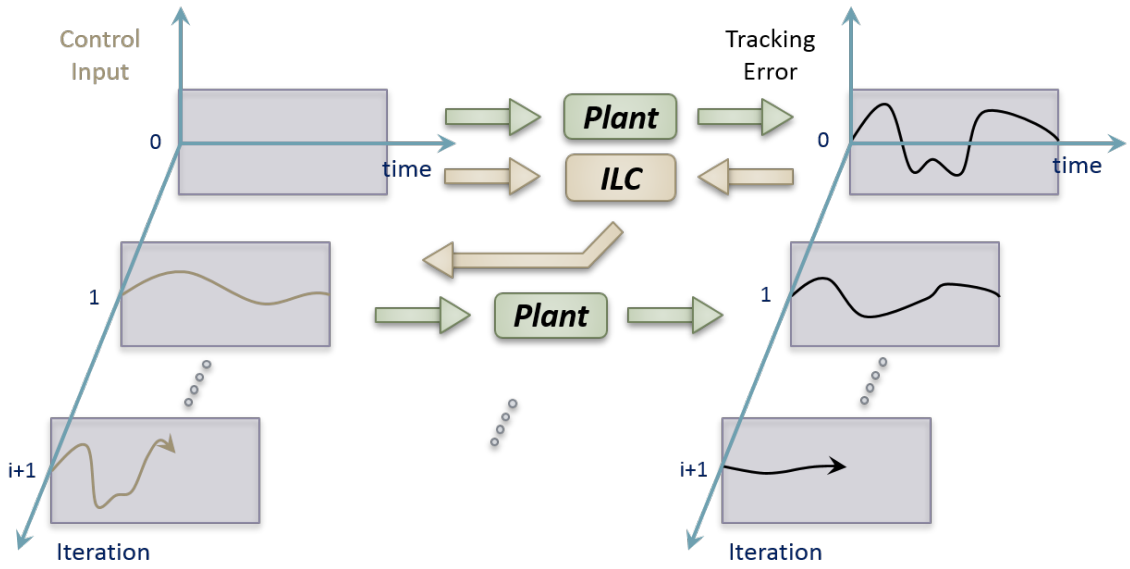

Figure 1.2: A standard progression in the error and control signal over several iterations with the use of ILC

(*Bristow et al.*, 2006; *Ahn et al.*, 2007a; *Xu*, 2011; *Li et al.*, 2013; *Wang et al.*, 2009; *Lee and Lee*, 2007; *Longman*, 2000), focusing on different aspect of ILC, have been published, which are recommended materials as a starting point if one is particularly interested in a certain aspect of ILC.

The inherent assumptions in ILC are the invariance of the plant dynamics (e.g., the initial condition, system parameters and exogenous disturbances are iteration invariant) and the repeatability of the control task in iteration domain. The relaxations of these assumptions have been explored in the ILC literature. For example, the relaxation of iteration-invariant tracking trajectory assumption can be found in (*Xu and Xu*, 2004; *Chi et al.*, 2008; *Chien et al.*, 2008; *Gao and Mishra*, 2014; *Altin and Barton*, 2015; *Van Zundert et al.*, 2015). The handling of initial condition shift problem in ILC is explored in (*Xu and Yan*, 2005; *Sun and Wang*, 2001, 2003; *Chi et al.*, 2008). The non-repetitiveness of disturbance issue has also be explored in (*Chen and Moore*, 2002b; *Heinzinger et al.*, 1992). The issue of iteration-varying system parameters has also attracted a lot of attention for researchers and adaptive

ILC and high-order internal model ILC are common and effective methods to deal with this issue (*Yin et al.*, 2010; *Chien and Yao*, 2004; *Choi and Lee*, 2000; *French and Rogers*, 2000).

Even though a large portion of the work in the ILC literature explores the first-order ILC algorithms, (i.e., ILC updating laws that use input and tracking information from one iteration before), high-order ILC algorithms (i.e., ILC updating laws that use input and tracking information from more than one iterations before) have also attracted a lot of interests in the ILC community. By incorporating more information from previous iterations, the high-order ILC has the potential to better address the stochastic and non-repetitive factors (*Bien and Huh*, 1989; *Chen et al.*, 1998; *Moore and Chen*, 2002; *Phan and Longman*, 2002; *Norrlof and Gunnarsson*, 2002b; *Owens and Feng*, 2006; *Hatonen et al.*, 2006).

Most ILC research is done in temporal domain, however, recently for specific robotics and manufacturing applications, spatial ILC has become an active research area to address the spatial behavior of the system (*Bristow and Alleyne*, 2006; *Sahoo et al.*, 2007; *Moore et al.*, 2007; *Cichy et al.*, 2011).

In terms of handling system types, ILC can be divided into two categories, i.e., ILC for nonlinear systems and ILC for linear systems.

For nonlinear systems, the ILC problems in general can be classified into two categories depending on four major types (*Xu*, 2011): information availability, system types, nonlinearities, design and analysis tools. The first category generally refers to linear ILC design for globally Lipschitz continuous systems, in which output tracking is the control objective. In this case, the system output information is available and the relative degree is assumed to be zero, and ILC can be formulated into a contraction mapping problem (*Xu*, 1997; *Wang*, 1998; *Liu et al.*, 2009b; *Yin et al.*, 2010; *Bouakrif*, 2011). For the second category, nonlinear ILC updating laws are applied to locally Lipschitz continuous systems, in which state tracking is the control

objective. The system state dynamics are indispensable in ILC design and analysis, where Lyapunov approach or composite energy function approach is often used. In this case, adaptive ILC appears as a common ILC design methodology (*Chien and Yao*, 2004; *Choi and Lee*, 2000; *French and Rogers*, 2000; *Tayebi*, 2004; *Wang et al.*, 2004).

In general, three different system representations are used for the ILC analysis and design problems for linear systems. The 2D system based ILC analysis and design method uses the state space representation. One important feature of the 2D system based approach is that the ILC updating law uses not only the control input and tracking error from previous iterations but also the state information from the previous iteration. Some of the 2D system based ILC analysis and design methods can be found in (*Kurek and Zaremba*, 1993; *Owens et al.*, 2000; *Shi et al.*, 2005; *Hladowski et al.*, 2010; *Cichy et al.*, 2014). On the other hand, ILC analysis and design using the lifted domain system representation or transfer function representation do not require state information. Lifted domain representation is widely used in the ILC literature, in which case the system input and output can be 'stacked' into vectors and plant can be 'lifted' into a matrix composing of system Markov parameters. Fruitful results, with regards to convergence and robustness property of NO-ILC, have been published using the lifted domain representation (*Ahn et al.*, 2007b; *Madady*, 2008; *Van De Wijdeven et al.*, 2009; *Owens and Feng*, 2006; *Owens and Daley*, 2008). The major advantages of using the lifted representation in analyzing ILC are that the convergence analysis can be easily formulated into a matrix contraction mapping problem and the analysis can be easily extended to Linear Time Varying (LTV) systems. Using the transfer function representation, ILC can be designed and analyzed in the frequency domain. The advantages of using this system representation are not only due to the fact that the analysis and design tools can reveal the frequency domain properties of the ILC system (*Norrlof and Gunnarsson*, 2002a; *Gunnarsson and Norrlof*, 2001;

Norrlof and Gunnarsson, 2005) but also due to the fact that some classical feedback design methodologies can be leveraged into the ILC design, e.g., plant inversion (*Harte et al.*, 2005), H_∞ and μ synthesis (*De Roover and Bosgra*, 2000).

1.3 Focus of This Work

This work focuses on the frequency domain analysis and design on a particular ILC algorithm, Norm-Optimal Iterative Learning Control (NO-ILC), for Linear Time Invariant (LTI) systems. Under the scope of LTI ILC on LTI systems, ILC design problems can mainly be classified into four categories (*Bristow et al.*, 2006): (1) PD-type learning, (2) learning based on plant inversion, (3) H_∞ based methods, (4) quadratically optimal designs.

For the first category, PD-type learning (*Chen and Moore*, 2002a; *Bristow et al.*, 2006) in the iteration domain is analogous to PD control in the time domain and is one of the widely used learning algorithms due to its ease of implementation. However, it requires ad-hoc tuning and even though it can ensure asymptotic stability, its transient performance may be unacceptable (*Bristow et al.*, 2006). For the second category, learning based on plant inversion (*Bristow et al.*, 2006; *Harte et al.*, 2005) uses the inversion of the system model to update the ILC input sequence, providing a systematic design. However, plant inversion may not work for non-minimum phase systems. For the third category, H_∞ methods (*Bristow et al.*, 2006; *De Roover and Bosgra*, 2000) offer a systematic approach to ILC design. However, all the above mentioned design methodologies are causal and thus do not take full advantage of the non-causal learning potential of the ILC paradigm (*Donkers et al.*, 2008; *Norrlof and Gunnarsson*, 2005; *Goldsmith*, 2002). For causal ILC updating laws, it has been reported in the literature that there exist equivalent feedback realizations for causal ILC designs (*Goldsmith*, 2002), therefore causal ILC updating laws are subject to the fundamental limitations of feedback, i.e., the water-bed effect (*Freudenberg and*

Looze, 1985).

For the last category, the learning functions, so called NO-ILC, are designed in the lifted system representation to minimize a quadratic next-iteration cost criterion. NO-ILC realizes non-causal control by minimizing a cost criterion similar to the traditional linear quadratic control concept. Due to its non-causal nature, NO-ILC potentially has the ability to bypass the water-bed limitation and, therefore, is gaining attention as a powerful approach. Recently, it has recently been applied to many areas, including, but not limited to, chemical processes (*Lee et al.*, 2000), manufacturing (*Barton and Alleyne*, 2011; *Barton et al.*, 2011; *Janssens et al.*, 2013), and networked hardware-in-the-loop simulation (*Ge et al.*, 2014). Recognizing its advantages, this thesis focuses on NO-ILC, especially on its frequency domain properties, and develops novel frequency domain based design approaches.

In NO-ILC the learning law is synthesized via minimization of a quadratic cost function, which was originally formulated by Amann (*Amann et al.*, 1996) and Lee (*Lee et al.*, 1996) for the single-input-single-output (SISO) LTI case as shown below:

$$J_{i+1}\left(\mathbf{u}_{i+1}\right) = \mathbf{e}_{i+1}^{T} Q \mathbf{e}_{i+1} + \left(\mathbf{u}_{i+1} - \mathbf{u}_{i}\right)^{T} R \left(\mathbf{u}_{i+1} - \mathbf{u}_{i}\right) + \mathbf{u}_{i+1}^{T} S \mathbf{u}_{i+1} \tag{1.1}$$

The variable $\mathbf{e}_i \in \mathbb{R}^N$ denotes the tracking error for the i_{th} iteration. $Q = \mathbf{W}_1^T \mathbf{W}_1$, $R = \mathbf{W}_2^T \mathbf{W}_2$ and $S = \mathbf{W}_3^T \mathbf{W}_3$ are positive semi-definite weighting matrices. A common choice for these weighting matrices is to use diagonal matrices, as discussed in Section 4.1 in Chapter IV. Non-diagonal weighting matrices can be used to enhance the performance of NO-ILC, which will be addressed in Section 4.2 in Chapter IV. The first term on the right side of Eq. (1.1) penalizes the tracking error for the next iteration; the second term penalizes the input difference between the next and current iterations; and the third term penalizes the input efforts for the next iteration. J_{i+1} is the total cost to be minimized and is a function of the input sequence for the iteration

$i+1$.

With the system perfectly known, asymptotic stability and monotonic stability can be established as discussed in (*Amann et al.*, 1996; *Lee et al.*, 1996; *Norrlof and Gunnarsson*, 2002a). Asymptotic stability guarantees the asymptotic convergence of the tracking error, but does not provide any limits on the tracking error during the transient phase in the iteration domain. In fact, the tracking error in this transient phase can be large enough to make a practical implementation infeasible (*Bristow et al.*, 2006). Therefore, monotonic convergence is often preferred to guarantee that the tracking error will reduce with each iteration, thereby avoiding large transient errors. In practice, a modeling error always exists, i.e., the model used to build the NO-ILC updating law is always different from the real system due to, for example, unmodeled dynamics. This modeling error can be estimated or identified to be within a certain range, but is in general not known exactly. Since NO-ILC is a model-based approach, modeling errors can degrade its performance. Therefore, the robustness of NO-ILC is an important topic and is one of the main focuses of this work.

Robustness of ILC algorithms in general has been subject to prior research. In (*Ahn et al.*, 2005, 2007b), the Schur stability radius in designing a general robust ILC has been investigated, assuming there exist interval uncertainties in the Markov parameters of the systems. However, this approach leads to conservative results with respect to the stipulated model uncertainty. In (*Harte et al.*, 2005; *Owens et al.*, 2009), the Robust Monotonic Convergence (RMC) of inverse-based ILC and gradient-based ILC has been studied. However, these algorithms are only special forms of NO-ILC and can only handle positive real modeling errors due to the absence of Q-filters. In (*Van De Wijdeven et al.*, 2009), the RMC of finite time interval ILC is investigated. In particular, μ analysis is adopted to check the RMC condition for ILC with an uncertainty formulation. For a given upper bound on the model uncertainty and a given ILC design, this tool provides a means for checking RMC.

For the specific context of NO-ILC, the RMC has been studied to a certain degree in the literature (*Donkers et al.*, 2008; *Gorinevsky*, 2002; *Van De Wijdeven et al.*, 2009; *Owens*, 2016). Specifically, RMC criteria in both time and frequency domain have been derived, based on which numerous design and tuning approaches have been proposed. However, determining the allowable range of modeling error for a given NO-ILC design is not a research question that has been fully answered. Even though the existing tools can be utilized in an attempt to answer this question, this would not only require a trial-and-error process, but also give conservative evaluations of the RMC range. This would lead to a conservative filter design for NO-ILC in terms of convergence speed and steady state tracking error; i.e., convergence speed may be unnecessarily slow or an unnecessary steady state tracking error may be introduced. Therefore, it is important to know how the range of the allowable modeling error is affected by the weighting terms in the cost function of NO-ILC to enable more aggressive designs against modeling uncertainties.

Besides robustness, as mentioned above, convergence speed and steady state error are also important concerns since a too robust solution leading to poor convergence speed or unnecessary steady state error is not preferred. For the convergence speed, inverting the plant, i.e., setting $R = 0$ and $S = 0$ in Eq. (1.1), in general achieves the fastest convergence speed, since theoretically the ILC output convergences after one iteration of learning. However, this method is usually not feasible due to the existence of model uncertainties as well as the non-minimum phase nature of some systems.

As for the steady state error, the trade-off between steady state error and robustness has been addressed in the literature qualitatively: increasing S provides additional robustness at the expense of a larger steady state error (*Donkers et al.*, 2008; *Gorinevsky*, 2002). However, due to the specific uncertainty formulation used, it has been reported that R does not affect the robustness of NO-ILC (*Donkers et al.*,

2008; *Gorinevsky*, 2002).

The work reviewed so far focuses on the problem of analyzing the RMC, convergence speed, or steady state error of NO-ILC for a given design of weighting matrices. The dual problem, i.e., the design and tuning of NO-ILC weighting matrices for a desired level of robustness, convergence speed, or steady state error has also been subject to prior investigation. However, majority of the design and tuning tools use diagonal matrices (*Gunnarsson and Norrlof*, 2001; *Bristow*, 2008; *Lee et al.*, 2000; *Donkers et al.*, 2008), which limits the design freedom in adjusting the trade-off between robustness, convergence speed, and steady state error. In (*Gorinevsky*, 2002), a loop shaping technique is proposed to address the design of a non-diagonal S matrix to balance the robustness and steady state error trade-off. Other design and tuning methods using time varying weighting matrices have also been proposed (*Barton and Alleyne*, 2011).

In light of this literature review, several gaps are identified.

- An analysis tool that completely evaluates the allowable model uncertainties against the NO-ILC weighting matrices has not been fully developed.
- A design technique that allows for the design of NO-ILC according to different robustness, convergence speed and steady state error requirements at different frequencies does not yet exist.
- An analytical equation that quantitatively characterizes the fundamental trade-off between robustness, convergence speed and steady state error has not yet been established.

The objective of this research is to provide fundamental analysis tools for the frequency domain properties of NO-ILC, which leads to novel design methodologies for NO-ILC to adjust the trade-off between robustness, convergence speed and steady state error at different frequencies.

1.4 Thesis Contributions and Outline

Through an infinite time horizon analysis, the main contributions of this work can be summarized as follows:

- This work presents a new model uncertainty formulation for NO-ILC. Unlike the conventional uncertainty formulation, which leads to the conclusion that R does not affect the robustness (*Donkers et al.*, 2008; *Gorinevsky*, 2002), the new formulation used in this work yields that the robustness is affected by both R and S but in different manners.

- Based on the above uncertainty formulation, this work both mathematically and graphically presents how the weighting terms in the cost function affect the robustness of NO-ILC. This leads to several new graphical design methodologies for the weighting matrices to achieve the RMC requirement.

- An analytical equation is derived to quantitatively characterize the fundamental trade-off between robustness, convergence speed and steady state error of NO-ILC in frequency domain. This equation can be helpful during the design process to satisfy a desired robustness requirement while ensuring fast convergence and small steady state error at different frequencies. This equation also reveals the optimality of NO-ILC among general ILC updating laws in the scope of LTI systems.

- Based on the analysis on allowable model uncertainty and fundamental trade-off for NO-ILC, two optimization based formulations are proposed to systematically design the weighting matrices for NO-ILC, which eliminate the manual tuning process and avoid unnecessarily conservative designs.

The rest of this thesis is organized as follows: Chapter II reviews the background of NO-ILC, including different system representations, derivation of the NO-ILC up-

dating law, definition of monotonic convergence and formulation of modeling error. Chapter III discusses the proposed model uncertainty formulation and how this uncertainty is visualized on the Bode and Nyquist plots. Then the frequency domain Robust Monotonic Convergence (RMC) criterion is revisited and the its validity towards infinite time horizon is addressed. Chapter IV presents two novel RMC analysis and design tools for NO-ILC, one with diagonal weighting matrices design and the other one with frequency dependent weighting matrices design. Both analysis methods offer graphical interpretations of the allowable model uncertainty region on the Nyquist plot and lead to novel design guidelines. Chapter V develops an analytical equation that characterizes the fundamental trade-off of NO-ILC between robustness, convergence speed and steady state error at each frequency. In addition, the chapter demonstrates that NO-ILC is the optimal solution under the scope of general LTI ILC updating laws for LTI systems in terms addressing the trade-off between robustness, convergence speed and steady state error at each frequency. Chapter VI presents two different formulations for the design of NO-ILC weighting matrices as an optimization problem to eliminate the manual tuning process and avoid unnecessarily conservative designs. Chapter VII summarizes the contributions of this thesis and lays out several potential future research directions.

CHAPTER II

Background of NO-ILC

In this chapter, background of NO-ILC is reviewed. First, three different system realizations and the transformations between them are presented. Next, the derivation of the NO-ILC updating law in the lifted domain is reviewed. Then, monotonic convergence and modeling error are discussed. Finally, the frequency domain NO-ILC updating law is presented.

2.1 System Representation

Consider a discrete SISO LTI system with the following state-space realization:

$$\begin{aligned} x_i(t+1) &= Ax_i(t) + Bu_i(t) \\ y_i(t) &= Cx_i(t) + Du_i(t) \end{aligned} \tag{2.1}$$

The matrices A, B, C, D are assumed to be time and iteration invariant. The variables $i \in [0, k]$ and $t \in [0, N-1]$ denote the iteration and time index, respectively, with N being the number of time steps in each iteration. The state variables, inputs and outputs are given by $x_i(t) \in \mathbb{R}^n$, $u_i(t) \in \mathbb{R}$, $y_i(t) \in \mathbb{R}$, respectively, where n denotes the number of state variables.

Beside the state-space realization, the transfer function realization can also be

used to represent a LTI system:

$$y_i(z) = G(z)u_i(z) + d(z) \tag{2.2}$$

Here, $y_i(z)$ and $u_i(z)$ are the z-transforms of the control output and input of the system, respectively. $G(z)$ is a rational transfer function and is equal to $C(zI - A)^{-1}B + D$. $d(z)$ is the z-transform of the free response.

In the ILC literature, the lifted representation has also been widely used. In this form, the control input and control output relationship can be re-written as

$$\mathbf{y}_i = \mathbf{G}\mathbf{u}_i + \mathbf{d} \tag{2.3}$$

Here, $\mathbf{d} = \begin{bmatrix} C; & CA; & \ldots; & CA^{N-1} \end{bmatrix} x(0)$. The initial condition $x(0)$ is assumed to be iteration invariant and $\mathbf{G} \in \mathbb{R}^{N \times N}$ is the lifted-form plant matrix composed of the Markov parameters, which relates the lifted inputs $\mathbf{u}_i \in \mathbb{R}^N$ to the lifted outputs $\mathbf{y}_i \in \mathbb{R}^N$

$$\begin{aligned} \mathbf{y}_i &= \begin{bmatrix} y_i(0) & \ldots & y_i(N-1) \end{bmatrix}^T \\ \mathbf{u}_i &= \begin{bmatrix} u_i(0) & \ldots & u_i(N-1) \end{bmatrix}^T \\ \mathbf{G} &= \begin{bmatrix} h_0 & 0 & 0 & 0 \\ h_1 & \ddots & 0 & 0 \\ \vdots & h_1 & \ddots & 0 \\ h_{N-1} & \cdots & h_1 & h_0 \end{bmatrix} \end{aligned} \tag{2.4}$$

where h denotes the impulse response of the system. Note that if the system relative degree is m, $h_0 = \ldots = h_{m-1} = 0$.

Note that the above three realizations are equivalent. One can easily transfer one realization into another one. Depending on the kind of analysis to be performed, one realization can be more convenient than the other two. The following section derives the NO-ILC updating law using the lifted domain representation.

2.2 Derivation of NO-ILC Updating Law

The control goal of NO-ILC is to find the input sequence so that the total cost shown in Eq. (1.1) is minimized. This can be done by setting $\frac{\partial J_i+1}{\partial \mathbf{u}_i+1} = 0$, which translates to the following updating law:

$$\mathbf{u}_{i+1} = \mathcal{Q}\mathbf{u}_i + \mathcal{L}\mathbf{e}_i \tag{2.5}$$

where the so-called Q-filter $\mathcal{Q} \in \mathbb{R}^{N\times N}$ and the learning gain $\mathcal{L} \in \mathbb{R}^{N\times N}$ are given by (*Amann et al.*, 1996; *Lee et al.*, 1996)

$$\begin{aligned} \mathcal{Q} &= (\mathbf{G}_o^T Q \mathbf{G}_o + R + S)^{-1}(\mathbf{G}_o^T Q \mathbf{G}_o + R) \\ \mathcal{L} &= (\mathbf{G}_o^T Q \mathbf{G}_o + R + S)^{-1}\mathbf{G}_o^T Q \end{aligned} \tag{2.6}$$

where $\mathbf{G}_o \in \mathbb{R}^{N\times N}$ is the lifted domain representation of the nominal plant. Weighting matrices Q, R and S not only provide the design freedom to ensure convergence of the NO-ILC in the presence of plant uncertainties but also affect the convergence speed and steady state tracking error performance of NO-ILC, which are addressed in later chapters.

2.3 Monotonic Convergence

One property of interest is the monotonic convergence, i.e., the tracking performance is improved every time the experiment is repeated. Monotonic convergence can be analyzed from the tracking error dynamics in the iteration domain:

$$\begin{aligned} \mathbf{e}_{i+1} &= \mathbf{y}_d - \mathbf{y}_{i+1} = \mathbf{y}_d - \mathbf{G}\mathbf{u}_{i+1} = \mathbf{y}_d - \mathbf{G}\left(\mathcal{Q}\mathbf{u}_i + \mathcal{L}\mathbf{e}_i\right) \\ &= \mathbf{y}_d - \mathbf{G}\mathcal{Q}\mathbf{G}^{-1}\mathbf{G}\mathbf{u}_i - \mathbf{G}\mathcal{L}\mathbf{e}_i \\ &= \mathbf{y}_d - \mathbf{G}\mathcal{Q}\mathbf{G}^{-1}\left(\mathbf{y}_d - \mathbf{e}_i\right) - \mathbf{G}\mathcal{L}\mathbf{e}_i \end{aligned} \tag{2.7}$$

Here, $\mathbf{y}_d$ is the lifted representation of the desired output. Let $\mathbf{e}_\infty$ denotes the tracking error when the ILC has converged. The following equation can be obtained:

$$\mathbf{e}_{i+1} - \mathbf{e}_\infty = \left(\mathbf{G}\mathcal{Q}\mathbf{G}^{-1} - \mathbf{G}\mathcal{L}\right)(\mathbf{e}_i - \mathbf{e}_\infty) \tag{2.8}$$

with

$$\mathbf{e}_\infty = \left(I - \mathbf{G}\mathcal{Q}\mathbf{G}^{-1} + \mathbf{G}\mathcal{L}\right)^{-1}\left(I - \mathbf{G}\mathcal{Q}\mathbf{G}^{-1}\right) \tag{2.9}$$

In analyzing monotonic convergence, Euclidean norm is often used, i.e., $\|\mathbf{e}_{i+1} - \mathbf{e}_\infty\|_2 < \|\mathbf{e}_i - \mathbf{e}_\infty\|_2$, which leads to the following criterion:

$$\|\mathbf{G}\mathcal{Q}\mathbf{G}^{-1} - \mathbf{G}\mathcal{L}\|_2 < 1 \tag{2.10}$$

Note that the presence of $\mathbf{G}^{-1}$ adds difficulty to the analysis when dealing with non-minimum phase systems since their inverses do not exist. In order to avoid this technical difficulty, monotonic convergence is typically analyzed from the input side (*Van De Wijdeven et al.*, 2009). Following similar derivation steps, one can obtain the input difference dynamics in the iteration domain:

$$\mathbf{u}_{i+1} - \mathbf{u}_\infty = (\mathcal{Q} - \mathcal{L}\mathbf{G})(\mathbf{u}_i - \mathbf{u}_\infty) \tag{2.11}$$

where

$$\mathbf{u}_\infty = (I - \mathcal{Q} + \mathcal{L}\mathbf{G})^{-1}\mathcal{L}\mathbf{G}\mathbf{u}_d \tag{2.12}$$

Here, $\mathbf{u}_d$ and $\mathbf{u}_\infty$ respectively denote the lifted representations of the input sequence that achieves perfect tracking and the input sequence to which the ILC algorithm finally converges. In the rest of this thesis, all monotonic convergence analysis is performed from the input the side. The definition of monotonic convergence is given as follows:

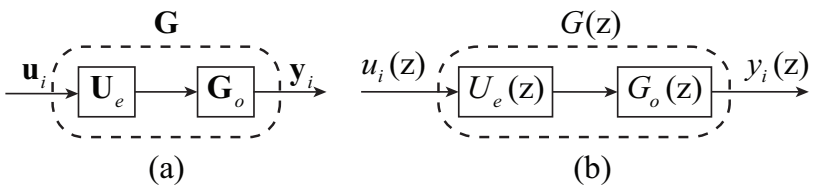

Figure 2.1: Formulation of modeling error in the (a) time and (b) frequency domain

Definition II.1. The ILC system is monotonic convergent from the input side if $\|\mathbf{u}_{i+1} - \mathbf{u}_\infty\|_2 < \|\mathbf{u}_i - \mathbf{u}_\infty\|_2$ for all $i \in [1, k]$ and for any desired output trajectory $\mathbf{y}_d$.

Therefore, the necessary and sufficient condition for monotonic convergence from the input side naturally follows:

$$\|\mathcal{Q} - \mathcal{L}\mathbf{G}\|_2 < 1 \tag{2.13}$$

2.4 Modeling Error

In a real control application, the exact lifted-form plant matrix, $\mathbf{G}$, is always unknown due to some modeling error. The available information is the nominal plant, $\mathbf{G}_o$, and possibly the range of the modeling error. To investigate the robustness of the NO-ILC algorithm, modeling error is incorporated as shown in Fig. 2.1 (*Owens et al.*, 2009; *Harte et al.*, 2005).

Proposition II.2. *Both $\boldsymbol{U}_e$ and $U_e(z)$ denote the modeling error, which represent a stable causal LTI SISO system. The relative degree of $\boldsymbol{G}_o(z)$ is assumed to be smaller than or equal to that of $G(z)$, with $G(z) = U_e(z)G_o(z)$. If $\boldsymbol{G}$, $\boldsymbol{G}_o$ and $\boldsymbol{U}_e$ are lifted matrix representations of these systems, then $\boldsymbol{G} = \boldsymbol{U}_e\boldsymbol{G}_o$.*

In the presence of modeling error, plugging $\mathbf{G} = \mathbf{U}_e\mathbf{G}_o$ into Eq. (2.13), the Robust Monotonic Convergence (RMC) criterion is shown as following:

$$\|\mathcal{Q} - \mathcal{L}\mathbf{U}_e\mathbf{G}_o\|_2 < 1 \tag{2.14}$$

2.5 NO-ILC in Frequency Domain

Instead of analyzing the updating law in the time domain, this thesis performs an analysis in the frequency domain. Frequency domain analysis has been a well-established tool in the literature (*Donkers et al.*, 2008; *Gorinevsky*, 2002; *Gunnarsson and Norrlof*, 2001; *Norrlof and Gunnarsson*, 2002a, 2005) for infinite time horizon analysis, i.e., $N \to \infty$, and is adopted in this work as well to provide insights about the performance of NO-ILC that can be useful in determining the weighting matrices for NO-ILC. This thesis considers LTI systems; therefore, $\mathbf{W}_1$, $\mathbf{W}_2$ and $\mathbf{W}_3$ can be considered as lifted representations of LTI filters. Thus, for the remainder of this work, the following frequency-domain updating law is considered:

$$\begin{aligned} u_{i+1}(z) &= \mathcal{Q}(z)u_i(z) + \mathcal{L}(z)e_i(z) \\ \mathcal{Q}(z) &= \frac{G_o(z^{-1})Q(z)G_o(z) + R(z)}{G_o(z^{-1})Q(z)G_o(z) + R(z) + S(z)} \\ \mathcal{L}(z) &= \frac{G_o(z^{-1})Q(z)}{G_o(z^{-1})Q(z)G_o(z) + R(z) + S(z)} \end{aligned} \tag{2.15}$$

where weighting filters $Q(z) = W_1(z^{-1})W_1(z)$, $R(z) = W_2(z^{-1})W_2(z)$ and $S(z) = W_3(z^{-1})W_3(z)$ are zero phase filters and $W_1(z)$, $W_2(z)$ and $W_3(z)$ are causal LTI filters.

Note here $\mathcal{Q}$, $\mathcal{L}$, Q, R, S and G_o^T are just lifted representations of $\mathcal{Q}(z)$, $\mathcal{L}(z)$, $Q(z)$, $R(z)$, $S(z)$ and $G_o(z^{-1})$. These notations are frequently used in the rest of the thesis.

CHAPTER III

Model Uncertainty Formulation

In this chapter, a new model uncertainty formulation is proposed. Given the upper and lower bounds of uncertainty, the uncertainty region on the Bode plot is transferred to the Nyquist plot. Then, the frequency domain RMC criterion is revisited, where its validity is addressed and the shortcomings of the existing graphical interpretation are laid out.

3.1 Model Uncertainty

The modeling error $U_e(z)$ is in general unknown, but belongs to a certain range, which can be estimated or obtained, for example, through frequency response tests. The following paragraphs discuss the uncertainty range transformation between the Bode plot and Nyquist plot.

Fig. 3.1 shows the frequency response of the nominal plant (indicated as the solid green curve) and the upper/lower bounds of model uncertainty region (indicated as the dashed blue curves, denoted as $G_{\max}(z) = U_{e,\max}(z)G_o(z)$ and $G_{\min}(z) = U_{e,\min}(z)G_o(z)$). Thus, the real system $G(z) = U_e(z)G_o(z)$ can be any curve within

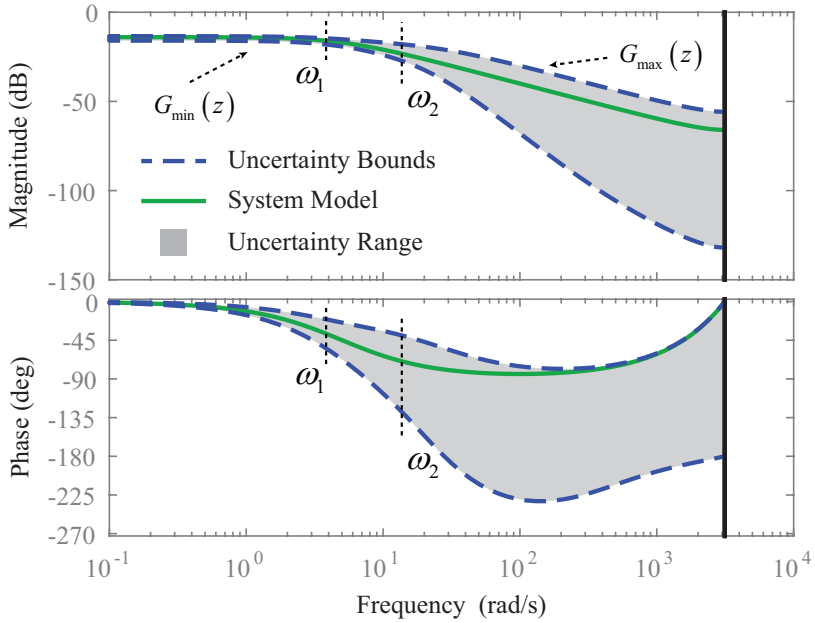

Figure 3.1: Example model uncertainty expressed on the Bode plot

the shaded region. Therefore, the following relationships hold:

$$\begin{aligned} \left|U_{e,\min}\left(e^{j\theta}\right)\right| &\leq \left|U_e\left(e^{j\theta}\right)\right| &\leq \left|U_{e,\max}\left(e^{j\theta}\right)\right| \\ \measuredangle U_{e,\min}\left(e^{j\theta}\right) &\leq \measuredangle U_e\left(e^{j\theta}\right) &\leq \measuredangle U_{e,\max}\left(e^{j\theta}\right) \end{aligned} \tag{3.1}$$

where $|\cdot|$ and $\measuredangle$ denote the magnitude and phase of a complex number, respectively. $\theta = T_s\omega$, where T_s is the time step size and ω is the frequency.

At each frequency ω, according to Eq. (3.1), the range of $U_e(e^{j\theta})$ can be interpreted on the Nyquist plot. As an example, the model uncertainty regions corresponding to the two frequencies ω_1 and ω_2 shown in Fig. 3.1 are shown as the gray regions in Fig. 3.2.

The novelty of the proposed uncertainty formulation and its significance can be stated in detail as follows. The robust control literature proposes the uncertainty formulation $G(z) = G_o(z)(1 + w_I(z)\Delta(z))$, where $w_I(z)$ is the weighting for uncertainty and $|\Delta(z)|_\infty \leq 1$. Here $|\cdot|_\infty$ denotes the H_∞ norm. This formulation, which incorporates magnitude information only, has been widely adopted into the ILC lit-

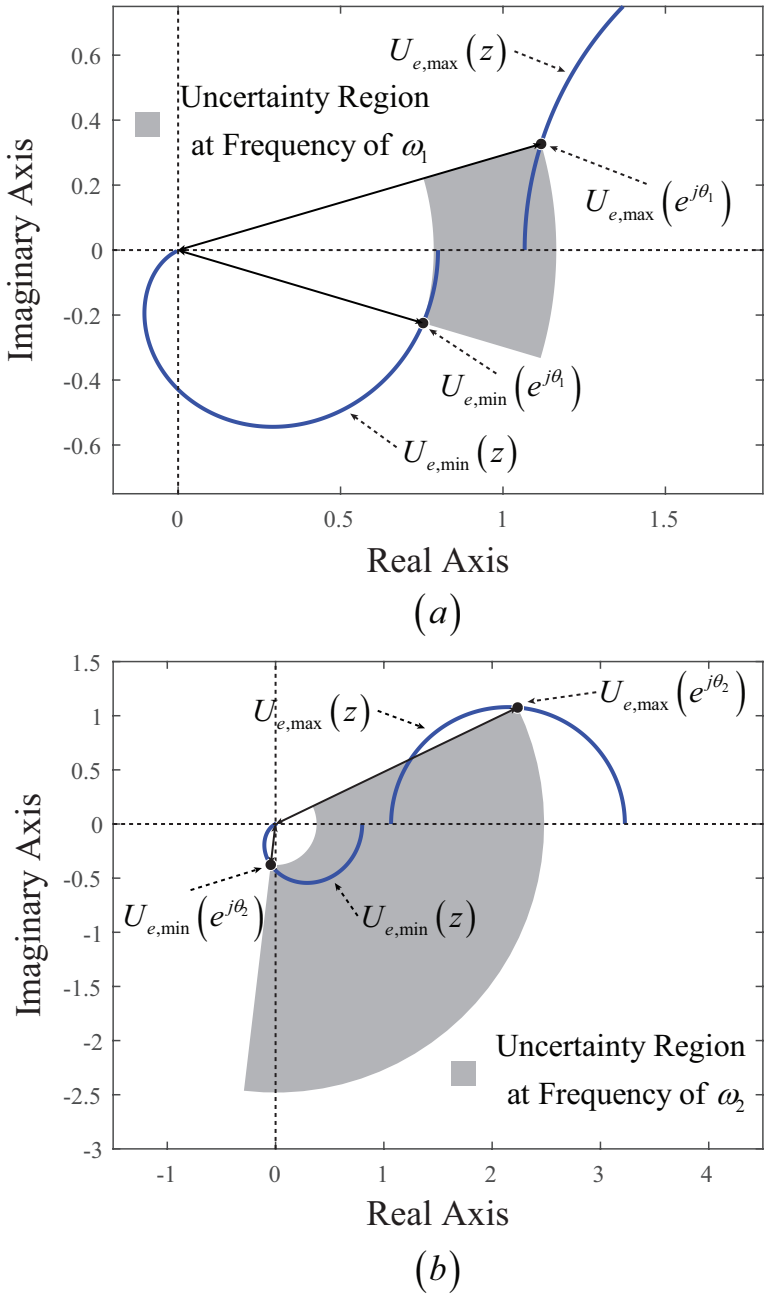

Figure 3.2: Model uncertainty in Fig. 3.1 expressed on the Nyquist Plot at frequency of (a) ω_1 and (b) ω_2

erature. It represents an uncertainty region in the Nyquist plot that is a disk centered at $(1, 0)$ with a radius of $\left|w_I(e^{j\theta})\right|$ at each frequency. Using the uncertainty formulation of $G(z) = G_o(z)(1 + w_I(z)\Delta(z))$ leads to the conclusion that the term $(\mathbf{u}_{i+1} - \mathbf{u}_i)^T R (\mathbf{u}_{i+1} - \mathbf{u}_i)$ in the NO-ILC cost function, Eq. (1.1), does not affect the robustness of NO-ILC (*Gorinevsky*, 2002; *Donkers et al.*, 2008). The proposed uncertainty formulation in this thesis incorporates not only the magnitude information but also the phase information. With this proposed uncertainty formulation, it is shown that the term $(\mathbf{u}_{i+1} - \mathbf{u}_i)^T R (\mathbf{u}_{i+1} - \mathbf{u}_i)$ in Eq. (1.1) actually affects the RMC region, but in a different manner compared with the term $\mathbf{u}_i^T Q \mathbf{u}_i$ (details are given in Chapter IV). Also, given the upper and lower bounds for the uncertainty region shown in Fig. 3.1, using $G(z) = G_o(z)(1 + w_I(z)\Delta(z))$ leads to a more conservative uncertainty region representation on the Nyquist plot compared with the proposed one, since using this traditional uncertainty formulation to represent the proposed uncertainty shown in Fig. 3.1 leads to an uncertainty region that is a disk centered at $(1, 0)$ with radius of $\left|w_I(e^{j\theta})\right|$ that encloses the gray region in Fig. 3.2.

As an example, consider the model uncertainty shown in Fig. 3.1 at the frequency of ω_2. Using the proposed uncertainty formulation leads to an uncertainty region shown as the dark gray region in Fig. 3.3. Using the traditional uncertainty formulation, $G(z) = G_o(z)(1 + w_I(z)\Delta(z))$, leads to an uncertainty region shown as the light gray disk in Fig. 3.3. The proposed uncertainty formulation incorporates both magnitude and phase information, while the traditional uncertainty formulation just uses the magnitude information. Thus, the proposed formulation leads to a less conservative uncertainty region representation. How this helps to achieve a less conservative robust monotonic convergent NO-ILC design is discussed in Chapter IV.

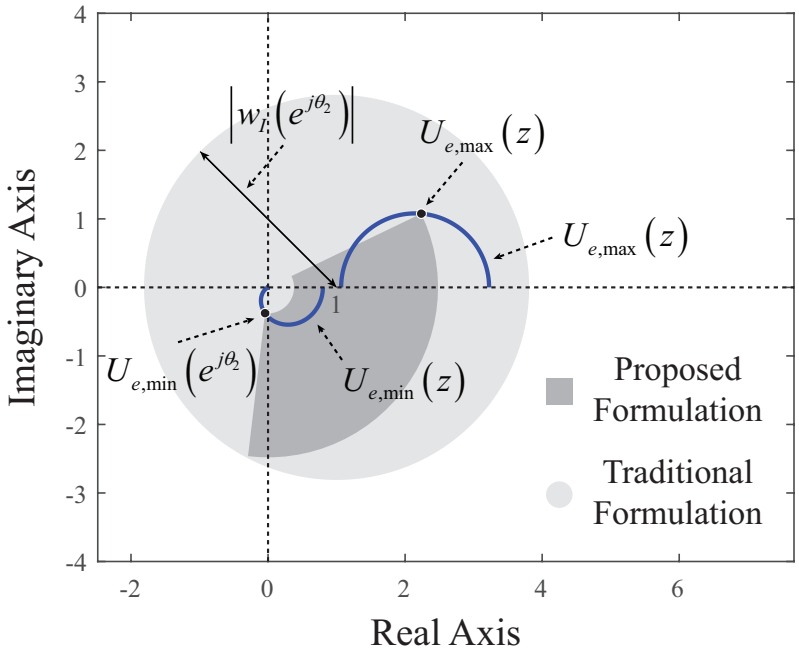

Figure 3.3: Comparison of the proposed and traditional model uncertainty formulations

3.2 Frequency Domain RMC Criterion

This work focuses on an infinite time horizon analysis, i.e., $N \to \infty$. For an infinite time horizon, the following monotonic convergence criterion has been widely used in the literature:

$$|\mathcal{Q}(z) - G(z)\mathcal{L}(z)|_\infty < 1 \tag{3.2}$$

This criterion was originally proven in (*Norrlof and Gunnarsson*, 2002a) for causal $\mathcal{Q}(z)$ and $\mathcal{L}(z)$ and has also been stated as an appropriate convergence criterion for infinite time horizon analysis in the literature for NO-ILC (*Gunnarsson and Norrlof*, 2001; *Donkers et al.*, 2008), which has non-causal $\mathcal{Q}(z)$ and $\mathcal{L}(z)$. A detailed discussion on the validity of the above frequency domain monotonic convergence criterion for an infinite time horizon analysis is shown in the coming paragraphs. The difference between the time and frequency domain non-causal ILC updating law is pointed out first for the infinite time horizon case. Then, the validity of using Eq. (3.2) as

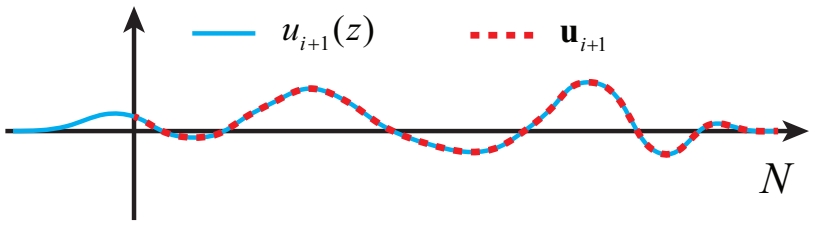

Figure 3.4: An illustration of $\mathbf{u}_{i+1}$ and $u_{i+1}(z)$ obtained through Eq. (3.3)

the RMC criterion for an infinite time horizon analysis of NO-ILC is discussed.

Recall that the input for the next iteration $\mathbf{u}_{i+1}$ and $u_{i+1}(z)$ are obtained through the following updating laws:

$$\begin{aligned} \mathbf{u}_{i+1} &= \mathcal{Q}\mathbf{u}_i + \mathcal{L}\mathbf{e}_i \\ u_{i+1}(z) &= \mathcal{Q}(z)u_i(z) + \mathcal{L}(z)e_i(z) \end{aligned} \tag{3.3}$$

where $\mathcal{Q}$ and $\mathcal{L}$ are the lifted representations of the non-causal $\mathcal{Q}(z)$ and $\mathcal{L}(z)$. One important difference between $\mathbf{u}_{i+1}$ and $u_{i+1}(z)$ is the fact that $\mathbf{u}_{i+1}$ denotes a signal that only exists in the positive time interval, whereas $u_{i+1}(z)$ denotes a signal that has components in the negative time interval, as well, since $\mathcal{Q}(z)$ and $\mathcal{L}(z)$ are non-causal. This difference is illustrated in Fig. 3.4. For the rest of this section, $\mathcal{Z}\{\cdot\}$ and $\mathcal{Z}^{-1}\{\cdot\}$ are used to denote the two sided z-transform and inverse z-transform of a signal. For a signal, the notation $\mathbf{g}$ denotes only its causal portion, while $g(z)$ denotes the two sided z-transform of this signal. Thus, $\mathcal{Z}\{\mathbf{g}\}$ is not equal to $g(z)$ unless the signal is causal.

Monotonic convergence is defined as $\|\mathbf{u}_{i+1} - \mathbf{u}_\infty\|_2 < \|\mathbf{u}_i - \mathbf{u}_\infty\|_2$. The input and tracking error from the current iteration must be causal signals, since these are the signals collected from a physical system. Thus, $u_i(z) = \mathcal{Z}\{\mathbf{u}_i\}$ and $e_i(z) = \mathcal{Z}\{\mathbf{e}_i\}$.

Using Parseval's Theorem, it is straightforward to show that Eq. (3.2) is the criterion for Eq. (3.4).

$$\left\|\mathcal{Z}^{-1}\{u_{i+1}(z)\} - \mathcal{Z}^{-1}\{u_\infty(z)\}\right\|_2 < \left\|\mathcal{Z}^{-1}\{u_i(z)\} - \mathcal{Z}^{-1}\{u_\infty(z)\}\right\|_2 \tag{3.4}$$

Eq. (3.4) indicates that $u_{i+1}(z)$ will monotonically converge to $u_\infty(z)$. However, once $u_{i+1}(z)$ is truncated into $\mathbf{u}_{i+1}$, is Eq. (3.2) still an appropriate monotonic convergence criterion for the non-causal ILC updating laws in the infinite time horizon analysis?

When $\mathcal{Q}(z) = 1$, it can be shown that Eq. (3.2) is a valid criterion for $\|\mathbf{u}_{i+1} - \mathbf{u}_\infty\|_2 < \|\mathbf{u}_i - \mathbf{u}_\infty\|_2$. To this end, the causality of $u_\infty(z)$ plays a critical role.

Let $u_d(z)$ be the causal and stable ideal input sequence that can go through the physical system $G(z)$ so that $G(z)u_d(z) = r(z)$, where $r(z)$ is the tracking reference. $u_\infty(z)$ is the input sequence when the algorithm converges and it can be derived from Eq. (3.3) as follows:

$$u_\infty(z) = \frac{G(z)\mathcal{L}(z)}{1 - \mathcal{Q}(z) + G(z)\mathcal{L}(z)} u_d(z) \tag{3.5}$$

For NO-ILC, when $\mathcal{Q}(z) = 1$, $u_\infty(z)$ is causal since $u_\infty(z) = u_d(z)$ from the above equation and $u_d(z)$ is causal. When $\mathcal{Q}(z) \neq 1$, $u_\infty(z)$ becomes non-causal.

In the case when $u_\infty(z)$ is causal, i.e., $\mathcal{Q}(z) = 1$ for NO-ILC, since $u_i(z)$ is causal, too, as discussed in the previous section, Eq. (3.4) can be rewritten into

$$\left\| \mathcal{Z}^{-1}\{u_{i+1}(z)\} - \mathbf{u}_\infty \right\|_2 < \|\mathbf{u}_i - \mathbf{u}_\infty\|_2 \tag{3.6}$$

Since the signal $\mathbf{u}_{i+1} - \mathbf{u}_\infty$ is the causal portion of the signal $\mathcal{Z}^{-1}\{u_{i+1}(z)\} - \mathbf{u}_\infty$, the following relationship is true:

$$\|\mathbf{u}_{i+1} - \mathbf{u}_\infty\|_2 \leq \left\| \mathcal{Z}^{-1}\{u_{i+1}(z)\} - \mathbf{u}_\infty \right\|_2 \tag{3.7}$$

Therefore,

$$\|\mathbf{u}_{i+1} - \mathbf{u}_\infty\|_2 \leq \left\| \mathcal{Z}^{-1}\{u_{i+1}(z)\} - \mathbf{u}_\infty \right\|_2 < \|\mathbf{u}_i - \mathbf{u}_\infty\|_2 \tag{3.8}$$

Thus, Eq. (3.2) is the criterion for $\|\mathbf{u}_{i+1} - \mathbf{u}_\infty\|_2 < \|\mathbf{u}_i - \mathbf{u}_\infty\|_2$ when $u_\infty(z)$ is causal,

i.e., $\mathcal{Q}(z) = 1$.

When $\mathcal{Q}(z) \neq 1$, Eq. (3.2) can be used as an approximation for an infinite time horizon analysis according to the following argument. The small portion of the signal that lies in the negative time interval (the portion of the blue curve that lies in the negative time interval in Fig. 3.4) can be neglected since the portion in the positive time interval will dominate when $N \to \infty$. Thus, Eq. (3.2) can be an appropriate monotonic convergence criterion for non-causal ILC updating laws for the infinite time horizon analysis, if one is mindful of the fact that NO-ILC is always implemented in a finite time horizon. In particular, since the analysis is performed in the infinite time horizon, it is reasonable to expect some errors at the beginning and end of each iteration. The errors at the beginning are due to the fact that the non-causal portion of $u_{i+1}(z)$ is truncated, since inputs in the negative time interval cannot be fed to a physical system. The errors at the end are due to the fact that the time does not go to infinity. Nevertheless, when N is sufficiently large, the frequency domain analysis provides a good approximation of time domain results.

As a conclusion, for NO-ILC, when $\mathcal{Q}(z) = 1$, Eq. (3.2) can be rigorously justified as a valid RMC criterion for infinite time horizon analysis. Otherwise, Eq. (3.2) should be used as an approximation. As the time horizon becomes larger, this approximation becomes better, because the signals in the positive time interval will dominate the signals in the negative time interval.

It is very important to note that, in practice, NO-ILC is always implemented in finite time horizon. The time domain convergence criterion is $||\mathcal{Q} - \mathcal{L}G||_2 < 1$. It has been pointed out in (*Van De Wijdeven et al.*, 2009) that the frequency domain convergence criterion, Eq. (3.2), implies the time domain convergence criterion only when $\mathcal{L}(z)$ is causal. For NO-ILC, however, the learning gain $\mathcal{L}(z)$ is non-causal. Thus, Eq. (3.2) can only be used as an approximation since the time horizon is always finite in practice. Nevertheless, the frequency domain interpretation still gives

useful insights in terms of designing NO-ILC when N is sufficiently large, i.e, the time horizon is significantly longer than the length of the non-zero impulse responses of $G(z)$, $W_1(z)$, $W_2(z)$ and $W_3(z)$. For example, among all the simulation tests that the author has performed to date, a value of N that is five times longer than the length of the non-zero impulse responses of all the filters, the frequency domain analysis and design approach served as a good approximation.

Therefore, it would be prudent to leave some safety margin and not design the RMC disk, which will be discussed in Chapter IV, too tight around the uncertain region on the Nyquist plot.

3.3 Existing Graphical Interpretation on RMC

Substituting the uncertainty formulation, $G(z) = U_e(z)G_o(z)$, and NO-ILC updating law, Eq. (2.15), into the monotonic convergence criterion, Eq. (3.2), the following expression can be obtained for all $\theta \in [0, 2\pi]$:

$$\left| 1 - \frac{\left|W_1\left(e^{j\theta}\right)\right|^2 \left|G_o\left(e^{j\theta}\right)\right|^2}{\left|W_1\left(e^{j\theta}\right)\right|^2 \left|G_o\left(e^{j\theta}\right)\right|^2 + \left|W_2\left(e^{j\theta}\right)\right|^2} U_e\left(e^{j\theta}\right) \right| < 1 + \frac{\left|W_3\left(e^{j\theta}\right)\right|^2}{\left|W_1\left(e^{j\theta}\right)\right|^2 \left|G_o\left(e^{j\theta}\right)\right|^2 + \left|W_2\left(e^{j\theta}\right)\right|^2} \quad (3.9)$$

Note that $U_e(e^{j\theta})$ is a complex number; worst case scenario of Eq. (3.9) for a particular θ in the complex plane is shown in Fig. 3.5. With modeling error $U_e(z)$, the causal LTI filters, $W_1(z)$,$W_2(z)$ and $W_3(z)$, should be chosen so that the green vector in Fig. 3.5 lies within the red circle.

This graphical interpretation helps with the qualitative understanding of the robustness of NO-ILC; similar interpretations can be found in (*Gunnarsson and Norrlof*, 2001; *Norrlof and Gunnarsson*, 2005). However, using the above interpretation to design or tune a robust monotonic convergent NO-ILC is a challenge for the fol-

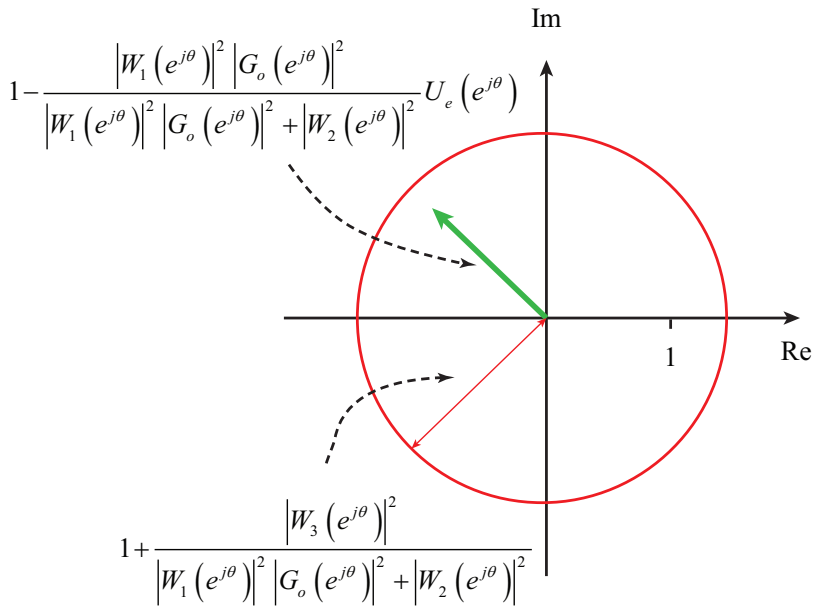

Figure 3.5: Graphical interpretation of Eq. (3.9)

lowing reasons. In real applications, the modeling error $U_e(z)$ is not known exactly, but only its range is known. Hence, Fig. 3.5 must include not only one, but a set of vectors that cover the modeling error range. Furthermore, the appearance of Fig. 3.5 depends on $W_1(z)$, $W_2(z)$, $W_3(z)$, $G_o(z)$ and $U_e(z)$. This implies two challenges. First, a new figure must be created for each frequency. Second, because both the radius of the circle and the vectors depend on the NO-ILC design parameters $W_1(z)$, $W_2(z)$ and $W_3(z)$, the radius of the circle and the vectors cannot be adjusted independently. Because of these reasons, using the graphical interpretation in Fig. 3.5 for design would lead to an ad-hoc and time consuming process.

Therefore, a new graphical interpretation is needed that decouples the complex geometric interdependencies in Fig. 3.5 and helps visualize what the allowable range of modeling error for RMC is for a specific design of $W_1(z)$, $W_2(z)$ and $W_3(z)$. The following chapter addresses this gap using a frequency domain analysis.

On the other hand, from analysis in the time domain, the RMC criterion is proposed in (*Donkers et al.*, 2008; *Van De Wijdeven et al.*, 2009). The results in (*Van De Wijdeven et al.*, 2009) are useful for checking RMC for specific model uncertainties and

ILC filter designs $\mathcal{Q}(z)$ and $\mathcal{L}(z)$. However, no design guidelines are suggested. Hence, using this tool to address the gap identified above would require a trial-and-error process of applying RMC criterion to various $W_1(z)$, $W_2(z)$ and $W_3(z)$ designs until a design that yields a satisfactory performance is found. Furthermore, the argument in (*Donkers et al.*, 2008; *Gorinevsky*, 2002) has stated that $(\mathbf{u}_{i+1} - \mathbf{u}_i)^T R (\mathbf{u}_{i+1} - \mathbf{u}_i)$ in Eq. (1.1) does not influence the RMC properties of NO-ILC. However, through the analysis in this thesis, a stronger statement is obtained; namely, increasing R influences RMC positively. Hence, the existing techniques give a conservative evaluation of the RMC range, whereas the analysis provided in this work aims to provide a more complete evaluation, as well as a less conservative systematic design process.

3.4 Conclusion

In this chapter, a new model uncertainty formulation is proposed. Unlike the traditional uncertainty formulation which does not incorporate the phase information, the proposed uncertainty formulation incorporates both the magnitude and phase information. The incorporation of this additional phase information not only provides a less conservative representation of the uncertainty region but also, more importantly, leads to a more aggressive NO-ILC design as discussed in the next chapter.

The proposed uncertainty formulation is initially formulated on the Bode plot. This chapter presents a method to transfer the uncertainty region from the Bode plot to the Nyquist plot at each frequency. Then the frequency domain RMC criterion is revisited. The validity of this criterion is addressed for the infinite time horizon analysis. Even though this frequency domain RMC criterion is only an approximation since NO-ILC is always implemented in finite time horizon, the infinite time horizon analysis still provides useful insights towards some frequency domain properties of NO-ILC. Finally, the shortcomings of the existing graphical interpretation are laid out, which motivates new frequency domain analysis and design methodologies for

NO-ILC.

CHAPTER IV

RMC Analysis and Design Tools

In this chapter, the frequency domain RMC analysis and design methodologies are addressed. New graphical interpretations that characterize the allowable modeling errors for NO-ILC are presented, with the understanding of which the RMC design guidelines naturally follow. The discussions can be divided into two parts.

For the first part, Section 4.1, diagonal weighting matrices analysis and design methodologies for NO-ILC are addressed. Setting the weighting matrices Q, R and S to I, λI and βI respectively, where I denotes the identity matrix, and adjusting the λ and β values for the RMC requirement is a common choice when designing NO-ILC. With respect to the equivalent frequency domain realization, this indicates $W_1(z) = 1$, $W_2(z) = \sqrt{\lambda}$ and $W_3(z) = \sqrt{\beta}$. In this part, the allowable modeling error region on the Nyquist plot is characterized with and without the Q-filter. Then a design guideline is proposed. Finally, some simulation examples are presented to demonstrate the utility of the theoretical results.

For the second part, Section 4.2, the analysis and design methodologies for non-diagonal weighting matrices for NO-ILC are addressed. Unlike the previous case in which $W_1(z)$, $W_2(z)$ and $W_3(z)$ are just constant gains, the magnitudes of $\left|W_1\left(e^{j\theta}\right)\right|$, $\left|W_2\left(e^{j\theta}\right)\right|$ and $\left|W_3\left(e^{j\theta}\right)\right|$ are adjusted at different frequencies. This leads to a frequency dependent weighting matrices design. Compared with the previous design

approach discussed in Section 4.1, this frequency dependent design approach better addresses the fundamental trade-off between robustness, convergence speed and steady state error, which is discussed in Chapter V. First, the effect of the weighting filters $W_1(z)$, $W_2(z)$ and $W_3(z)$ affect the RMC region on the Nyquist plot is discussed. Then design guidelines for this approach are proposed, followed with some simulation examples.

4.1 Diagonal Weighting Matrices Design

In this section, the allowable region of the modeling error $U_e(z)$ is interpreted through the Nyquist plot for a robust monotonic convergent NO-ILC as a function of λ and β. Before going into the detailed analysis, note that, with $W_1(z) = 1$, $W_2(z) = \sqrt{\lambda}$ and $W_3(z) = \sqrt{\beta}$, Eq. (3.2) can be re-written into Eq. (4.1) for all $\theta \in [0, 2\pi]$, where $\mathrm{Re}\{\cdot\}$ denotes the real part of a complex number. From now on, Eq. (4.1) serves as the criterion for RMC and the following two sections discuss the interpretation of this criterion with $\beta = 0$ and $\beta \neq 0$; i.e., with and without the Q-filter.

$$\left(\frac{\left|G_o\left(e^{j\theta}\right)\right|^2}{\left|G_o\left(e^{j\theta}\right)\right|^2+\lambda+\beta}\right)^2\left|U_e\left(e^{j\theta}\right)\right|^2+\left(\frac{\left|G_o\left(e^{j\theta}\right)\right|^2+\lambda}{\left|G_o\left(e^{j\theta}\right)\right|^2+\lambda+\beta}\right)^2 - 2\frac{\left(\left|G_o\left(e^{j\theta}\right)\right|^2+\lambda\right)\left|G_o\left(e^{j\theta}\right)\right|^2}{\left|G_o\left(e^{j\theta}\right)\right|^2+\lambda+\beta}\mathrm{Re}\{U_e\left(e^{j\theta}\right)\}<1 \quad (4.1)$$

4.1.1 RMC of NO-ILC without Q-Filter

In this section, the allowable modeling error region is analyzed for the RMC condition. With the Q-filter disabled, the corresponding allowable error with respect to a specific λ value is illustrated visually on the Nyquist plot. The results show that the RMC region expands as λ increases, but there are certain modeling errors that cannot be accommodated with using λ only.

With $\beta = 0$, Criterion (4.1) can be simplified as follows. For all $\theta \in [0, 2\pi]$

$$\alpha^2(\theta)\left|U_e\left(e^{j\theta}\right)\right|^2 - 2\alpha(\theta)\,\mathrm{Re}\{\left(U_e\left(e^{j\theta}\right)\right)\} < 0 \tag{4.2}$$

where $\alpha(\theta)$ is defined as

$$\alpha(\theta) \triangleq \frac{\left|G_o\left(e^{j\theta}\right)\right|^2}{\left|G_o\left(e^{j\theta}\right)\right|^2 + \lambda} \in (0, 1] \tag{4.3}$$

Proposition IV.1. *The NO-ILC with the updating law of Eq. (2.15) with $\beta = 0$ cannot be robust monotonic convergent for the uncertain plant formulated in* ***Proposition II.2****, if $\mathrm{Re}\{U_e(e^{j\theta})\}$ is negative for any $\theta \in [0, 2\pi]$.*

Proof. See Appendix A for the proof. □

The above proposition illustrates the fundamental limitation of using only λ. If $\mathrm{Re}\{U_e(e^{j\theta})\}$ is negative for any $\theta \in [0, 2\pi]$, it is not possible to satisfy Criterion (3.2) by using λ only. Nevertheless, increasing λ still helps enlarge the RMC region as discussed below.

Proposition IV.2. *With the updating law of Eq. (2.15), if NO-ILC with $\lambda = \lambda_0$ and $\beta = 0$ has RMC against the modeling error $U_e(z)$, NO-ILC still has RMC for at least the same modeling error $U_e(z)$ for $\lambda' > \lambda_0$ and $\beta = 0$.*

Proof. See Appendix A for the proof. □

Previous results in the literature have stated that increasing λ would not affect the robustness of NO-ILC (*Donkers et al.*, 2008; *Gorinevsky*, 2002; *Van De Wijdeven et al.*, 2009). The results above more specifically show that increasing λ does not affect the RMC in a negative way. It is further shown in the following that increasing λ actually enlarges the RMC region of NO-ILC.

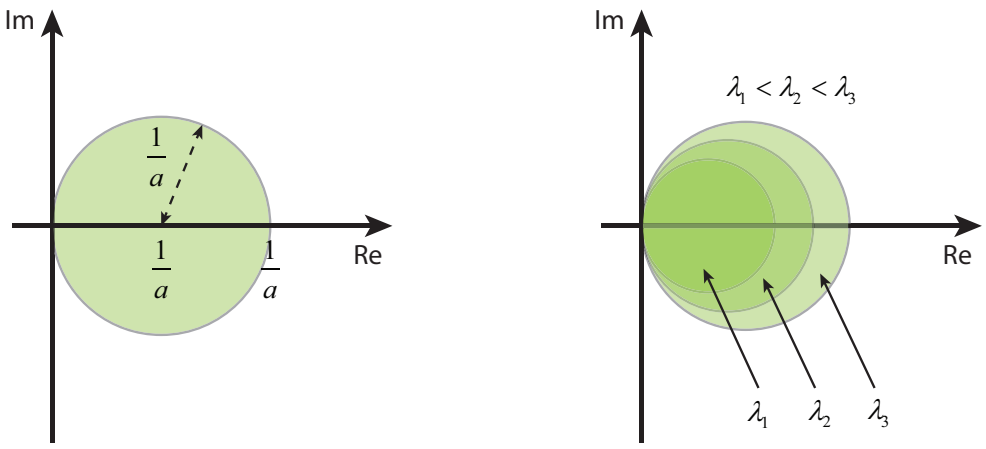

Figure 4.1: Geometric representation of RMC region of NO-ILC without Q-filter

To better understand the impact of λ, an analysis is developed that helps to visualize the RMC region of NO-ILC with $\beta = 0$. Towards this end, the following definitions are introduced:

$$a \triangleq \sup_{\theta\in[0,2\pi]} \alpha(\theta); \quad x(\theta) \triangleq \mathrm{Re}\{U_e\left(e^{j\theta}\right)\}; \quad y(\theta) \triangleq \mathrm{Im}\{U_e\left(e^{j\theta}\right)\} \tag{4.4}$$

where $\mathrm{Im}\{\cdot\}$ denotes the imaginary part of a complex number. With these definitions, a sufficient condition for Criterion (4.2), which will be proved in **Lemma IV.3**, can be stated as:

$$2ax(\theta) - a^2\left(x^2(\theta) + y^2(\theta)\right) > 0 \quad \Leftrightarrow \quad \left(x(\theta) - \frac{1}{a}\right)^2 + y^2(\theta) < \left(\frac{1}{a}\right)^2 \tag{4.5}$$

The above inequality describes a disk in the complex plane, which can be visualized as shown in Fig. 4.1. The center of the disk is located at $1/a$ on the real axis and the radius of the disk is $1/a$. As λ increases, the center of the disk shifts towards right and its radius becomes larger as shown in Fig. 4.1, with each new disk encompassing the previous ones.

Lemma IV.3. *Consider the NO-ILC as described by Eq. (2.15) with $\lambda = \lambda_0$, $\beta = 0$, and the modeling error $U_e(z)$. The NO-ILC has RMC if $U_e\left(e^{j\theta}\right)$ stays inside the disk*

described by Eq. (4.5) for all $\theta \in [0, 2\pi]$. *Furthermore, using* $\lambda' > \lambda_0$ *would enlarge the RMC region as shown in Fig. 4.1.*

Proof. See Appendix A for the proof. □

4.1.2 RMC of NO-ILC with Q-Filter

If the modeling error $U_e(z)$ is not positive real, a case in which increasing λ while keeping $\beta = 0$ would not help achieve RMC, the following analysis shows that using $\beta > 0$ in NO-ILC can help the algorithm tolerate this kind of modeling error. This additional tolerance of modeling error is shown both analytically and visually with the help of the Nyquist plot in this section.

Define $\gamma(\theta)$ as follows:

$$\gamma(\theta) \triangleq \frac{\left|G_o\left(e^{j\theta}\right)\right|^2}{\left|G_o\left(e^{j\theta}\right)\right|^2 + \lambda + \beta} \tag{4.6}$$

With $\alpha(\theta)$ and $\gamma(\theta)$ defined, Criterion (4.1) can be re-written as the following for all $\theta \in [0, 2\pi]$:

$$\gamma^2(\theta)\left|U_e\left(e^{j\theta}\right)\right|^2 - 2\frac{\gamma^2(\theta)}{\alpha(\theta)}\mathrm{Re}\{U_e\left(e^{j\theta}\right)\} + \frac{\gamma^2(\theta)}{\alpha^2(\theta)} - 1 < 0 \tag{4.7}$$

Proposition IV.4. *With the updating law of Eq. (2.15), if NO-ILC with* $\beta = 0$ *and* $\lambda = \lambda_0$ *has RMC against the modeling error* $U_e(z)$ *as formulated in* ***Proposition II.2****, NO-ILC still has RMC at least for the same modeling error* $U_e(z)$ *for* $\lambda = \lambda_0$ *and* $\beta > 0$.

Proof. See Appendix A for the proof. □

Even though using β adds additional robustness to the algorithm, it will potentially introduce steady state error. Thus, for scenarios where the model uncertainty is

positive real, if avoiding unnecessary steady state error is preferred, a larger λ value should be used instead of introducing the Q-filter.

Proposition IV.5. *With the updating law of Eq. (2.15), if NO-ILC with $\beta = \beta_0$ and $\lambda = \lambda_0$ has RMC against the modeling error $U_e(z)$ formulated as in* ***Proposition II.2****, NO-ILC still has RMC at least for the same modeling error $U_e(z)$ for $\lambda' \geq \lambda_0$ and $\beta' \geq \beta_0$.*

Proof. See Appendix A for the proof. □

Note that the results in (*Donkers et al.*, 2008; *Gorinevsky*, 2002; *Van De Wijdeven et al.*, 2009) state that adding a Q-filter enhances the robustness of NO-ILC, but λ does not affect the robustness of NO-ILC. However, the above results show that both λ and β affect the robustness indeed. The way λ and β affect the RMC region is different, which has not yet been pointed out in the literature and is addressed next.

Similar to the case without the Q-filter, the effect of λ and β on the RMC region of NO-ILC can be visualized in the complex plane. To this end, Eq. (4.1) can be re-written, after some manipulation, as follows:

$$\left(x(\theta) - \frac{1}{\alpha(\theta)}\right)^2 + y^2(\theta) < \left(\frac{1}{\gamma(\theta)}\right)^2, \quad \forall\theta \in [0, 2\pi] \tag{4.8}$$

With q defined as

$$q \triangleq \sup_{\theta\in[0,2\pi]} \frac{\left|G_o\left(e^{j\theta}\right)\right|^2}{\left|G_o\left(e^{j\theta}\right)\right|^2 + \lambda + \beta} = \sup_{\theta\in[0,2\pi]} \gamma(\theta) \tag{4.9}$$

a sufficient condition for Eq. (4.8), which will be proved in **Lemma IV.6**, is obtained as follows:

$$\left(x(\theta) - \frac{1}{a}\right)^2 + y^2(\theta) < \left(\frac{1}{q}\right)^2, \quad \forall\theta \in [0, 2\pi] \tag{4.10}$$

Eq. (4.10) describes a disk centered at $1/a$ with a radius of $1/q$ as shown in Fig. 4.2. The center of the disk is affected by λ and the radius is affected by both λ and β.

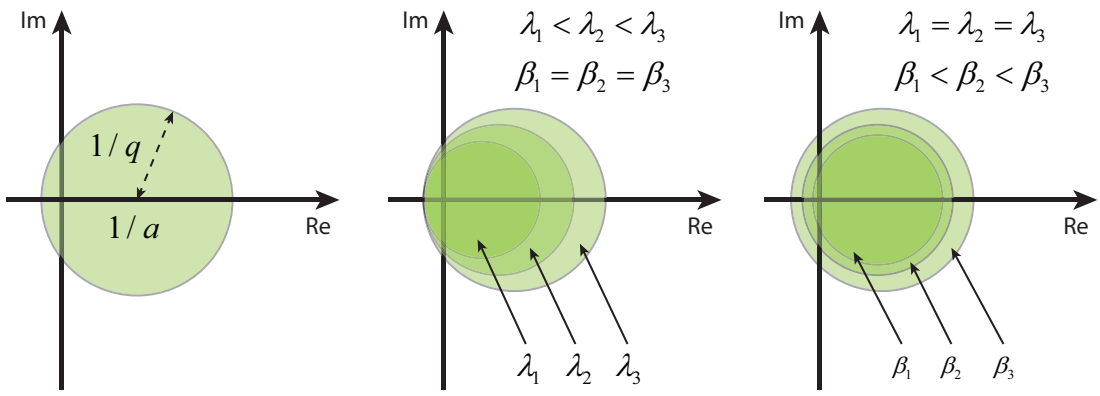

Figure 4.2: Geometric representation of RMC region of NO-ILC with Q-filter

Since a is smaller than q according to their definitions in Eq. (4.4) and Eq. (4.9), this disk encloses certain areas in the left half plane of the complex plane. Increasing λ or β enlarges the area enclosed by the disk. Increasing β, however, helps cover more area in the left half plane, which cannot be achieved by increasing λ alone.

Lemma IV.6. *Consider the NO-ILC as described by Eq. (2.15) with $\lambda = \lambda_0$ and $\beta = \beta_0$, as well as the modeling error $U_e(z)$ as formulated in* ***Proposition II.2****. The NO-ILC has RMC against the modeling error if $U_e\left(e^{j\theta}\right)$ stays inside the disk described by Eq. (4.10) for all $\theta \in [0, 2\pi]$. Furthermore, using $\lambda' > \lambda_0$ or $\beta' > \beta_0$ would enlarge the RMC region as shown in Fig. 4.2.*

Proof. See Appendix A for the proof. □

Instead of providing equations that are used to check the RMC condition for given weighting parameter values to a specific model uncertainty formulation as in (*Donkers et al.*, 2008; *Gorinevsky*, 2002; *Van De Wijdeven et al.*, 2009), this work specifically gives the allowable modeling error boundary with respect to the weighting parameter values of NO-ILC, which offers a design guideline for picking λ and β in NO-ILC as will be discussed in the next section. More importantly, this work explicitly points out how the design parameters λ and β affect the RMC region differently; i.e., the disk center is affected by λ, while the radius of the disk is related to both λ and β.

As shown in Fig. 4.2, with $\beta = 0$ the disk always lies in the right half plane; on the other hand, with $\beta \neq 0$ the disk can cover certain areas in the left half plane. With this frequency domain tool, one can determine the appropriate λ and β values if the range of the modeling error is given.

To give a better illustration of the comparisons between the proposed and traditional analysis on RMC of NO-ILC, consider the scenario illustrated in Fig. 4.3. Fig. 4.3a compares the different model uncertainty formulations. The proposed uncertainty formulation leads to an uncertainty region shown as the dark gray region, while the traditional uncertainty formulation leads to an uncertainty region shown as the light gray region, which is due to the fact that the proposed uncertainty formulation method incorporates additional phase information; compared with the traditional one, a less conservative uncertainty region can be obtained. Furthermore, using the traditional uncertainty formulation leads to the conclusion that λ does not affect the robustness of NO-ILC (*Donkers et al.*, 2008; *Gorinevsky*, 2002). The RMC disk design using the traditional uncertainty formulation is shown as the blue region in Fig. 4.3b. When the proposed uncertainty formulation is used, however, the RMC disk can be designed as the green disk shown in Fig. 4.3b. Even though both designs ensure RMC, the traditional uncertainty formulation leads to a NO-ILC design with steady state error, because the disk goes into the left half plane. In contrast, a design without steady state error ensues with the proposed uncertainty formulation. Therefore, the proposed design approach can help avoid unnecessary steady state error in this scenario.

4.1.3 Design Guideline

The above analysis has shown how λ and β affect the RMC region. Based on this analysis, some guidelines for designing λ and β are summarized as follows:

- Formulate the uncertain system and mesh the frequency range. Then obtain

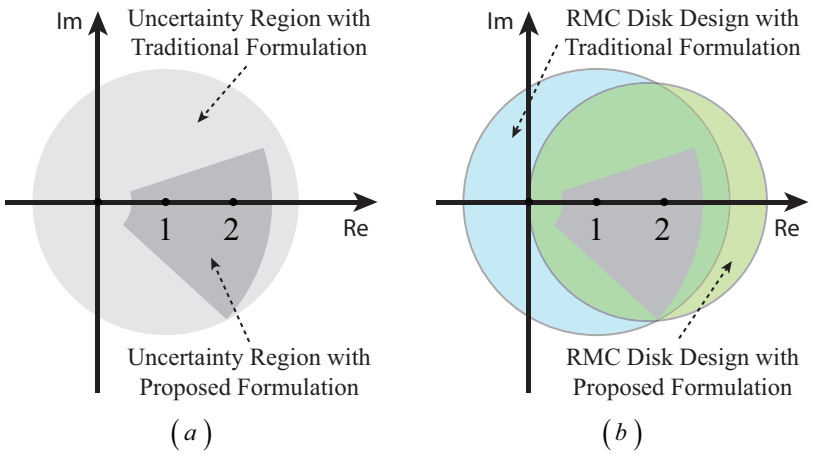

Figure 4.3: Illustration of the benefits of the proposed approach: (a) the uncertainty regions and (b) the RMC disks resulting from the traditional and proposed uncertainty formulations.

the uncertainty region for each frequency on the Nyquist plot as discussed in Chapter III.

- For all frequencies, if the gray regions always lie in the right half plane on the Nyquist plot, pick $\beta = 0$. Perform an initial design of λ according to the Eq. (4.4) that characterizes the center and radius of the RMC disk. Increase or decrease λ until the RMC region encloses the uncertainty regions over all frequencies.

- If the uncertainty region goes to the left half plane at some frequencies, β cannot be zero. First perform an initial design of λ and β according to Eq. (4.4) and Eq. (4.9). If the leftmost point of the RMC disk needs to be shifted towards the left, increase β. Otherwise, decrease β. If a larger disk is needed, increase the value of λ. Otherwise, decrease λ.

For example, considering the RMC design problem against the gray model uncertainty shown in Fig. 4.4 at two specific frequencies ω_1 and ω_2, λ and β need to be designed so that the gray uncertainty regions lie inside the green RMC disk as shown in Fig. 4.4. Note that Fig. 4.4 illustrates the design criterion for only two

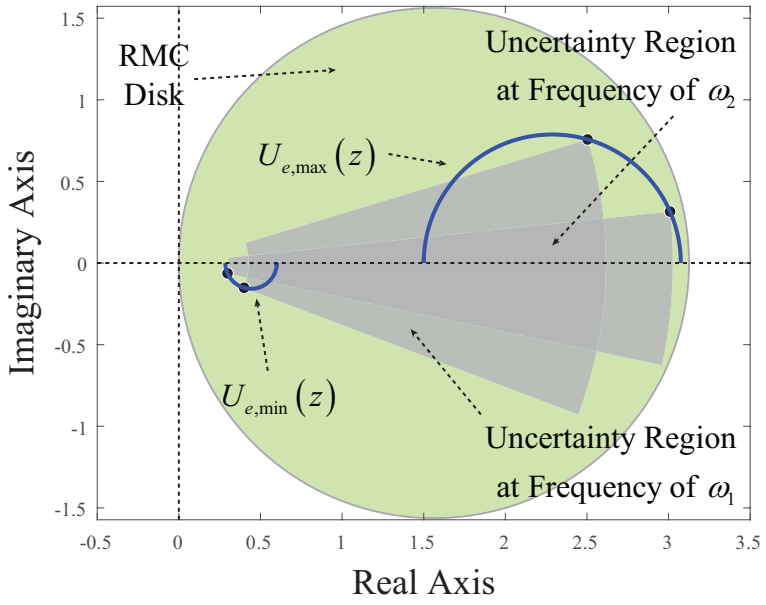

Figure 4.4: Achieving RMC for the example model uncertainty regions at two frequencies

frequencies. For the purpose of RMC against all possible modeling errors, $U_e(z)$, it must be ensured that the design criterion is valid for all frequencies.

4.1.4 Simulation Examples

The frequency domain analysis presented above provides insights into the RMC of NO-ILC against model uncertainties. The three examples given in this section illustrate how the proposed tool in the frequency domain is useful towards designing the appropriate weighting parameters to achieve RMC of NO-ILC against specified model uncertainties. All the continuous transfer functions given in this section are discretized with a sampling frequency of $T_s = 0.01$s in the implementation. The total running steps N is 3000.

Specifically, the first example demonstrates the utility of the proposed methodology against a positive real model uncertainty. At the same time, it also compares the proposed approach to the traditional approach and shows how unnecessary steady state error can be avoided with the proposed approach. The second example, using

a positive real model uncertainty as well, illustrates a scenario that the design of the weighting parameters for RMC relates to a trade-off between the convergence speed and steady state error. In this example, the effect of measurement noise is also explored and the effectiveness of the two proposed noise compensation methods is demonstrated. The third example demonstrates the utility of the proposed design methodology against non-positive real uncertainties.

4.1.4.1 Example 1

Consider a system with the following nominal plant and modeling error:

$$G_o(s) = \frac{s+20}{s+5}; \quad U_e(s) = 1.4\frac{(0.19s+1)(0.033s+1)}{(0.08s+1)(0.05s+1)} \tag{4.11}$$

Let the upper and lower bounds of the model uncertainty be

$$U_{e,\max}(s) = 3\frac{s+5}{s+10}; \quad U_{e,\min}(s) = 0.3\frac{s+20}{s+10} \tag{4.12}$$

Fig. 4.5 shows the nominal model $G_o(z)$, real plant $G(z)$ and the uncertainty region on the Bode plot. The dashed blue lines indicate the upper and lower bounds $G_{\max}(z)$ and $G_{\min}(z)$. The gray region represents all possible uncertain plants. The green curve indicates the nominal model $G_o(z)$ and the red dotted line shows the real plant $G(z)$, which lies inside the uncertainty region.

The Nyquist plots of $U_{e,\max}(z)$ and $U_{e,\min}(z)$ are shown as the blue curves in Fig. 4.6. The real modeling error $U_e(z)$ is shown as the red curve. The black dots on the above three curves represent the values of $U_{e,\max}(z)$, $U_{e,\min}(z)$ and $U_e(z)$ at the frequency of 13.27 rad/s. The dark gray region shows the corresponding uncertainty region with the proposed uncertainty formulation at this frequency. The two green disks represent the RMC disk for two NO-ILC designs with $\lambda = 9$ and $\lambda = 16$. $\beta = 0$ is picked as zero for both designs since the modeling uncertainty is positive real. Both

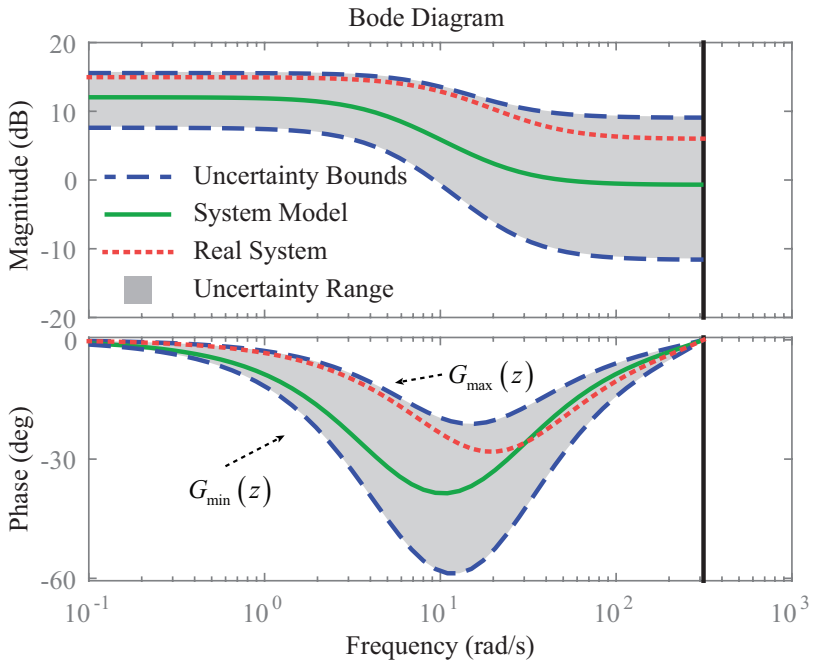

Figure 4.5: Bode plot of $G(z)$, $G_o(z)$, $G_{\max}(z)$, $G_{\min}(z)$ and uncertainty region for Example 1

designs ensure that the RMC disk encloses the uncertainty region over all frequencies.

The tracking performances for both designs are shown in Fig. 4.7 with tracking error and input difference defined as:

$$\begin{aligned} \text{Tracking Error} &\triangleq \mathbf{y}_d - \mathbf{y}_i \\ \text{Input Difference} &\triangleq \mathbf{u}_i - \mathbf{u}_\infty \end{aligned} \tag{4.13}$$

The tracking reference $\mathbf{y}_d$ is a sinusoid of 15 rad/s with a magnitude of 1. In Fig. 4.7, the red dashed line shows the tracking error and input difference in the iteration domain with a design of $\lambda = 16$, whereas the blue solid line shows the tracking error and input difference in the iteration domain with a design of $\lambda = 9$. Since the uncertainty region lies inside the RMC disk over all frequencies, the input differences are monotonic convergent for both cases. Tracking errors are monotonic convergent for both cases as well. Perfect tracking is achieved for both cases since the Q-filter is disabled.

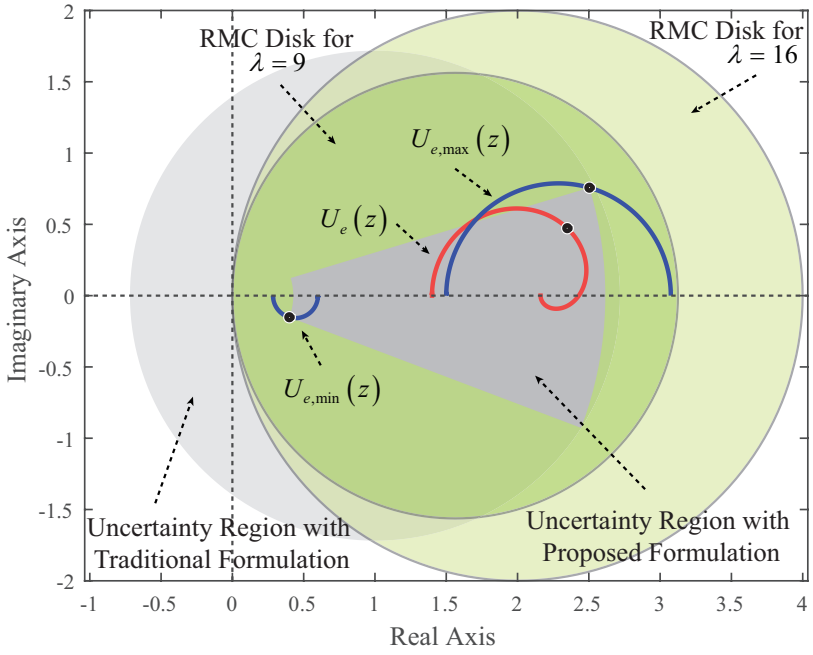

Figure 4.6: RMC disks with different λ values and uncertainty region at a frequency of 13.23 rad/s on the Nyquist plot for Example 1

Note that for robust monotonic convergent NO-ILC designs, usually the one with a larger λ value leads to slower convergence, which is demonstrated in this example. However, this is not always true. The detailed analysis can be found in Chapter VI.

As a comparison, if the traditional uncertainty formulation is used for this example, a Q filter has to be used. To see this, consider the frequency of 13.23 rad/s as an example. The light gray disk in Fig. 4.6 indicates the corresponding uncertainty region with the traditional uncertainty formulation at this frequency, which goes into the negative half plane, which bears two consequences. First, the traditional uncertainty formulation gives a more conservative result than what the proposed one yields. Second, if the traditional NO-ILC design methodology, which does not recognize the impact of λ towards the robustness, is used to design against the uncertainty formulated in the traditional sense, it is found that the smallest β value that guarantees RMC in this case is about 1.4. The results of using $\lambda = 0$ and $\beta = 1.4$ are shown as the green dashed line in Fig. 4.7. Even though this design gives a monotonic

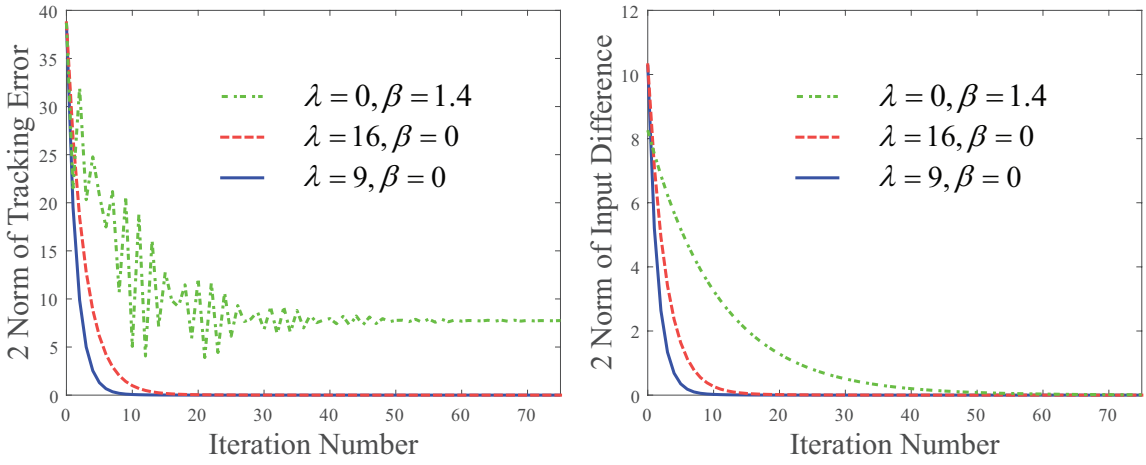

Figure 4.7: Tracking results of NO-ILC with $\lambda = 9$ and $\lambda = 16$ in Example 1

convergent result, there is a significant steady state error as well as large oscillations in the tracking error. Also note that the convergence speed is slower compared with the proposed design. This demonstrates the significance of the proposed uncertainty formulation and design approach over the traditional ones. Note that the monotonic convergence of $||\mathbf{u}_i - \mathbf{u}_\infty||_2$ does not necessarily imply the monotonic convergence of $||\mathbf{e}_i||_2$, especially in the presence of steady state error, which can be seen in Fig. 4.7.

4.1.4.2 Example 2

Consider a system with the same nominal plant as the previous example, but with different modeling error:

$$G_o(s) = \frac{s+20}{s+5}; \quad U_e(s) = 0.95\frac{(0.45s+1)^2}{(1.5s+1)(2.5s+1)} \tag{4.14}$$

Let the upper and lower bounds of the modeling uncertainty be

$$U_{e,\max}(s) = 1.3\frac{0.15s+1}{0.1s+1}; \quad U_{e,\min}(s) = \frac{0.8(0.45s+1)^2}{(1.5s+1)(3s+1)} \tag{4.15}$$

The Bode plot of the nominal model $G_o(z)$, real plant $G(z)$ and the uncertainty

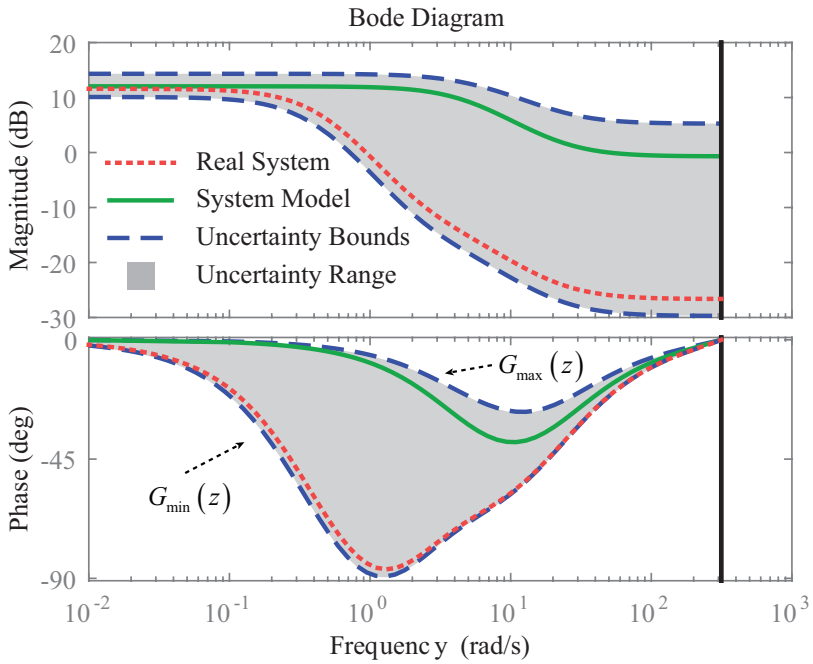

Figure 4.8: Bode plot of $G(z)$, $G_o(z)$, $G_{\max}(z)$, $G_{\min}(z)$ and uncertainty region for Example 2

region are shown in Fig. 4.8.

The corresponding Nyquist plot is shown in Fig. 4.9. There are two RMC disks in the figure; for space issues, only a portion of the disks are shown. The RMC disk with its leftmost point lying on the origin corresponds to a NO-ILC design with $\lambda = 46.24$ and $\beta = 0$. The RMC disk that encloses some area in the left half plane corresponds to a NO-ILC design with $\lambda = 32.49$ and $\beta = 1$. Both designs ensure that the corresponding RMC disk encloses the gray uncertainty region over all frequencies.

The tracking reference in this case is a sinusoid of 1.5 rad/s with a magnitude of 1. As has been analyzed before, since the model uncertainty is positive real, β is not necessary for the purpose of RMC. With $\beta = 0$, the smallest λ one can choose is about 46.24 to satisfy the graphical criterion. However, this leads to a very large RMC disk and therefore, even though perfect tracking is achieved, the convergence speed is slow as shown in Fig. 4.10.

In order to accelerate the convergence speed without compromising RMC, a Q-

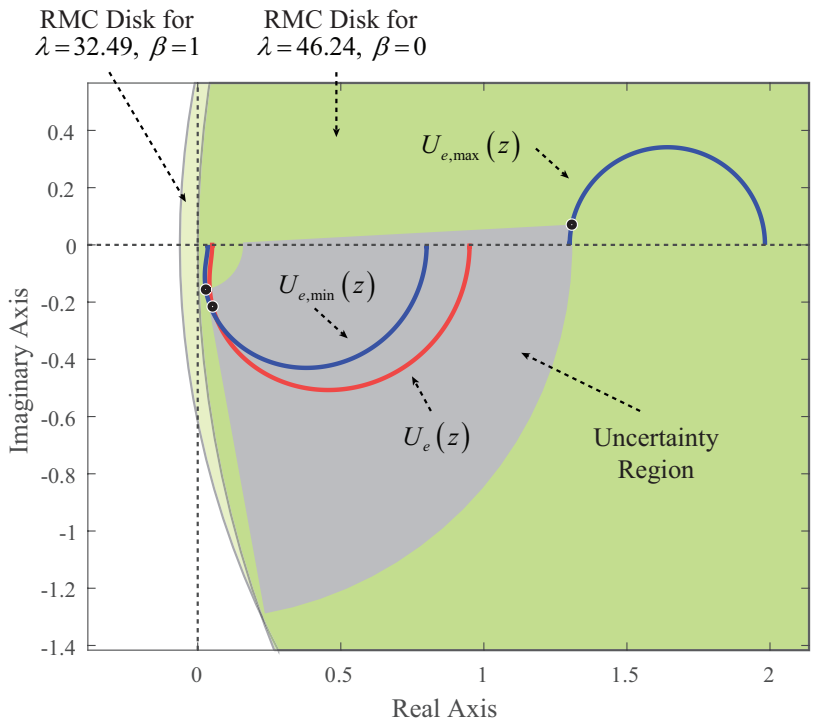

Figure 4.9: RMC disks with two NO-ILC designs and uncertainty region at a frequency of 1.05 rad/s on the Nyquist plot for Example 2

filter can be introduced. With $\beta > 0$, λ can be smaller according to the expression of radius $1/q$ and center $1/a$ of the RMC disk. Here, $\lambda = 32.49$ and $\beta = 1$ are picked as an example. With this design, the algorithm converges faster, but at the expense of a steady state tracking error as shown in Fig. 4.10. Note, as mentioned before, that the monotonic convergence of $||\mathbf{u}_i - \mathbf{u}_\infty||_2$ does not necessarily imply the monotonic convergence of $||\mathbf{e}_i||_2$, especially in the presence of steady state error, which can be seen in Fig. 4.10.

Hence, this example illustrates the utility of the developed NO-ILC design method in adjusting the trade-off between convergence speed and steady state tracking error while ensuring RMC.

The effect of noise is also explored in this example. For the same system model and uncertainties, consider a scenario that a colored noise exists in the output measurement channel. This colored noise is obtained by passing a white noise through a

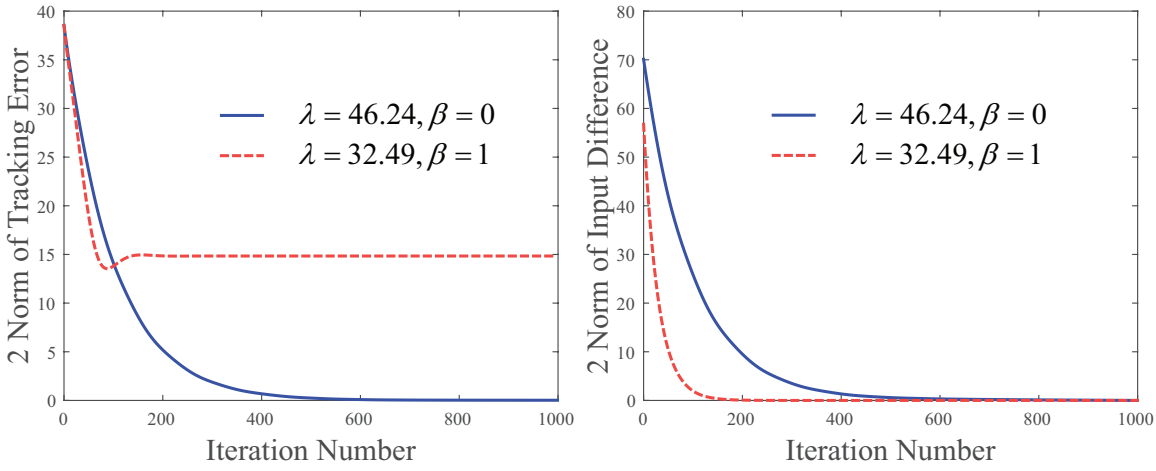

Figure 4.10: Tracking results of NO-ILC with $\lambda = 46.24$, $\beta = 0$ and $\lambda = 32.49$, $\beta = 1$ in Example 2

high pass filter $W_n(z)$ as shown in Eq. (4.16). The Fast Fourier Transform (FFT) of this colored noise is shown in Fig. 4.11.

$$W_n(s) = \frac{s}{s+100}; \quad W_1(s) = \frac{20}{s+20} \tag{4.16}$$

In the following, three design options are considered to tolerate this noise. All three designs use $\lambda = 46.24$ and $\beta = 0$ as the weighting parameters for NO-ILC. Here, $\mathbf{e}_i$ and $\mathbf{e}_{m,i}$ are used to denote the real tracking error and measured tracking error (with noise) in the i_{th} iteration.

Design Option 1 and Design Option 2 use the same Q-filter and learning gain as the previous scenario where measurement noise does not exist. Design Option 1 simulates a scenario in which no action is taken towards the existing measurement noise and the noisy tracking error, $\mathbf{e}_{m,i}$, is directly used in the updating law:

$$\mathbf{u}_{i+1} = \mathcal{Q}\mathbf{u}_i + \mathcal{L}\mathbf{e}_{m,i} \tag{4.17}$$

Design Option 2 simulates the case in which the noisy measured tracking error

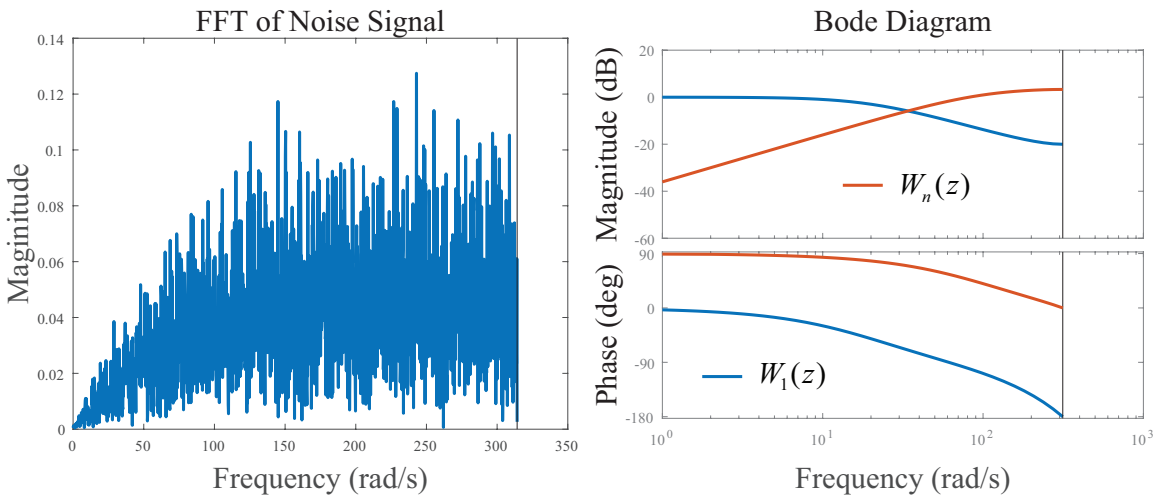

Figure 4.11: FFT of the noise signal and Bode plot of $W_1(z)$ and $W_n(z)$

is filtered through a low-pass filter $W_1(s)$ as shown in Eq. (4.16) and the filtered tracking error signal $\mathbf{e}_{f,i}$ is used in the updating law:

$$\mathbf{u}_{i+1} = \mathcal{Q}\mathbf{u}_i + \mathcal{L}\mathbf{e}_{f,i} \quad \text{with} \quad E_{f,i}(s) = W_1(s)E_{m,i}(s) \tag{4.18}$$

Design Option 3 uses a different Q-filter and learning gain compared with the two previous designs. Given the fact that noise occurs in the output measurement at high frequencies, the cost function is manipulated as follows:

$$J_{i+1}\left(\mathbf{u}_{i+1}\right) = \left\|\mathbf{e}_{f,i+1}\right\|_2^2 + \lambda \left\|\mathbf{u}_{i+1} - \mathbf{u}_i\right\|_2^2 + \beta \left\|\mathbf{u}_{i+1}\right\|_2^2 \tag{4.19}$$

where $\mathbf{e}_{f,i+1} = \mathbf{W}_1\mathbf{e}_{m,i+1}$ with $\mathbf{W}_1$ representing the lifted matrix form of $W_1(z)$. Thus, the same low-pass filter $W_1(z)$ is used as the one used in Design Option 2, but this time the low-pass filter is incorporated into the cost function. The ILC updating law

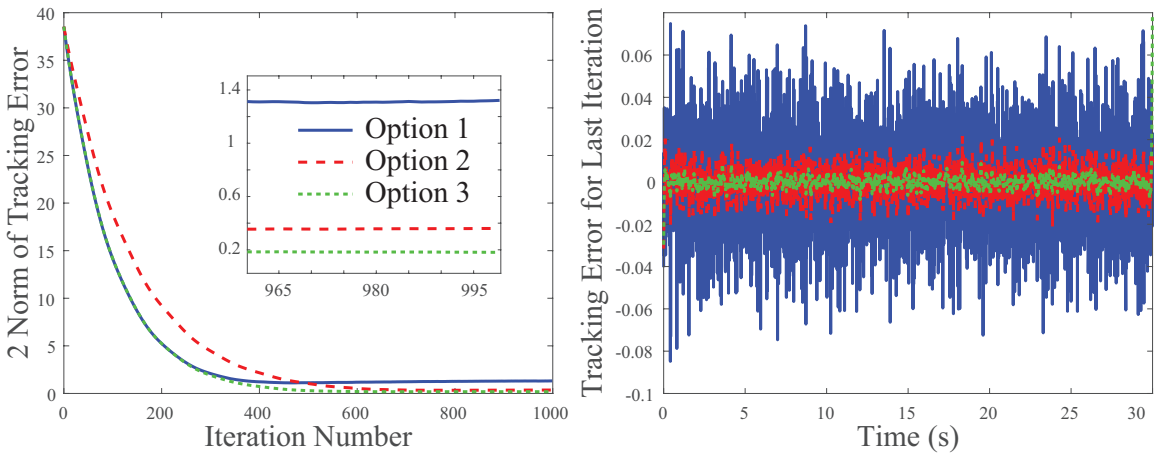

Figure 4.12: Tracking results of NO-ILC with $\lambda = 46.24$, $\beta = 0$ in Example 2 when measurement noise exists

therefore becomes:

$$\begin{aligned}
\mathbf{u}_{i+1} &= \hat{\mathcal{Q}}\mathbf{u}_i + \hat{\mathcal{L}}\mathbf{e}_{m,i} \\
\hat{\mathcal{Q}} &= (\mathbf{G}_o^T\mathbf{W}_1^T\mathbf{W}_1\mathbf{G}_o + \lambda I + \beta I)^{-1}(\mathbf{G}_o^T\mathbf{W}_1^T\mathbf{W}_1\mathbf{G}_o + \lambda I) \\
\hat{\mathcal{L}} &= (\mathbf{G}_o^T\mathbf{W}_i^T\mathbf{W}_1\mathbf{G}_o + \lambda I + \beta I)^{-1}\mathbf{G}_o^T\mathbf{W}_1^T
\end{aligned} \tag{4.20}$$

For the three design options, the 2 norm of the tracking errors in the iteration domain are shown in Fig. 4.12. The tracking errors for the last iteration are also shown in the right figure in Fig. 4.12.

By comparing the tracking results of Design Option 1 to the tracking results of the scenario without measurement noise, in which case the tracking error converges to zero as shown in Fig. 4.10, it is obvious that the measurement noise degrades the system performance in the sense that it introduces some steady-state error. Both Design Option 2 and 3 demonstrate improvements towards attenuating the effects induced by noise, with a smaller steady state error achieved by Design Option 3.

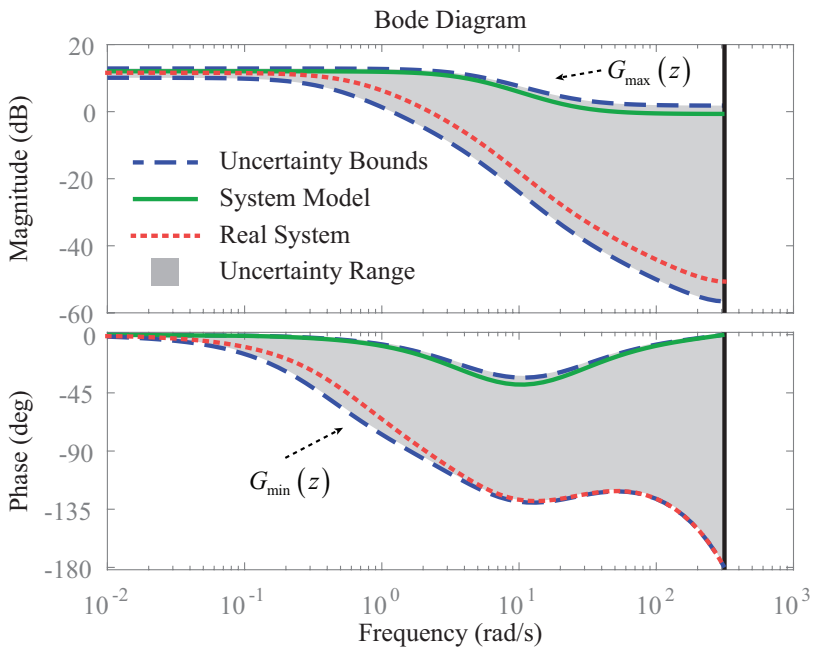

Figure 4.13: Bode plot of $G(z)$, $G_o(z)$, $G_{\max}(z)$, $G_{\min}(z)$ and uncertainty region for Example 3

4.1.4.3 Example 3

This example illustrates a scenario in which the phase uncertainty at high frequencies is larger than $\pm$ 90 degree. Consider the following system and modeling error:

$$G_o(s) = \frac{s+20}{s+5}; \quad U_e(s) = \frac{0.95}{1.5s+1} \tag{4.21}$$

Let the upper and lower bounds of the model uncertainty be:

$$U_{e,\max}(s) = 1.1\frac{0.12s+1}{0.1s+1}; \quad U_{e,\min}(s) = \frac{0.8}{2.5s+1} \tag{4.22}$$

The Bode plot of the nominal model $G_o(z)$, real plant $G(z)$ and the uncertainty region are shown in Fig. 4.13.

The corresponding Nyquist plot is shown in Fig. 4.14. The two RMC disks designed in the figure correspond to a NO-ILC design with $\lambda = 0$, $\beta = 22.09$ and $\lambda = 0$, $\beta = 30.25$. Both designs ensure that the corresponding RMC disk encloses

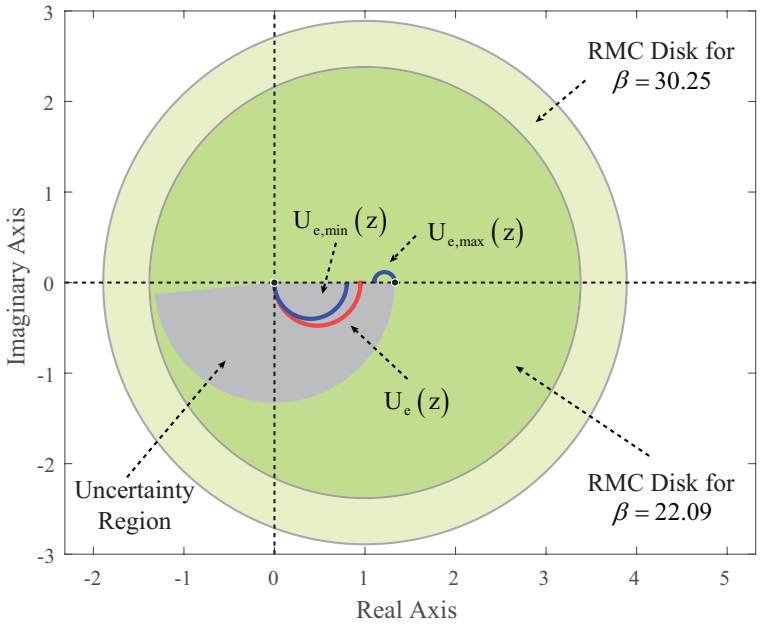

Figure 4.14: RMC disks with two NO-ILC designs and uncertainty region at a frequency of 294.87 rad/s on the Nyquist plot for Example 3

the gray uncertainty region over all frequencies. In this case, λ can be picked as zero since $|U_{e,\max}(e^{j\theta}) - 1|$ is smaller than 1 for all frequencies.

The tracking reference in this case is a sinusoid of 0.3 rad/s with a magnitude of 0.1. Comparing the tracking results for the two designs as shown in Fig. 4.15, it is confirmed that both designs guarantee RMC. Note that for robust monotonic convergent NO-ILC design, usually the one with a larger β value leads to a larger steady state error, which is demonstrated in this example. However, this is not always true. The detailed analysis can be found in Chapter VI.

4.2 Frequency Dependent Weighting Matrices Design

In this section, instead of analyzing the robustness property of NO-ILC for a diagonal weighting matrices design, a more general case is studied, i.e., non-diagonal weighting matrices design. In this case, the weighting filters $W_1(z)$, $W_2(z)$ and $W_3(z)$ are no longer constrained as constant gains. Furthermore, the graphical interpretation

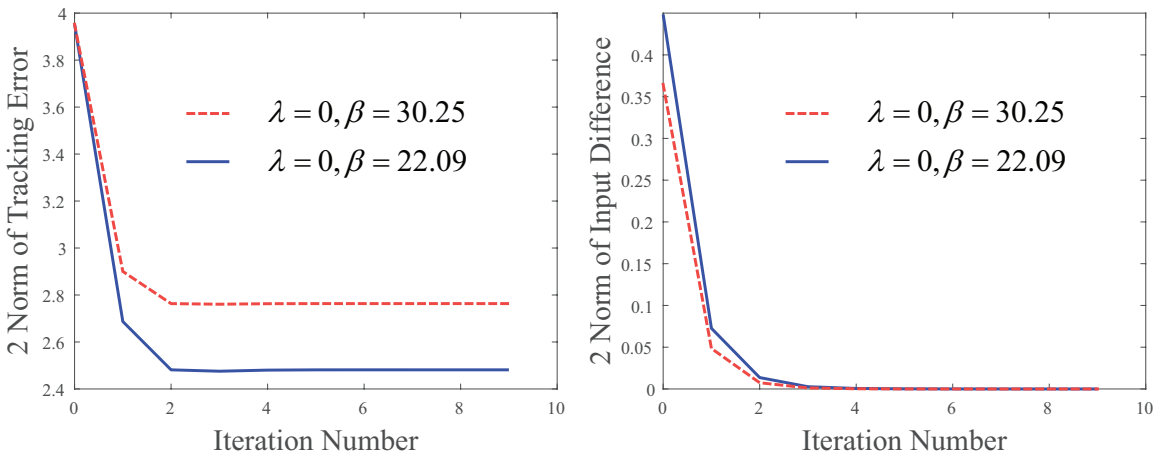

Figure 4.15: Tracking results of NO-ILC with $\lambda = 0$, $\beta = 22.09$ and $\lambda = 30$, $\beta = 30.25$ in Example 3

derived in Section 4.1, Eq. (4.10), is only a sufficient condition for the NO-ILC RMC criterion, Eq. (3.2) whereas in this section, a graphical interpretation that is sufficient and necessary for Eq. (3.2) is derived, which leads to RMC regions that can vary over different frequencies. With this additional freedom in design, this new design technique better addresses the fundamental trade-off of NO-ILC between robustness, convergence speed and steady state error at difference frequencies, which is clarified along with the discussion in Chapter V.

4.2.1 RMC Analysis

By plugging in $G(z) = U_e(z)G_o(z)$ into the RMC criterion, Eq. (3.2), the following inequality can be obtained:

$$\left(\mathcal{L}(e^{j\theta})G_o(e^{j\theta})\right)^2 \left|U_e(e^{j\theta})\right|^2 + \mathcal{Q}^2(e^{j\theta}) - 1 - 2\left(\mathcal{Q}(e^{j\theta})\mathcal{L}(e^{j\theta})G_o(e^{j\theta})\right)\mathrm{Re}\{U_e(e^{j\theta})\} < 0, \forall\theta \in [0, 2\pi] \quad (4.23)$$

Note that both $\mathcal{Q}(e^{j\theta})$ and $\mathcal{L}(e^{j\theta})G_o(e^{j\theta})$ are real numbers and $x(\theta)$, $y(\theta)$ are defined in Eq. (4.4). Then, Eq. (4.23) can be expressed as:

$$(x(\theta) - c(\theta))^2 + y^2(\theta) < r^2(\theta), \forall\theta \in [0, 2\pi] \tag{4.24}$$

where $c(\theta)$ and $r(\theta)$ are defined as:

$$\begin{aligned} c(\theta) &\triangleq \frac{\left|W_1\left(e^{j\theta}\right)\right|^2\left|G_o\left(e^{j\theta}\right)\right|^2 + \left|W_2\left(e^{j\theta}\right)\right|^2}{\left|W_1\left(e^{j\theta}\right)\right|^2\left|G_o\left(e^{j\theta}\right)\right|^2} \\ r(\theta) &\triangleq \frac{\left|W_1\left(e^{j\theta}\right)\right|^2\left|G_o\left(e^{j\theta}\right)\right|^2 + \left|W_2\left(e^{j\theta}\right)\right|^2 + \left|W_3\left(e^{j\theta}\right)\right|^2}{\left|W_1\left(e^{j\theta}\right)\right|^2\left|G_o\left(e^{j\theta}\right)\right|^2} \end{aligned} \tag{4.25}$$

Note that Eq. (4.24) describes a disk, centered at $c(\theta)$ with a radius of $r(\theta)$. At each frequency, as long as the possible $U_e(e^{j\theta})$ lies inside the disk enclosed by Eq. (4.24), the NO-ILC updating law will have RMC against this modeling error. Note that:

$$r(\theta) - c(\theta) = \frac{\left|W_3\left(e^{j\theta}\right)\right|^2}{\left|W_1\left(e^{j\theta}\right)\right|^2\left|G_o\left(e^{j\theta}\right)\right|^2} \tag{4.26}$$

If $W_3(e^{j\theta}) = 0$, then $r(\theta) = c(\theta)$, meaning the disk at this frequency θ cannot cover any area of the left half of the complex plane, as shown in Fig. 4.16a. This means that, at any frequency θ, as long as the real part of model uncertainty is positive, i.e., $\mathrm{Re}\{U_e(e^{j\theta})\} > 0$, $W_3(e^{j\theta})$ can be zero. This is an important insight when designing NO-ILC since $W_3(e^{j\theta}) = 0$ leads to zero steady state error at this frequency, as discussed in later sections.

At any frequency θ, if the real part of model uncertainty is not positive, $W_3(e^{j\theta})$ cannot be zero if RMC is desired. If $W_3(e^{j\theta}) \neq 0$, then $r(\theta) > c(\theta)$, which means the disk can cover some area in the left half plane as shown in Fig. 4.16b. This additional coverage of the left half plane furnishes additional robustness, but at the expense of a steady state error in the iteration domain, as discussed in Chapter V.

For a specific frequency, θ, the location and size of the RMC disk with respective

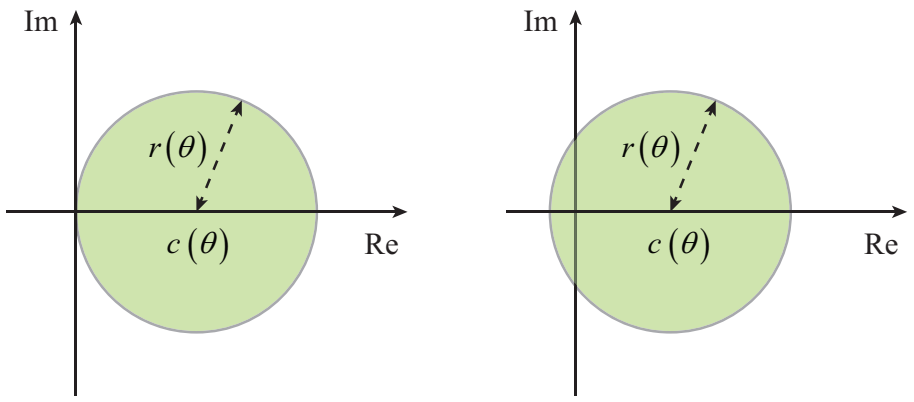

(a) (b)

Figure 4.16: RMC region example for (a) $W_3(e^{j\theta}) = 0$, and (b) $W_3(e^{j\theta}) \neq 0$

to $W_1(e^{j\theta})$, $W_2(e^{j\theta})$ and $W_3(e^{j\theta})$ are shown in Fig. 4.17:

1. When $W_2(e^{j\theta})$ is held constant and $W_3(e^{j\theta}) = 0$, increasing $\left|W_1(e^{j\theta})\right|$ shifts the center of the disk to the left and, at the same time, shrinks the disk. This is shown in Fig. 4.17a.

2. When $W_1(e^{j\theta})$ is held constant and $W_3(e^{j\theta}) = 0$, increasing $\left|W_2(e^{j\theta})\right|$ shifts the center of the disk to the right and, at the same time, enlarges the disk. This is shown in Fig. 4.17b.

3. Note that for both cases above, the disk does not enclose any region in the left half plane. When $W_1(e^{j\theta})$ and $W_2(e^{j\theta})$ are held constant, increasing $\left|W_3(e^{j\theta})\right|$ increases the radius of the disk, keeping the disk center unchanged. Thus, the disk can cover a certain area in the left half plane. This is shown in Fig. 4.17.c.

4.2.2 Design Guideline

Understanding the above analysis, a procedure for designing $W_1(z)$, $W_2(z)$ and $W_3(z)$ can be laid out as follows:

1. Generate the upper and lower bound of the model uncertainty, $U_{e,\max}\left(e^{j\theta}\right)$ and $U_{e,\min}\left(e^{j\theta}\right)$, on the Bode plot as shown in Chapter III. Sample the frequency

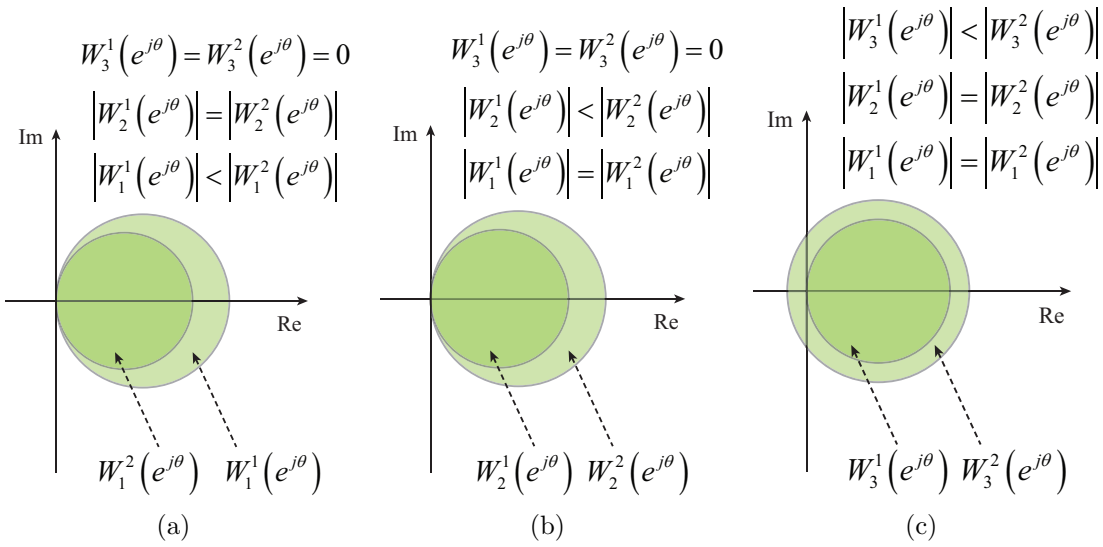

Figure 4.17: Illustration of how the RMC region changes with respect to $W_1(e^{j\theta})$, $W_2(e^{j\theta})$ and $W_3(e^{j\theta})$

range of the system using $m \in \mathbb{N}^+$ points $\{\theta_1, \cdots, \theta_m\}$. Ideally, m would be infinity, but for practical purposes m can be picked sufficiently large. Transform the uncertainty region onto the Nyquist plot at each frequency as shown in Chapter III, θ_i for $i \in [1, m]$.

2. For each frequency θ_i, design $W_1\left(e^{j\theta_i}\right)$, $W_2\left(e^{j\theta_i}\right)$ and $W_3\left(e^{j\theta_i}\right)$ according to Eq. (4.25) so that the RMC disk encloses the uncertainty region on the Nyquist plot. To avoid a too conservative design, i.e., to avoid too slow convergence and unnecessary steady state errors, the RMC disk should be as small as possible and the leftmost point of the RMC disk should be as close to zero as possible. This requires some tuning on the chosen $W_1(z)$, $W_2(z)$ and $W_3(z)$ as is discussed in the following bullet. Alternatively, the design of the weighting filters can be formulated as an optimization problem to avoid manual tuning, as will be addressed in Chapter VI.

3. For any frequency θ_i, set $W_3\left(e^{j\theta_i}\right)$ to zero if the uncertainty region lies in the right half plane. If the disk needs to be enlarged towards the right hand side,

either increase $W_2\left(e^{j\theta_i}\right)$ or decrease $W_1\left(e^{j\theta_i}\right)$. If the disk needs to be enlarged to cover more area in the left half plane, increase $W_3\left(e^{j\theta_i}\right)$.

As a comparison, with diagonal weightings in the cost function, i.e., $Q = I$, $R = \lambda I$ and $S = \beta I$ (or equivalently $W_1(z) = 1$, $W_2(z) = \sqrt{\lambda}$ and $W_3(z) = \sqrt{\beta}$), the degree of freedom for shaping the RMC region at different frequencies is very limited. When $W_1(z)$, $W_2(z)$ and $W_3(z)$ are constant for all frequencies, a design that is too conservative towards robustness over a certain frequency range is likely to occur, which ultimately sacrifices the convergence speed and steady state error in this frequency range as discussed in Chapter V. In contrast, this non-diagonal/frequency-dependent filter design gives the opportunity to shape the RMC region at different frequencies. This motivation for a frequency dependent weighting filter design will be further obvious when the fundamental trade-off analysis at each frequency is presented in the next chapter.

As a conclusion, the filters $W_1(z)$, $W_2(z)$ and $W_3(z)$ need to be designed so that for every frequency, the possible modeling error, $U_e(e^{j\theta})$, which is unknown but lies inside an uncertainty range, is guaranteed to lie inside the RMC region. For example, considering the RMC design problem against the gray modeling uncertainty shown in Fig. 4.18 at two specific frequencies ω_1 and ω_2, $W_1(z)$, $W_2(z)$, and $W_3(z)$ need to be designed so that the gray uncertainty region lies inside the green RMC disk as shown in Fig. 4.18. Note that Fig. 4.18 illustrates the design criterion for only two frequencies. For the purpose of RMC against all possible modeling errors, $U_e(z)$, it must be ensured that the design criterion is valid for all frequencies.

Also note that, guaranteeing RMC against upper and lower bounds of the uncertainty region on the Bode plot only does not necessarily guarantee RMC against all the possible uncertainties. This can be seen in Fig. 4.18b since the disk would be much smaller if it is designed only against the upper and lower bound at this frequency as indicated by the two black dots on the solid curves. The reason is that

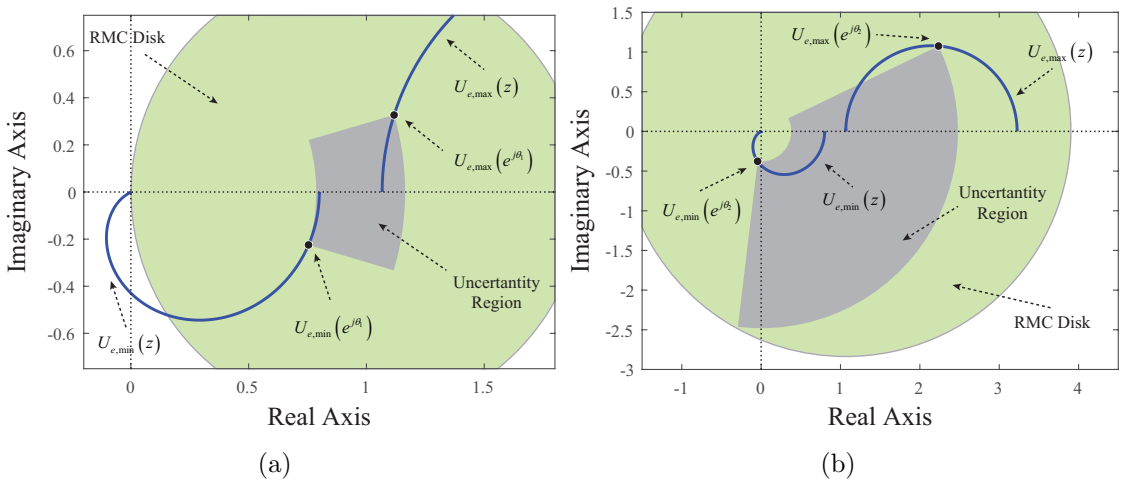

Figure 4.18: Achieving RMC for the example modeling uncertainty region: (a) at ω_1 and (b) at ω_2

the worst-case scenario on the Bode plot does not necessarily refer to the worst-case scenario on the Nyquist plot.

4.2.3 Simulation Examples

In this section, two simulation examples are used to demonstrate the utility of the developed frequency-dependent filter design approach. All the systems and filters have the sampling time $T_s = 0.001$s and a total time steps $N = 6000$. The tracking reference signal is a sinusoid at a frequency of 15 rad/s for the first example and is a sinusoid at a frequency of 10 rad/s for the second example. These two examples demonstrate the utility of the graphical design technique described in Section 4.2 for a robust monotonic convergent NO-ILC in the presence of model uncertainty. Specifically, the first example deals with a positive real model uncertainty, a case in which the Q-filter is not necessary for RMC and therefore perfect tracking can be achieved. The second example deals with a non-positive real model uncertainty, a case in which the Q-filter has to be used for RMC and thus some steady state error is introduced. Note that for all the cases, the total time horizon length $N = 6000$ is picked at least five times longer than the length of the non-zero impulse response of

$G_o(z)$, $W_1(z)$, $W_2(z)$, $W_3(z)$, thus the infinite time horizon analysis presented in this thesis provides a good analysis and design tool.

4.2.3.1 Example 1

Consider a nominal plant, $G_o(z)$:

$$G_o(z) = \frac{0.9975z}{z - 0.995} \times 10^{-3} \tag{4.27}$$

The Bode plot of the nominal plant is shown in Fig. 4.19 indicated as the solid curve. Suppose there exists a positive real modeling error, which lies inside the range shown as the gray region in Fig. 4.19. The upper and lower bounds of the model uncertainty $U_{e,\max}(z)$ and $U_{e,\min}(z)$, shown as the dashed curve in Fig. 4.19, have the following form:

$$U_{e,\max}(z) = \frac{3z - 2.976}{z - 0.9763}; \quad U_{e,\min}(z) = \frac{0.4z - 0.392}{z - 0.99} \tag{4.28}$$

As Fig. 4.19 illustrates, the model is accurate at the low frequency range, whereas the model accuracy starts to degrade at frequencies above 5 rad/s. Note that the real system, $G(z) = U_e(z)G_o(z)$, can be any transfer function that lies inside the gray region in Fig. 4.19. In this case, three example modeling errors are picked:

$$\begin{aligned} U_{e,1}(z) &= U_{e,\max}(z) \\ U_{e,2}(z) &= \frac{2.25z^2 - 4.438z + 2.188}{z^2 - 1.961z + 0.9618} \\ U_{e,3}(z) &= \frac{1.364z^2 - 2.678z + 1.323}{z^2 - 1.966z + 0.9666} \end{aligned} \tag{4.29}$$

As discussed in Section 4.2.2, $W_3(z)$ is not needed for the purpose of RMC, because the model uncertainty is positive real. This can be seen from the uncertainty range in the Bode plot, since the phase difference between any uncertain plant and the system

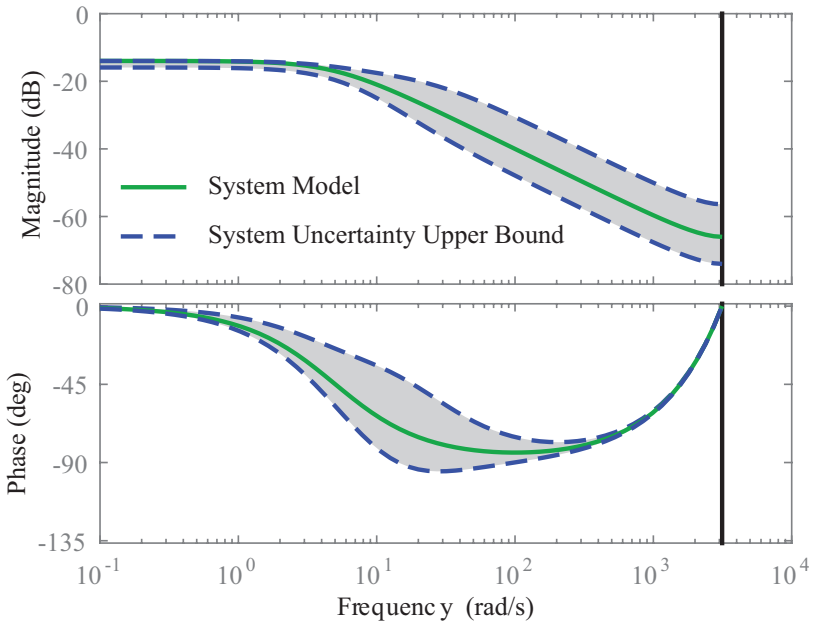

Figure 4.19: Bode plot of $G(z)$, $G_o(z)$, $G_{\max}(z)$, $G_{\min}(z)$ and uncertainty region for Example 1

model never exceeds ± 90 degrees. $W_2(z)$ should be designed as a low pass filter, since the model uncertainty is large at higher frequencies. Following the design guidelines in Section 4.2.2, the filters are designed as $W_1(z) = 1$, $W_3(z) = 0$ and

$$W_2(z) = \frac{0.02z - 0.01901}{z - 0.9802} \tag{4.30}$$

so that the possible uncertainty region lies inside the RMC disk at all frequencies. As an example, the disk plots at two frequencies, one above and one below the reference frequency, are shown in Fig. 4.20. Fig. 4.20a is for $\omega = 3.72$ rad/s and Fig. 4.20b is at $\omega = 16.63$ rad/s. The black dots indicate the values of $U_{e,\max}(e^{j\theta})$ and $U_{e,\min}(e^{j\theta})$ on the complex plane at the corresponding frequencies. The gray region in Fig. 4.20 indicates the model uncertainty range, which corresponds to the gray region in Fig. 4.19 at this specific frequency. In both frequencies shown, the RMC criterion is satisfied, since the green disk includes the gray region. The same holds for all frequencies. Therefore, for all the possible modeling errors, the designed NO-ILC

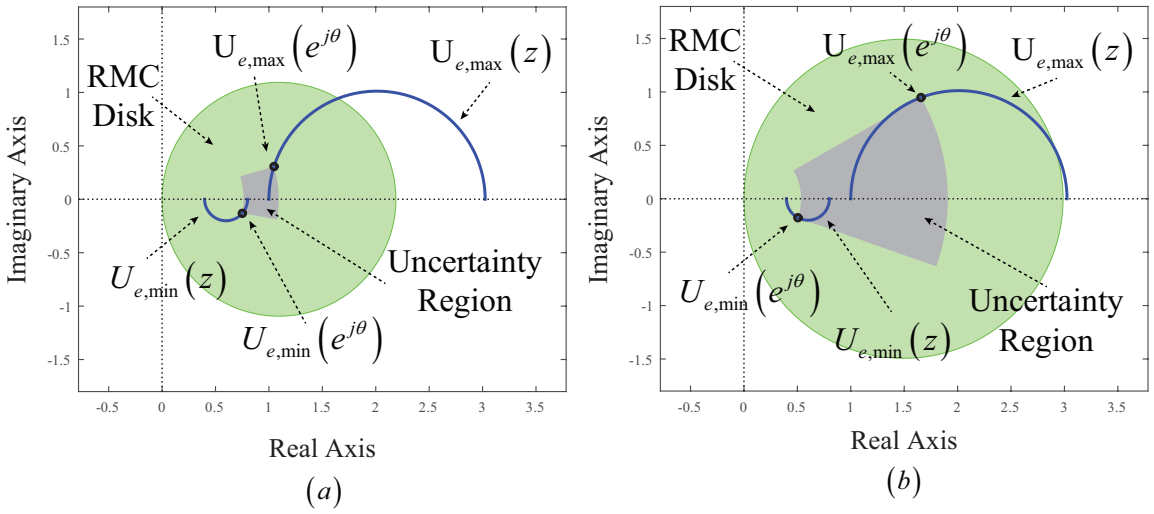

Figure 4.20: RMC disks for Example 1 at different frequencies: (a) 3.72 rad/s (b) 16.63 rad/s

algorithm will be robust monotonic convergent.

With this filter design, the tracking error in the iteration domain is shown in Fig. 4.21. Remember that the tracking error and input difference are defined as following:

$$\begin{aligned} \text{Tracking Error} &\triangleq \mathbf{y}_d - \mathbf{y}_i \\ \text{Input Difference} &\triangleq \mathbf{u}_i - \mathbf{u}_\infty \end{aligned} \tag{4.31}$$

As shown in Fig. 4.21, both the tracking error and input difference are monotonically decreasing as the iteration number increases.

4.2.3.2 Example 2

In this example, the following nominal plant, $G_o(z)$, is used:

$$G_o(z) = \frac{0.398z^2 + 0.96z}{z^2 - 1.995z + 0.995} \times 10^{-3} \tag{4.32}$$

Similar to the previous example, the Bode plots of the nominal plant and uncertainty range are shown in Fig. 4.22. The lower bound of model uncertainty, $U_{e,\min}(z)$,

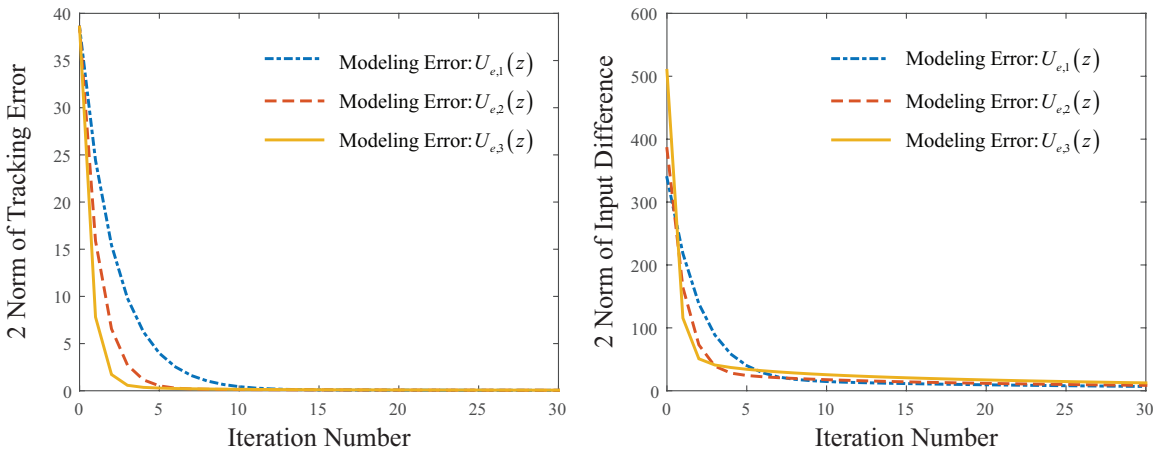

Figure 4.21: Monotonic convergence of tracking error and input difference in the iteration domain for Example 1

in this case has the following form:

$$U_{e,\min}(z) = \frac{1.178z - 0.7854}{z^2 - 1.96z + 0.9608} \times 10^{-3} \tag{4.33}$$

The upper bound of the model uncertainty is $U_{e,\max}(z) = 1$. Three example modeling errors are picked:

$$\begin{aligned} U_{e,1}(z) &= U_{e,\min}(z) \\ U_{e,2}(z) &= \frac{(4.573z^2 - 7.492z + 2.964) \times 10^{-3}}{z^3 - 2.847z^2 + 2.699z - 0.8521} \\ U_{e,3}(z) &= \frac{1.111z^2 - 1.655z + 0.5879}{z^2 - 1.96z + 0.9608} \times 10^{-2} \end{aligned} \tag{4.34}$$

In this case, $W_3(z)$ is not needed for the low frequencies, because all the possible modeling errors are in the right half plane at low frequencies. However, $W_3(z)$ is needed at high frequencies, since some component of the possible modeling error lies in the left half plane at high frequencies. Following the design guidelines in Section

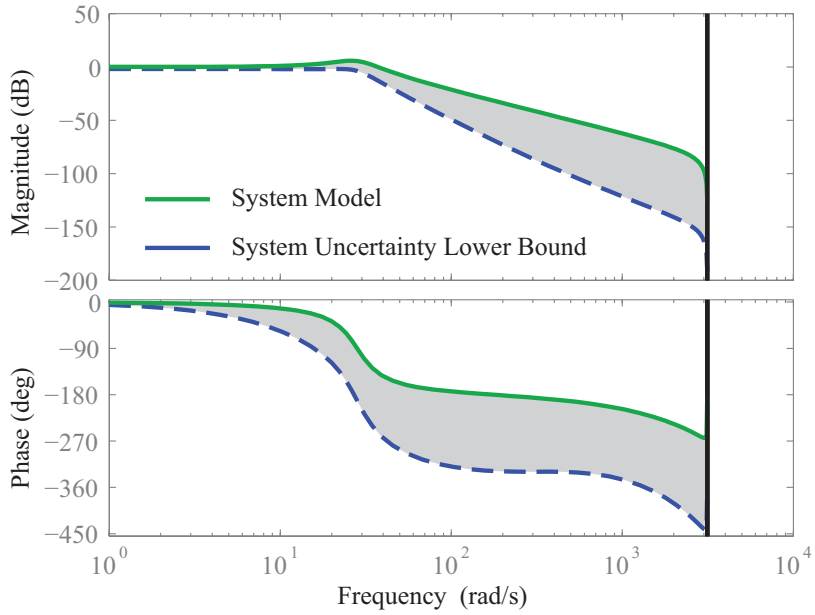

Figure 4.22: Bode plot of $G(z)$, $G_o(z)$, $G_{\max}(z)$, $G_{\min}(z)$ and uncertainty region for Example 2

4.2.2, the filters are designed as $W_1(z) = 1$, $W_2(z) = 0.1$ and

$$W_3(z) \quad = \quad 10^{-3} \quad \times \quad \frac{0.4137z^2 + 0.8274z^3 + 0.0122z^2 + 0.803z - 0.4015}{z^5 - 4.94z^4z + 9.761z^3 - 9.644z^2 + 4.765z - 0.9418} \tag{4.35}$$

so that the possible modeling error lies inside the RMC disk for all frequencies.

The RMC disk plots at two example frequencies are shown in Fig. 4.23. Fig. 4.23a is at 7.90 rad/s and Fig. 4.23b is at 31.51 rad/s.

The tracking error and input difference in the iteration domain are shown in Fig. 4.24. Since the value of $\left|W_3(e^{j\theta})\right|$ is non-zero at 10 rad/s, which is the frequency of tracking reference signal, a steady state tracking error is expected. Also note that the 2-norm of the input difference is decreasing monotonically, confirming that the design has RMC against the given uncertainty range.

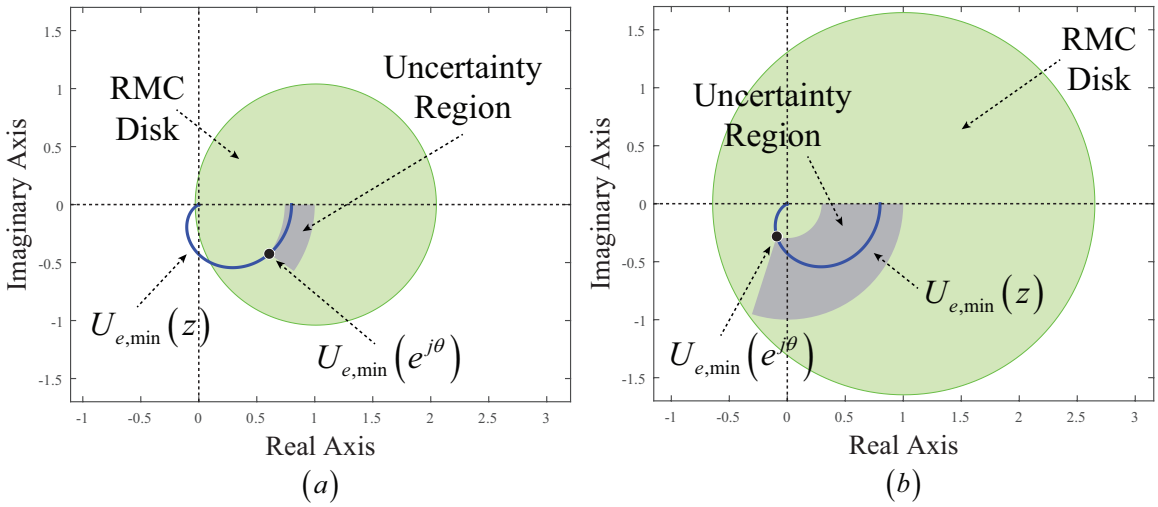

Figure 4.23: RMC disk for Example 2 at different frequencies: (a) 7.90 rad/s (b) 31.51 rad/s

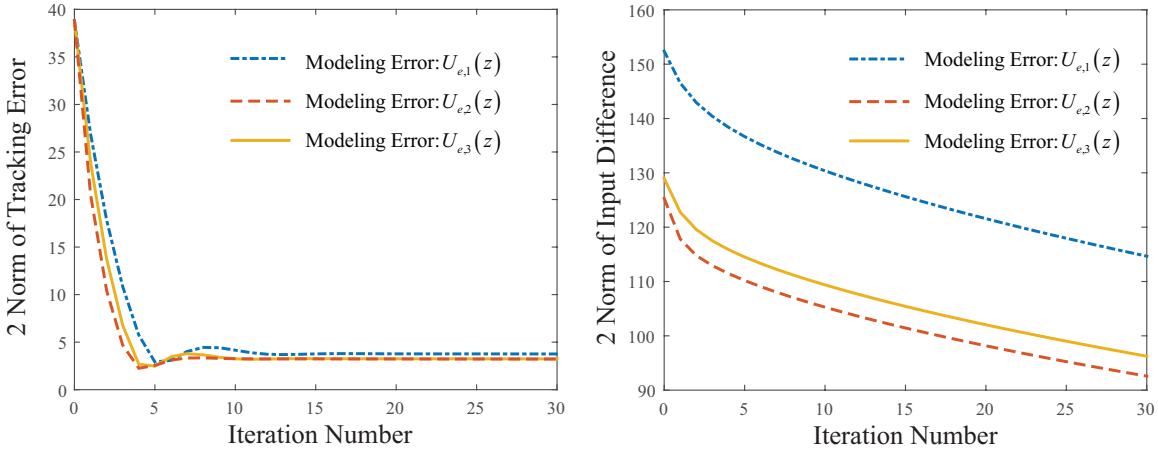

Figure 4.24: Tracking error and input difference in iteration domain for Example 2

4.3 Conclusion

Using the new model uncertainty formulation presented in Chapter III, which incorporates additional phase information compared with the traditional one, a frequency domain analysis on the RMC of NO-ILC has been developed to explain the relationships between RMC against the modeling errors and the NO-ILC weighting filters.

The first section of this chapter derives a **sufficient condition** for the RMC criterion for scalar NO-ILC wighting filters, which leads to a graphical characterization of the allowable modeling error on the Nyquist plot. The relationship between the RMC region and the scalar weighting filters is analyzed. The analysis points out how the RMC region changes with respect to different NO-ILC weighting parameters λ and β. Therefore, this tool can be used as a frequency domain design method for robust monotonic convergent NO-ILC against model uncertainties. Three simulation examples are presented to demonstrate the effectiveness of the proposed design method.

The second section extends the analysis in the previous section in two aspects. First, a **necessary and sufficient condition** is derived for the RMC criterion for NO-ILC. Second, the scalar weighting filter design is extended to general LTI weighting filter designs. The RMC region is also interpreted on Nyquist plot and the relationship between the RMC region and weighting filters is analytically characterized. The analysis leads to a more aggressive design technique, which better addresses the trade-off between robustness, convergence speed and steady state error at different frequencies that is discussed in the next chapter.

CHAPTER V

Fundamental Trade-off of NO-ILC and Its Optimality

The discussions in the previous chapter focus on design methodologies for RMC against model uncertainty. However, robustness is not the only concern when designing NO-ILC. Besides robustness, convergence speed and steady state error are also important performance criterion. A good NO-ILC design should have just enough robustness against the model uncertainty and, at the same time, maximize the convergence speed and minimize the steady state error. Therefore, it is important to understand the trade-off between robustness, convergence speed and steady state error for NO-ILC. In the literature, some qualitative statements about this trade-off already exist. In this chapter, through the frequency domain analysis, a quantitative characterization of this trade-off is presented for the first time.

Given the fact that NO-ILC is subject to this fundamental trade-off, it is interesting to ask whether other LTI ILC updating laws can bypass this trade-off. It is demonstrated that the answer is **no**. In another word, NO-ILC is the optimal solution in terms of addressing the trade-off between robustness, convergence speed and steady state error among LTI ILC updating laws. The proof of this optimality is presented in the second half of this chapter.

5.1 Fundamental Trade-off Between Robustness, Convergence Speed and Steady State Error

Against any modeling error, $U_e(z)$, diagonal weightings can be used in the cost function to ensure RMC for NO-ILC; i.e., $Q = I$, $R = \lambda I$ and $S = \beta I$, which corresponds to $W_1(z) = 1$, $W_2(z) = \sqrt{\lambda}$ and $W_3(z) = \sqrt{\beta}$. However, robustness is not the only concern, since convergence speed and steady state error are also important factors. A fundamental trade-off exists between robustness, convergence speed and steady state error, and using frequency dependent weightings in the cost function helps better address this trade-off. This section shows the analytical relationship among these three performance criteria at each frequency for any robust monotonic convergent NO-ILC using the cost function, Eq. (1.1).

To this end, the robustness, convergence speed and steady state tracking error for NO-ILC are first defined at each frequency.

5.1.1 Robustness

Robustness is defined as the allowable modeling error for a specific NO-ILC design. In this work, RMC region is used to quantify the robustness of NO-ILC. As discussed in the previous chapter, the RMC region at each frequency is a disk. Hence, the radius of this disk is used in this work to characterize the robustness. Larger disk radius corresponds to larger robustness. Thus, at each frequency, robustness, denoted as RB(θ) here, is defined as the following:

$$\mathrm{RB}\left(\theta\right) \triangleq r\left(\theta\right) = \frac{\left|W_1\left(e^{j\theta}\right)\right|^2\left|G_o\left(e^{j\theta}\right)\right|^2 + \left|W_2\left(e^{j\theta}\right)\right|^2 + \left|W_3\left(e^{j\theta}\right)\right|^2}{\left|W_1\left(e^{j\theta}\right)\right|^2\left|G_o\left(e^{j\theta}\right)\right|^2} \tag{5.1}$$

Note that the robustness, RB(θ), is a number that lies in the interval $[1, \infty)$. This is consistent with the fact that the radius of the RMC disk for NO-ILC is guaranteed to be larger than one, because when $W_2(z) = W_3(z) = 0$, NO-ILC is the same as

plant inversion and the RMC disk radius in this case is one (*Harte et al.*, 2005).

5.1.2 Convergence Speed

Convergence speed denotes how fast the input sequence converges. Before giving the definition of convergence speed, the concept of convergence ratio is first introduced. Convergence ratio, $\mathrm{CR}(\theta)$, is a ratio defined as:

$$\mathrm{CR}\left(\theta\right) \triangleq \left| \frac{u_{i+1}\left(e^{j\theta}\right) - u_{\infty}\left(e^{j\theta}\right)}{u_i\left(e^{j\theta}\right) - u_{\infty}\left(e^{j\theta}\right)} \right| \tag{5.2}$$

where $u_{\infty}(z)$ denotes the input sequence when ILC converges. From the frequency domain updating law, Eq. (2.15), and considering the nominal performance, i.e., there is no model uncertainty, the following equation can be derived:

$$u_{i+1}(z) - u_{\infty}(z) = \left(\mathcal{Q}(z) - \mathcal{L}(z)G_o(z)\right)\left(u_{i+1}(z) - u_{\infty}(z)\right) \tag{5.3}$$

Therefore, the convergence ratio becomes:

$$\begin{aligned} \mathrm{CR}(\theta) &= \left|\mathcal{Q}(e^{j\theta}) - \mathcal{L}(e^{j\theta})G_o(e^{j\theta})\right| \\ &= \frac{\left|W_2\left(e^{j\theta}\right)\right|^2}{\left|W_1\left(e^{j\theta}\right)\right|^2\left|G_o\left(e^{j\theta}\right)\right|^2 + \left|W_2\left(e^{j\theta}\right)\right|^2 + \left|W_3\left(e^{j\theta}\right)\right|^2} \end{aligned} \tag{5.4}$$

Note that the convergence ratio, $\mathrm{CR}(\theta)$, is a number in the interval $[0, 1)$. $\mathrm{CR}(\theta) = 1$ means the input sequence is not converging, while $\mathrm{CR}(\theta) = 0$ means the input sequence converges infinitely fast, like a dead-beat control in the iteration domain. The convergence speed, $\mathrm{CS}(\theta)$, is then defined as:

$$\begin{aligned} \mathrm{CS}(\theta) &\triangleq 1 - \mathrm{CR}(\theta) \\ &= \frac{\left|W_1\left(e^{j\theta}\right)\right|^2\left|G_o\left(e^{j\theta}\right)\right|^2 + \left|W_3\left(e^{j\theta}\right)\right|^2}{\left|W_1\left(e^{j\theta}\right)\right|^2\left|G_o\left(e^{j\theta}\right)\right|^2 + \left|W_2\left(e^{j\theta}\right)\right|^2 + \left|W_3\left(e^{j\theta}\right)\right|^2} \end{aligned} \tag{5.5}$$

Thus, convergence speed, $\mathrm{CS}(\theta)$, is also a number that lies in the interval $(0, 1]$. $\mathrm{CS}(\theta) = 0$ means the input sequence is not converging, whereas $\mathrm{CS}(\theta) = 1$ means the input sequence is converging infinitely fast.

Note that the definition of convergence speed, Eq. (5.5), is for steady state signals. Transient signals always exist and the worst-case convergence ratio in terms of the 2-norm of the input sequence is $|\mathcal{Q}(z) - \mathcal{L}(z)G_o(z)|_\infty$ according to Parseval's Theorem, which has been widely used in the ILC literature to characterize the convergence speed. However, $|\mathcal{Q}(z) - \mathcal{L}(z)G_o(z)|_\infty$ does not provide any information about the frequency components. In many cases, this leads to a conservative estimation of the convergence speed.

5.1.3 Steady State Error

It is well-known in the literature that even if the nominal performance of NO-ILC converges, a steady state error exists if $\mathcal{Q}(z) \neq 1$. In this paper, the steady state error, $\mathrm{SSE}(\theta)$, for each frequency, θ, is defined as:

$$\mathrm{SSE}(\theta) \triangleq \left| \frac{u_d\left(e^{j\theta}\right) - u_\infty\left(e^{j\theta}\right)}{u_d\left(e^{j\theta}\right)} \right| \tag{5.6}$$

where $u_d(z)$ denotes the ideal input that achieves perfect tracking. Note that $u_d(z)$ is unknown in general. However, from the frequency domain updating law, Eq. (2.15), one can obtain the following equation:

$$\mathrm{SSE}(\theta) = \frac{\left|W_3\left(e^{j\theta}\right)\right|^2}{\left|W_1\left(e^{j\theta}\right)\right|^2 \left|G_o\left(e^{j\theta}\right)\right|^2 + \left|W_3\left(e^{j\theta}\right)\right|^2} \tag{5.7}$$

Note that the steady state error is a number in the interval $[0, 1]$. $\mathrm{SSE}(\theta) = 0$ means the input converges to the ideal one at this frequency, while $\mathrm{SSE}(\theta) = 1$ means the input signal is zero. Also note that when $W_3(e^{j\theta}) = 0$, $\mathrm{SSE}(\theta) = 0$, which is consistent with the fact that there will be no steady state error if Q-filter is not used;

i.e., $\mathcal{Q}(z) = 1$.

5.1.4 Expressing the Fundamental Trade-off for NO-ILC

In the previous sections, mathematical expressions for robustness $\mathrm{RB}(\theta)$, convergence speed $\mathrm{CS}(\theta)$ and steady state error $\mathrm{SSE}(\theta)$ at each frequency have been defined. In this section, the relationship between these three terms is analytically expressed. This relationship is a fundamental trade-off for the nominal performance of NO-ILC.

From Eq. (5.1), (5.5) and (5.7), it can be shown that the robustness, convergence speed and steady state error at each frequency for NO-ILC satisfy the following relationship:

$$\frac{1}{\mathrm{CS}(\theta)\mathrm{RB}(\theta)} + \mathrm{SSE}(\theta) = 1 \tag{5.8}$$

The significance of the above equation is that it quantitatively describes the trade-off between robustness, convergence speed and steady state error of NO-ILC at each frequency. This equation is analogous to the fundamental trade-off $S(\theta)+T(\theta) = 1$ in feedback control, where $S(\theta)$ is the sensitivity function and $T(\theta)$ is the complementary sensitivity function at each frequency θ. The design of NO-ILC is a design of balancing the abovementioned trade-off.

For a NO-ILC design with $W_3(e^{j\theta}) = 0$, $\mathrm{SSE}(\theta)$ is zero, and the robustness and convergence speed have an inverse relationship as shown by the solid curve in the Fig. 5.1a. Note that, as discussed earlier, NO-ILC in this case guarantees a minimum robustness of 1. As $W_3(e^{j\theta})$ increases, $\mathrm{SSE}(\theta)$ increases, which shifts the curve up, as shown by the dashed curve in Fig. 5.1a.

For a NO-ILC design with $W_2(e^{j\theta}) = 0$, $\mathrm{CS}(\theta)$ is one according to Eq. (5.5). From Eq. (5.8), it follows that $\mathrm{RB}(\theta) = 1/(1 - \mathrm{SSE}(\theta))$ as shown by the solid curve in the Fig. 5.1b. As $W_2(e^{j\theta})$ increases, $\mathrm{CS}(\theta)$ decreases, which shifts the curve up, as shown by the dashed curve in Fig. 5.1b.

For the purpose of better visualizing the fundamental trade-off of NO-ILC char-

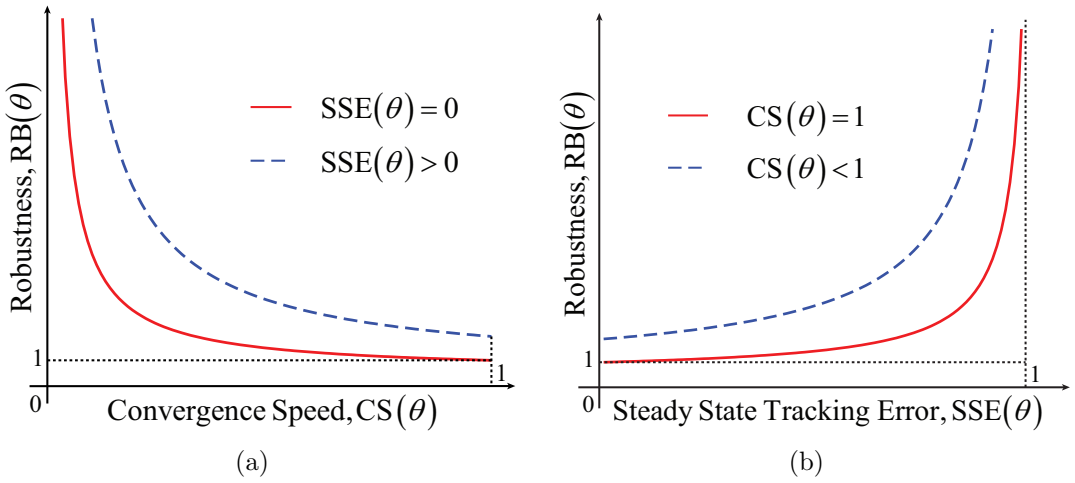

Figure 5.1: Illustration of the trade-off between (a) convergence speed and robustness, and (b) steady state error and robustness

acterized by Eq. (5.8), a 3D Pareto plot of the three performance metrics of NO-ILC is shown in Fig. 5.2. At each frequency, robustness, convergence speed and steady state error lie on the Pareto surface. Note that the most aggressive NO-ILC (plant inversion), i.e., $W_2(e^{j\theta}) = W_3(e^{j\theta}) = 0$, is at the point of the surface with $\mathrm{SSE}(\theta) = 0$, $\mathrm{CS}(\theta) = 1$ and $\mathrm{RB}(\theta) = 1$.

This fundamental trade-off analysis can be used in the NO-ILC to design for optimal performance at each frequency according to various robustness, convergence speed and steady state error requirements.

5.1.5 Simulation Example

In this example, the nominal performance of NO-ILC is analyzed. The performance of NO-ILC is compared between using the proposed frequency-dependent filter design method, , as discussed in Section 4.2, and using diagonal weighting matrices, as discussed in Section 4.1. Eq. (5.8) shows that robustness, convergence speed and steady state error cannot be improved at the same time at a given frequency. Therefore, the design of NO-ILC needs to balance the trade-off between the above-mentioned quantities according to different requirements at different frequencies. This

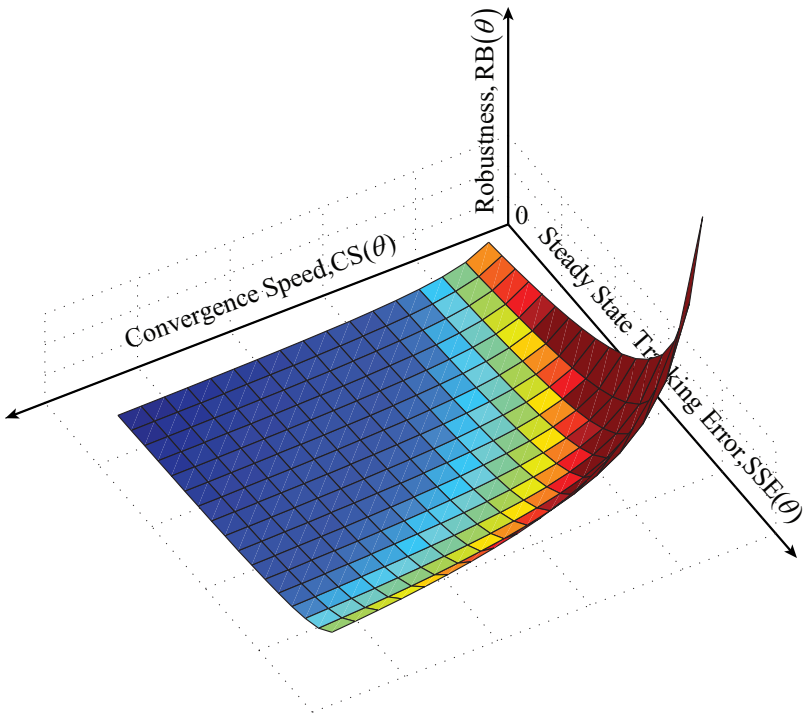

Figure 5.2: Performance surface for NO-ILC

example is built on the scenario that the diagonal weighting matrix design is required to meet at least the robustness that has been achieved by using the proposed filter design. The results show that either convergence speed or steady state error comes as a sacrifice when diagonal weighting matrices are used. All the systems and filters have the sampling time $T_s = 0.001$s and a total time steps $N = 6000$, which is at least five times longer than the length of the non-zero impulse response of $G_o(z)$, $W_1(z)$, $W_2(z)$, $W_3(z)$, thus the infinite time horizon analysis presented in this paper provides a good analysis and design tool.

Two nominal plants are used in this section:

$$\begin{aligned} G_{o,Ex_1}(z) &= \frac{0.9975z}{z - 0.995} \times 10^{-3} \\ G_{o,Ex_2}(z) &= \frac{0.398z^2 + 0.396z}{z^2 - 1.995z + 0.995} \times 10^{-3} \end{aligned} \tag{5.9}$$

Consider the first nominal plant in Eq. (5.9), $G_{o,Ex_1}(z)$. In Section 4.2.3.1, a

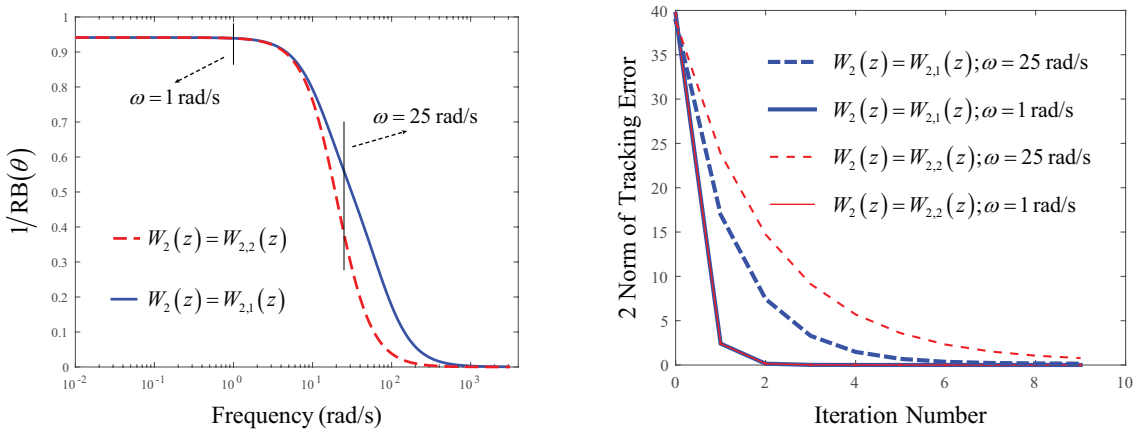

Figure 5.3: (a) Robustness at different frequency for $W_{2,1}(z)$ and $W_{2,2}(z)$ and (b) 2 norm of tracking error in iteration domain

NO-ILC filter design has been proposed with:

$$\begin{aligned} W_1(z) &= 1 \\ W_{2,1}(z) &= \frac{0.02z - 0.01901}{z - 0.9802} \\ W_3(z) &= 0 \end{aligned} \tag{5.10}$$

for the nominal plant $G_{o,Ex_1}(z)$. Let $W_1(z)$ and $W_3(z)$ be the same but use $W_2(z) = W_{2,2}(z) = \sqrt{\lambda}$ to guarantee that its robustness at each frequency is no smaller compared with the previous design. As discussed in the previous section, the robustness at each frequency, RB (θ), is characterized using Eq. (5.1). The smallest value of $\sqrt{\lambda}$ in this case is 0.5, which is the DC gain of $W_{2,1}(z)$. The robustness, RB (θ), with respect to different frequencies for the two designs is shown in Fig. 5.3a.

In this case, since $W_3(z) = 0$, which means there will be no steady state error, the results show how the robustness and convergence speed are related at different frequencies with different $W_2(z)$ designs. At 1 rad/s, using $W_2(z) = W_{2,1}(z)$ and $W_2(z) = W_{2,2}(z)$ gives the same robustness as shown in Fig. 5.3a. The convergence speed of these two different designs is almost the same at this specific frequency as shown in Fig. 5.3b, since the thin solid line and the thick solid line overlap with

each other. At the frequency of 25 rad/s, the robustness with $W_2(z) = W_{2,2}(z)$ is larger compared with the robustness of the design with $W_2(z) = W_{2,1}(z)$ as shown in Fig. 5.3a. According to the fundamental trade-off analysis in the previous section, larger robustness at this frequency corresponds to slower convergence speed. This is consistent with the results shown in Fig. 5.3b, since the thin dashed line (with a design of $W_2(z) = W_{2,2}(z)$) converges slower than the thick dashed line (with a design of $W_2(z) = W_{2,1}(z)$).

The relationship between robustness and convergence speed can also be evaluated quantitatively according to Eq. (5.8) for this example, since the steady state error is zero. At the frequency of 1 rad/s, $(\mathrm{RB}(\theta))^{-1}$ for both designs is 0.939 as shown in Fig. 5.3a. According to Eq. (5.8), a convergence speed of 0.939 is expected, which corresponds to a convergence ratio of 0.061. From Fig. 5.3b, the actual converge ratio is roughly 0.060, confirming the analysis. Similarly, at the frequency of 25 rad/s, $(\mathrm{RB}(\theta))^{-1}$ is 0.383 for $W_{2,2}(z)$ and is 0.560 for $W_{2,1}(z)$. The expected corresponding convergence ratios are 0.617 and 0.440, respectively. The actual convergence ratios can be calculated according to the thin and thick dashed line shown in Fig. 5.3b, which is roughly 0.612 for $W_{2,2}(z)$ and is 0.447 for $W_{2,1}(z)$. This agreement between the theoretical and actual values demonstrates the utility of Eq. (5.8). The minor differences between the theoretical and actual numbers are due to the fact that the frequency domain analysis is for an infinite time horizon, but the simulations are run for a finite time.

Consider the second nominal plant in Eq. (5.9), $G_{o,Ex_2}(z)$. In Section 4.2.3.2, a NO-ILC filter design has been proposed with:

$$\begin{aligned} W_1(z) &= 1 \\ W_2(z) &= 0.1 \\ W_{3,1}(z) &= 10^{-3} \times \frac{0.4137z^2 + 0.8274z^3 + 0.0122z^2 + 0.803z - 0.4015}{z^5 - 4.94z^4z + 9.761z^3 - 9.644z^2 + 4.765z - 0.9418} \end{aligned} \tag{5.11}$$

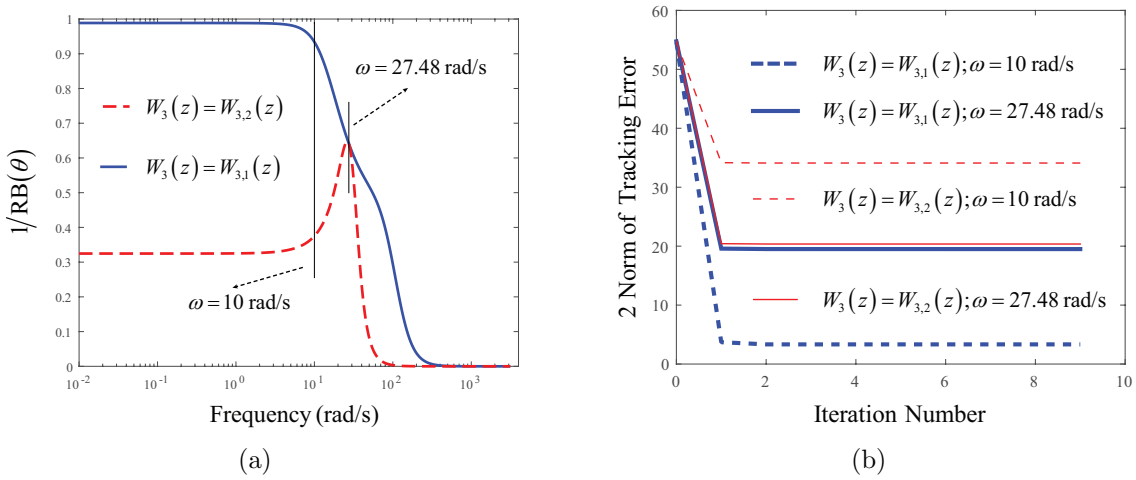

Figure 5.4: (a) Robustness at different frequencies for $W_{3,1}(z)$ and $W_{3,2}(z)$ and (b) 2 norm of tracking error in iteration domain

for nominal plant $G_{o,Ex_2}(z)$. Let $W_1(z)$ and $W_2(z)$ be the same, but use $W_3(z) = W_{3,2}(z) = \sqrt{\beta}$ to guarantee that its robustness at each frequency is no smaller compared with the previous design. The smallest value of $\sqrt{\beta}$ in this case is 1.44. The robustness, RB (θ), with respect to different frequencies for the two designs is shown in Fig. 5.4a.

In this case, since $W_2(z) = 0.1$ is quite small compared with $W_3(z)$ and $G_{o,Ex_2}(z)$, which means the learning will be very fast, the results can be studied to see how the robustness and steady state error are related at different frequencies with different $W_3(z)$ designs. At 27.8 rad/s, using $W_3(z) = W_{3,1}(z)$ and $W_3(z) = W_{3,2}(z)$ gives the same robustness as shown in Fig. 5.4a. The steady state errors of these two different designs are very close at this specific frequency as shown in Fig. 5.4b. At frequency of 10 rad/s, the robustness with $W_3(z) = W_{3,1}(z)$ is larger compared with the robustness of the design with $W_3(z) = W_{3,2}(z)$ as shown in Fig. 5.4a. According to the fundamental trade-off analysis in the previous section, larger robustness at this frequency corresponds to a larger steady state error. This is consistent with the results shown in Fig. 5.4b, since the thin dashed line (with a design of $W_3(z) = W_{3,2}(z)$) converges to a larger steady state error than the thick dashed line (with a design of

$W_3(z) = W_{3,1}(z)$).

The relationship between robustness and steady state error can be quantitatively investigated based on these simulation results since $\text{CS}(\theta) \approx 1$ in this scenario. At the frequency of 27.48 rad/s, $(\text{RB}(\theta))^{-1}$ for both designs is 0.642 as shown in Fig. 5.4a. According to Eq. (5.8), a steady state error of 0.358 is expected. From Fig. 5.4b, the actual steady state error is 0.356 for $W_{3,1}(z)$ and 0.372 for $W_{3,2}(z)$. Similarly, at the frequency of 10 rad/s, $(\text{RB}(\theta))^{-1}$ is 0.934 for $W_{3,1}(z)$ and 0.375 for $W_{3,2}(z)$. The expected steady state errors are 0.066 and 0.625, respectively. The actual steady state errors are roughly 0.061 for $W_{3,1}(z)$ and 0.624 for $W_{3,2}(z)$. This agreement between the theoretical and actual values illustrates the utility of Eq. (5.8).

Fig. 5.4 shows that the learning speed for all cases is very fast because $W_2(z)$ is small and this is consistent with Eq. (5.5). Also note that, theoretically, the steady state error in the iteration domain for this case at frequency of 27.48 rad/s should be the same for an infinite time horizon. Note that the frequency domain analysis for NO-ILC is for infinite time horizon, whereas NO-ILC is always implemented in finite time horizon in the time domain. The small difference between the red solid line and the blue solid line in Fig. 5.4b is due to the transients in the time domain. Since $W_3(z)$ used is different, this leads to different transients in the time domain. Fig. 5.5 shows the error signal in the time domain for both designs at the 10th iteration. Notice that the transients occur at both the beginning and ending due to the zero-phase filter nature of NO-ILC. In this case, the transients with the design of $W_3(z) = W_{3,1}(z)$ are smaller than the transients with the design of $W_3(z) = W_{3,2}(z)$. Therefore, a smaller steady state error in the iteration domain is expected with the design of $W_3(z) = W_{3,1}(z)$ as shown in Fig. 5.4b.

In conclusion, for the nominal performance, using the proposed frequency-dependent filter design in NO-ILC can lead to more degrees of freedom to design the NO-ILC performance, i.e., robustness, convergence speed and steady state error, at different

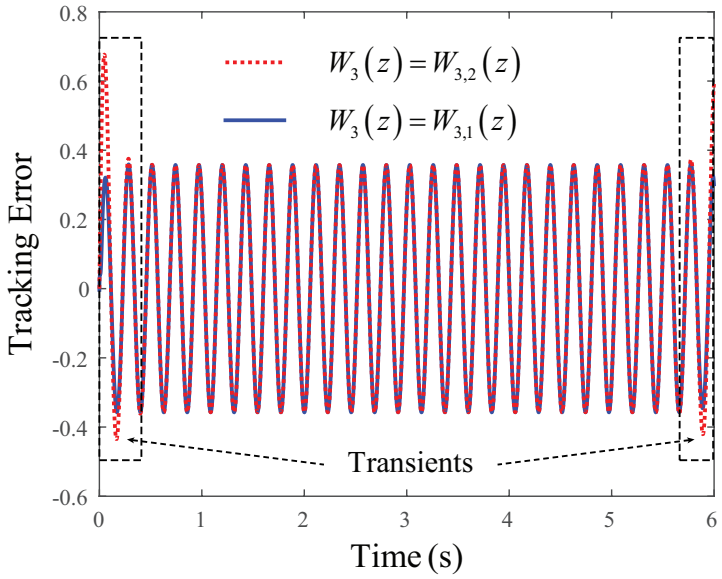

Figure 5.5: Comparison of the tracking error for $G_{o,Ex2}$ with different $W_3(z)$ designs at 27.48 rad/s after 10th iteration

frequencies compared with NO-ILC design with constant weighting matrices.

5.2 Optimality of NO-ILC

The previous section quantitatively presents the fundamental trade-off between robustness, convergence speed and steady state error at each frequency for NO-ILC for Single-Input-Single-Output (SISO) system. An interesting question that naturally follows is whether this fundamental trade-off also exists for general LTI ILC updating laws:

$$u_{i+1}(z) = \mathcal{Q}(z)u_i(z) + \mathcal{L}(z)e_i(z) \tag{5.12}$$

In this section, it is shown that, for general LTI ILC updating laws, there exists some quantifiable relationship between the three performance indices at each frequency. Furthermore, in the scope of LTI ILC updating laws, NO-ILC is the optimal solution in terms of balancing the trade-off between these three performance indexes over all the frequencies.

In this section, first, the results will be presented in a case where the Q-filter is

disabled in the updating law Eq. (5.12). Then, the results will be generalized to the scenarios where the Q-filter is used.

5.2.1 Without Q-Filter

In this section, the following LTI ILC updating law will be considered:

$$u_{i+1}(z) = u_i(z) + \mathcal{L}(z)e_i(z) \tag{5.13}$$

Since the Q-filter is disabled in this scenario, there will be no steady state error if the ILC converges. In the following two sections, the question of how much model uncertainty can be tolerated will be explored and then the relationship between the robustness and convergence speed will be addressed.

5.2.1.1 How Much Uncertainty Can Be Tolerated?

In this section, the research question of how much model uncertainty can be tolerated will be answered. Plugging $\mathcal{Q}(z) = 1$ into the RMC criterion Eq. (3.2), the following can be obtained:

$$\left|1 - U_e\left(e^{j\theta}\right) G_o\left(e^{j\theta}\right) \mathcal{L}\left(e^{j\theta}\right)\right| < 1, \quad \forall\theta \in [0, 2\pi] \tag{5.14}$$

Let the complex numbers, $G_o\left(e^{j\theta}\right) \mathcal{L}\left(e^{j\theta}\right)$ and $U_e\left(e^{j\theta}\right)$, be:

$$\begin{aligned} U_e\left(e^{j\theta}\right) &\triangleq x(\theta) + jy(\theta) \\ G_o\left(e^{j\theta}\right) \mathcal{L}\left(e^{j\theta}\right) &\triangleq m(\theta) + jn(\theta) \end{aligned} \tag{5.15}$$

where $x(\theta)$, $m(\theta)$ and $y(\theta)$, $n(\theta)$ denote the real and complex parts of $U_e\left(e^{j\theta}\right)$ and $G_o\left(e^{j\theta}\right) \mathcal{L}\left(e^{j\theta}\right)$ respectively. Substituting the above equations into Eq. (5.14) gives

the following:

$$(x(\theta) - c_x(\theta))^2 + (y(\theta) - c_y(\theta))^2 < r(\theta), \quad \forall\theta \in [0, 2\pi) \tag{5.16}$$

where $(c_x(\theta), c_y(\theta))$ and $r(\theta)$ denote the center and radius of a disk. They are functions of $m(\theta)$ and $n(\theta)$ as shown in the following:

$$\begin{aligned} c_x(\theta) &= \frac{m(\theta)}{m^2(\theta) + n^2(\theta)} \\ c_y(\theta) &= -\frac{n(\theta)}{m^2(\theta) + n^2(\theta)} \\ r(\theta) &= \frac{1}{\sqrt{m^2(\theta) + n^2(\theta)}} \end{aligned} \tag{5.17}$$

Thus, the allowable model uncertainty can be characterized with a disk centered at $(c_x(\theta), c_y(\theta))$ with a radius of $r(\theta)$ at each frequency θ. As an example shown in Fig. 5.6 at a particular frequency θ_o, the disk is illustrated as the light green region. As long as the model uncertainty $U_e(z)$ lies inside the green disk over all the frequencies, RMC is achieved. The vector $G_o\left(e^{j\theta_o}\right)\mathcal{L}\left(e^{j\theta_o}\right)$ is also illustrated using the red arrow in Fig. 5.6, which is further discussed in the next section.

5.2.1.2 Relationship Between Robustness and Convergence Speed

For the scenario when the Q-filter is disabled, there will not be any steady state error if the ILC converges, which has been well understood in the literature. Therefore, in this section, the relationship between the robustness and convergence speed will be investigated. First, the definitions of robustness and convergence speed will be introduced.

The radius of the disk that describes the allowable modeling uncertainties is used here to characterize the robustness. The definition of the robustness over different

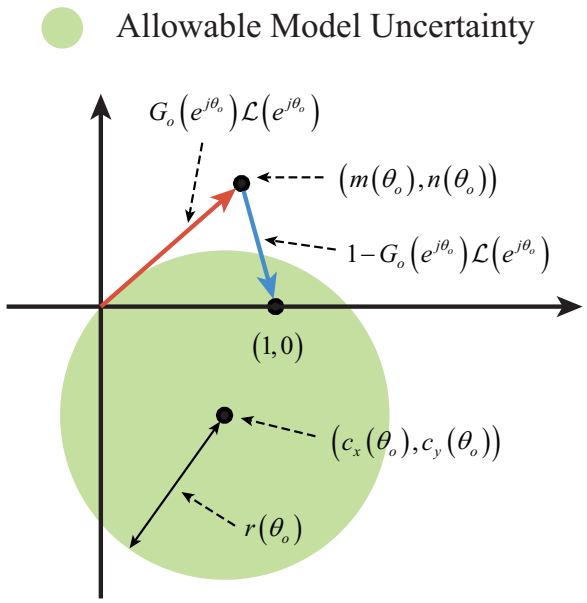

Figure 5.6: Illustration of allowable model uncertainties and the vector $G_o\left(e^{j\theta_o}\right)\mathcal{L}\left(e^{j\theta_o}\right)$ on the complex plane at a particular frequency θ_o

frequencies, $\mathrm{RB}(\theta)$, is shown as following:

$$\mathrm{RB}(\theta) \triangleq r(\theta) = \frac{1}{\left|G_o\left(e^{j\theta}\right)\mathcal{L}\left(e^{j\theta}\right)\right|} \in \left(\frac{\sqrt{2}}{2}, \infty\right) \tag{5.18}$$

As can be seen here, a too large learning gain $\mathcal{L}(\theta)$ potentially leads to a very small robustness since, according to its definition, $\mathrm{RB}(\theta) = \left|G_o\left(e^{j\theta}\right)\mathcal{L}\left(e^{j\theta}\right)\right|^{-1}$. Comparing this to NO-ILC, note that NO-ILC guarantees a minimum robustness of 1 over all the frequencies.

For a robust monotonic convergent ILC updating law, the convergence ratio $\mathrm{CR}(\theta)$ at each frequency θ is defined as following:

$$\mathrm{CR}(\theta) \triangleq \left|1 - G_o\left(e^{j\theta}\right)\mathcal{L}\left(e^{j\theta}\right)\right| \in [0, 1) \tag{5.19}$$

where $\mathrm{CR}(\theta) = 1$ means the ILC is not converging and $\mathrm{CR}(\theta) = 0$ means the ILC

converges rapidly. The definition of convergence speed $\mathrm{CS}(\theta)$ follows immediately:

$$\mathrm{CS}(\theta) \triangleq 1 - \mathrm{CR}(\theta) \in (0, 1] \tag{5.20}$$

where $\mathrm{CS}(\theta) = 1$ means the ILC converges rapidly and $\mathrm{CS}(\theta) = 0$ means the ILC does not converge. The following proposition then characterizes the relationship between robustness and convergence speed at each frequency θ.

Proposition V.1. *For a monotonic convergent ILC updating law Eq. (5.13), its robustness and converge speed satisfy the following relationship:*

$$\frac{1}{\mathrm{RB}(\theta)\,\mathrm{CS}(\theta)} \geq 1, \quad \forall \theta \in [0, 2\pi] \tag{5.21}$$

Proof. See Appendix A for the proof. □

Note that the relationship between robustness and convergence speed for NO-ILC when the Q-filter is disabled has been previously reported in the previous section:

$$\frac{1}{\mathrm{RB}(\theta)\mathrm{CS}(\theta)} = 1, \quad \forall \theta \in [0, 2\pi] \tag{5.22}$$

To this end, the optimality of NO-ILC when the Q-filter is disabled in terms of the trade-off between robustness and convergence speed at each frequency is illustrated in Fig. 5.7. The red curve denotes the Pareto curve for NO-ILC while the gray region indicates the landing point for LTI ILC updating law Eq. (5.13). This demonstrates the optimality of NO-ILC in terms of balancing the trade-off between robustness and convergence speed at each frequency. It is worth mentioning here though that the performance index of the ILC updating law Eq. (5.13) could potentially lie on the the Pareto curve for certain frequencies but NO-ILC guarantees this for all the frequencies.

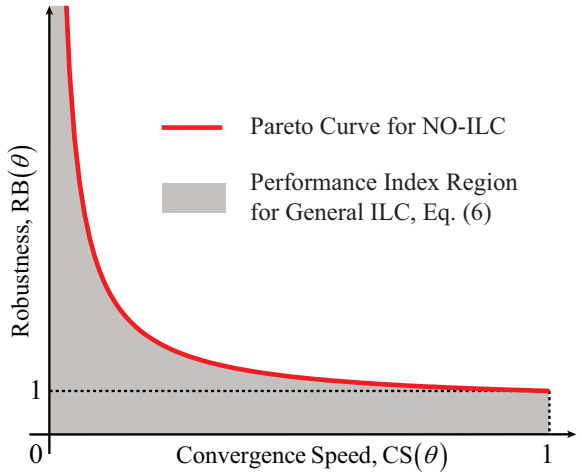

Figure 5.7: Trade-off between robustness and convergence speed for general LTI ILC updating laws when Q-filter is disabled

5.2.2 With Q-Filter

In this section, the results derived in the previous sections are extended for the general case when Q-filter is used in the ILC updating law. Similar to the previous section, the region for the allowable model uncertainty is addressed first followed by the derivation of the relationship between robustness, convergence speed and steady state error.

5.2.2.1 How Much Uncertainty Can Be Tolerated?

Following the similar ideas presented in the previous section, the allowable model uncertainty analysis is extended to a scenario where the Q-filter is used.

The frequency domain RMC criterion Eq. (3.2) can be re-written as:

$$\left|\mathcal{Q}\left(e^{j\theta}\right) - U_e\left(e^{j\theta}\right) G_o\left(e^{j\theta}\right) \mathcal{L}\left(e^{j\theta}\right)\right| < 1, \quad \forall\theta \in [0, 2\pi] \tag{5.23}$$

Define the complex number $\mathcal{Q}\left(e^{j\theta}\right)$ as:

$$\mathcal{Q}\left(e^{j\theta}\right) \triangleq p(\theta) + jq(\theta) \tag{5.24}$$

Pluging Eq. (5.15) and Eq. (5.24) into Eq. (5.23) gives Eq. (5.16) but with $c_x(\theta)$, $c_y(\theta)$ and $r(\theta)$ equal to the followings:

$$\begin{aligned} c_x(\theta) &= \frac{m(\theta)p(\theta) + n(\theta)q(\theta)}{m^2(\theta) + n^2(\theta)} \\ c_y(\theta) &= -\frac{n(\theta)p(\theta) - m(\theta)q(\theta)}{m^2(\theta) + n^2(\theta)} \\ r(\theta) &= \frac{1}{\sqrt{m^2(\theta) + n^2(\theta)}} \end{aligned} \tag{5.25}$$

As long as the model uncertainty $U_e(z)$ lies inside the disk centered at $(c_x(\theta), c_y(\theta))$ with a radius of $r(\theta)$, the general ILC updating law will be monotonic convergent. Note that the radius of the disk is only affected by the design of the learning gain $\mathcal{L}(z)$ while the center of this disk is related both to the learning gain and Q-filter $\mathcal{Q}(z)$.

5.2.2.2 Relationship Between Robustness, Convergence Speed and Steady State Error

In this section, the relationship between robustness, convergence speed and steady state error is investigated. First, the definitions of these three performance indexes are introduced.

The definitions of the robustness and convergence speed remain unchanged:

$$\begin{aligned} \mathrm{RB}(\theta) &\triangleq |r(\theta)| = \frac{1}{\sqrt{m^2(\theta) + n^2(\theta)}} \in (0, \infty) \\ \mathrm{CS}(\theta) &\triangleq 1 - \mathrm{CR}(\theta) \\ &= 1 - \left| \mathcal{Q}\left(e^{j\theta}\right) - G_o\left(e^{j\theta}\right) \mathcal{L}\left(e^{j\theta}\right) \right| \in (0, 1] \end{aligned} \tag{5.26}$$

The steady state error $\mathrm{SSE}(\theta)$ is defined as following:

$$\begin{aligned}\mathrm{SSE}(\theta) &\triangleq \left|\frac{u_d\left(e^{j\theta}\right)-u_\infty\left(e^{j\theta}\right)}{u_d\left(e^{j\theta}\right)}\right| \\ &= \left|\frac{1-\mathcal{Q}\left(e^{j\theta}\right)}{1-\mathcal{Q}\left(e^{j\theta}\right)+G_o\left(e^{j\theta}\right)\mathcal{L}\left(e^{j\theta}\right)}\right| \in [0,1]\end{aligned} \tag{5.27}$$

where $u_d(z)$ denotes the ideal control input that achieves perfect tracking. $\mathrm{SSE}(\theta)=0$ means the control input converges to the ideal one at this frequency, while $\mathrm{SSE}(\theta)=1$ means the input signal convergences to zero. Also note that in Eq. (5.27) when $\mathcal{Q}\left(e^{j\theta}\right)=1$, $\mathrm{SSE}(\theta)=0$, which is consistent with the fact that there will be no steady state error if the Q-filter is not used. The relationship between robustness, convergence speed and steady state error at each frequency is presented in the following Lemma:

Lemma V.2. *For a monotonic convergent ILC updating law Eq. (5.12), its robustness, converge speed and steady state error satisfy the following relationship:*

$$\frac{1}{\mathrm{RB}\left(\theta\right)\mathrm{CS}\left(\theta\right)}+\mathrm{SSE}\left(\theta\right)\geq 1, \quad \forall\theta\in[0,2\pi] \tag{5.28}$$

Proof. See Appendix A for the proof. □

Note that for NO-ILC, the trade-off between robustness, convergence speed and steady state error at each frequency is characterized by Eq. (5.8). Comparing Eq. (5.28) to Eq. (5.8) naturally leads to the conclusion that NO-ILC optimally balances the trade-off between robustness, convergence speed and steady state error at each frequency. As graphically illustrated in Fig. 5.2, the surface represents the Pareto surface of NO-ILC and the performance index of general LTI ILC updating laws lies under that surface. This demonstrates the optimality of NO-ILC in terms of handling the three performance indexes of NO-ILC at each frequency.

Note that the performance index of LTI ILC updating laws other than NO-ILC still can lie on the Pareto curve/surface as shown in Fig. 5.6 and Fig. 5.2 for some frequencies. The optimality of NO-ILC is that it guarantees the performance index lies on the Pareto curve/surface over all the frequencies.

5.3 Conclusion

In this chapter, first, an analytical expression is derived to characterize the fundamental trade-off of NO-ILC between robustness, convergence speed and steady state error. This equation can be leveraged to perform NO-ILC design considering the fundamental trade-off explicitly and quantitatively. Thus, NO-ILC can be designed according to different requirements, i.e., robustness, convergence speed and steady state error, at different frequencies. This shows that the frequency dependent weighting matrices design methodology discussed in Section 4.2 appears to be more powerful than the diagonal weighting matrices design introduced in Section 4.1.

In the second part of this chapter, through a frequency domain analysis approach, the allowable model uncertainty of general LTI ILC updating laws has been both mathematically characterized and illustrated on the Nyquist plot, which helps the RMC design if some knowledge of uncertainty range is given. In addition, the relationship between robustness, convergence speed and steady state error for general LTI ILC updating laws is characterized at each frequency, which in turn demonstrates the optimality of NO-ILC as the Pareto front as discussed in the first part of this chapter.

CHAPTER VI

Optimization Formulation towards NO-ILC Design

Chapter IV discusses the RMC analysis/design methodologies and Chapter VI analytically lays out the fundamental trade-off of NO-ILC between robustness, convergence speed and steady state error. Ideally, when designing NO-ILC, a robust design with fast convergence and small steady state error is desired.

However, the design guidelines in Section 4.2.2 only provide general rules and the design of the weighting matrices Q, R and S is still subject to manual tuning at each frequency, which is ad-hoc and time consuming. So far, there is no design method that explicitly considers the trade-off between robustness, convergence speed, and steady state error and at the same time optimally balances that trade-off. This chapter aims to fill this gap.

In order to fill the above identified gap, this section formulates the design of the NO-ILC weighting matrices as an optimization problem to eliminate the manual tuning process and avoid an unnecessarily conservative design. Specifically, this section develops two optimization formulations to systematically design the weighting matrices for NO-ILC, with one focusing on optimizing the nominal performance and the other focusing on optimizing performance against all possible uncertainties.

6.1 Design for Optimal Nominal Performance

Even though the graphical criterion for RMC has been derived and the fundamental trade-off at each frequency has been laid out for NO-ILC in the previous chapters, the filters $W_1(z)$, $W_2(z)$ and $W_3(z)$ still have to be designed manually to satisfy the corresponding requirement at each frequency. The design guidelines are summarized in Section 4.2.2. A systematic design approach, however, has not been addressed yet. In this section, an optimization-based design methodology is proposed for a systematic NO-ILC design for the purpose of ensuring RMC and at the same time also taking the fundamental trade-off into account explicitly.

6.1.1 Problem Setup

Once the uncertainty has been formulated as described in Chapter III, the goal is to design a NO-ILC that has RMC against all the possible modeling errors in the uncertainty region while maximizing the convergence speed and minimizing the steady state error. This needs to be done for all frequencies.

The graphical interpretation for RMC is to guarantee that the uncertainty region on the Nyquist plot lies inside the RMC disk as illustrated in Fig. 4.18. Thus, at each frequency θ, the radius $r(\theta)$ and center $c_x(\theta)$ need to be appropriately chosen, so that all edges of the uncertainty region lie inside the RMC disk.

Besides the robustness concern, the convergence speed and steady state error are related to the radius and center of the disk as discussed in the rest of this section. Note that the expressions for convergence speed and steady state error for nominal performance are given as:

$$\begin{aligned} \mathrm{CS}(\theta) &= \frac{|W_1(e^{j\theta})|^2 |G_o(e^{j\theta})|^2 + |W_3(e^{j\theta})|^2}{|W_1(e^{j\theta})|^2 |G_o(e^{j\theta})|^2 + |W_2(e^{j\theta})|^2 + |W_3(e^{j\theta})|^2} \\ \mathrm{SSE}(\theta) &= \frac{|W_3(e^{j\theta})|^2}{|W_1(e^{j\theta})|^2 |G_o(e^{j\theta})|^2 + |W_3(e^{j\theta})|^2} \end{aligned} \tag{6.1}$$

which indicates that, for given $W_1\left(e^{j\theta}\right)$, maximizing the convergence speed is the same as minimizing the value of $\left|W_2\left(e^{j\theta}\right)\right|$ and that minimizing the steady state tracking error is the same as minimizing the value of $\left|W_3\left(e^{j\theta}\right)\right|$. Note that minimizing the value of $\left|W_2\left(e^{j\theta}\right)\right|$ is equivalent to minimizing the radius of the RMC disk and the radius is no smaller than one according to Eq. (4.25). Also, note the following relationship:

$$r\left(\theta\right) - c_x\left(\theta\right) = \frac{|W_3\left(e^{j\theta}\right)|^2}{|W_1\left(e^{j\theta}\right)|^2 |G_o\left(e^{j\theta}\right)|^2} \tag{6.2}$$

which indicates that minimizing the steady state tracking error is equivalent to minimizing the distance from the leftmost point on the RMC disk to the origin.

Thus, the original design problem is reformulated into a problem of designing the appropriate radius and center of the RMC disk at various frequencies.

6.1.2 Optimization Setup to Design the Filters

In this section, the problem of designing a robust monotonic convergent NO-ILC while maximizing convergence speed and minimizing steady state tracking error is formulated as an optimization problem at a discrete set of points in the frequency domain. Towards this end, after formulating the model uncertainty, the frequency range is discretized with m points $\{\theta_1, \ldots, \theta_m\}$. For each frequency θ_i, the edges of the uncertainty region are meshed with k points $\{(a_1, b_1), \ldots, (a_k, b_k)\}$, where a_j and b_j denote the x and y coordinate of the j^{th} meshed point on the edges of the uncertainty region. A constrained optimization problem is then formulated at each frequency θ_i as described in this section. To simplify the notation, $c_{x,i}$ and r_i are used to denote $c_x\left(\theta_i\right)$ and $r\left(\theta_i\right)$.

6.1.2.1 Constrains

Two constraints are included in the optimization formulation. First, because of the definition of the center and radius, Eq. (4.25), the following constraint holds:

$$r_i \geq c_i \geq 1, \quad \forall i \in [1, m] \tag{6.3}$$

Second, as discussed in the previous section, the edges of the uncertainty region have to lie inside the RMC disk to achieve RMC. Mathematically, this condition is expressed using the constraint

$$(a_j - c_{x,i})^2 + b_j^2 \leq \sigma_i r_i^2, \quad \forall i \in [1, m], \quad j \in [1, k] \tag{6.4}$$

where $\sigma_i \in (0, 1]$ is a safety factor introduced to compensate for the truncation error that stems from the fact that the frequency domain analysis is for an infinite time horizon, while in practice NO-ILC is always implemented in a finite time horizon. Similar ideas can also be found in (*Gorinevsky*, 2002). The truncation error could be small or even could be neglected for sufficiently large N, i.e., when N is significantly larger than the length of the non-zero impulse response of $G_o(z)$, $W_1(z)$, $W_2(z)$ and $W_3(z)$.

6.1.2.2 Cost Function

Besides RMC, faster convergence speed and smaller steady state tracking error are also preferred. As per the discussion in Section 6.1.1, this goal is translated into minimizing the radius while minimizing the distance from the leftmost point on the RMC disk to the origin. Therefore, the following cost function is constructed:

$$J_i = \alpha_i \|r_i - c_{x,i}\|_2^2 + \|r_i\|_2^2, \quad \forall i \in [1, m] \tag{6.5}$$

where $\alpha_i \geq 0$ is a tunable weighting factor. If α_i is larger, the steady state error is penalized more.

6.1.2.3 Solution Strategy

The *fmincon* command in Matlab is used in this thesis to solve the optimization problem. At each frequency θ_i, the radius r_i and center $c_{x,i}$ of the RMC disk is optimized. Once the value of $\left|W_1\left(e^{j\theta_i}\right)\right|$ is determined (in this work it is chosen as one), the values of $\left|W_2\left(e^{j\theta_i}\right)\right|$ and $\left|W_3\left(e^{j\theta_i}\right)\right|$ are solved using r_i, $c_{x,i}$ and $\left|G_o\left(e^{j\theta}\right)\right|$ according to Eq. (4.25).

6.1.3 Least Squares Setup to Obtain the Weighting Matrices

After the optimization problem is solved, $\left|W_1\left(e^{j\theta_i}\right)\right|$, $\left|W_2\left(e^{j\theta_i}\right)\right|$ and $\left|W_3\left(e^{j\theta_i}\right)\right|$ are obtained for $i \in [1, m]$. Recall, however, that the ultimate goal is to obtain the weighting matrices Q, R and S. This section describes how the weighting matrices can be obtained from $\left|W_1\left(e^{j\theta_i}\right)\right|$, $\left|W_2\left(e^{j\theta_i}\right)\right|$ and $\left|W_3\left(e^{j\theta_i}\right)\right|$ using a least squares formulation.

Note that the weighting matrices Q, R and S are lifted representations of the zero phase filters $Q(z) = W_1(z^{-1})W_1(z)$, $R(z) = W_2(z^{-1})W_2(z)$ and $S(z) = W_3(z^{-1})W_3(z)$. Also note that $\left|Q\left(e^{j\theta}\right)\right| = \left|W_1\left(e^{j\theta}\right)\right|^2$, $\left|R\left(e^{j\theta}\right)\right| = \left|W_2\left(e^{j\theta}\right)\right|^2$ and $\left|S\left(e^{j\theta}\right)\right| = \left|W_3\left(e^{j\theta}\right)\right|^2$. The matrix Q and the zero-phase filter $Q(z)$ have the following structure:

$$Q = \begin{bmatrix} q_0 & q_1 & \cdots & q_{N-1} \\ q_1 & q_0 & q_1 & \vdots \\ \vdots & q_1 & \ddots & q_1 \\ q_{N-1} & \cdots & q_1 & q_0 \end{bmatrix} \in \mathbb{R}^N \tag{6.6}$$

$$Q(z) = \cdots + q_2 z^2 + q_1 z + q_0 + q_1 z^{-1} + q_2 z^{-2} + \cdots$$

Similar structures hold for R, $R(z)$ and S, $S(z)$, as well.

For a stable filter, q_i will be zero for some sufficiently large i, since the impulse response of a stable system will decay to zero. Thus, for sufficiently large N , the following relationship is true:

$$Q\left(e^{j\theta}\right) = \left|W_1\left(e^{j\theta}\right)\right|^2 \approx \sum_{i=-(N-1)}^{N-1} q_{|i|} e^{ji\theta} = \sum_{i=1}^{N-1} 2q_i \cos i\theta + q_0 \tag{6.7}$$

For practical concerns, when N is significantly larger than the time steps that needed for the impulse response to decay to zero, the above equation can be a good approximation. Thus, the following least squares problem is formulated:

$$\begin{bmatrix} \left|W_1\left(e^{j\theta_1}\right)\right|^2 \\ \left|W_1\left(e^{j\theta_2}\right)\right|^2 \\ \vdots \\ \left|W_1\left(e^{j\theta_m}\right)\right|^2 \end{bmatrix} = \begin{bmatrix} 1 & 2\cos\theta_1 & \cdots & 2\cos\left(N-1\right)\theta_1 \\ 1 & 2\cos\theta_2 & \cdots & 2\cos\left(N-1\right)\theta_2 \\ \vdots & \vdots & \vdots & \vdots \\ 1 & 2\cos\theta_m & \cdots & 2\cos\left(N-1\right)\theta_m \end{bmatrix} \begin{bmatrix} q_0 \\ q_1 \\ \vdots \\ q_{N-1} \end{bmatrix} \tag{6.8}$$

To have a unique solution to this least squares problem, using $m \geq N$ is preferred. Once the solution is obtained, the construction of the weighting matrix Q is complete. R and S matrices are obtained using the same method.

This completes the description of the design methodology for optimal nominal performance. This design methodology guarantees RMC against possible uncertainties while maximizing the convergence speed and minimizing the steady steady state error for optimal nominal performance. However, note that a better nominal performance does not necessarily correspond to a better performance when uncertainty is present. Therefore, the following section presents an alternative design methodology that guarantees RMC while maximizing the convergence speed and minimizing the steady steady state error for optimal performance under the presence of uncertainties.

6.2 Design for Optimal Performance Under Uncertainties

An optimal design for the nominal plant does not necessarily guarantee a good performance for the real plant. In this section, two examples are used to demonstrate this fact first. Then, the optimization problem formulation of the previous section is modified to create a design method for optimal performance against uncertainties while ensuring RMC.

6.2.1 Disadvantage of the Nominal Performance Based Design

The two examples given in this section illustrate the fact that increasing R does not necessarily slow down the convergence speed and increasing S does not necessarily increase the steady state error against a modeling error. All the transfer functions are reported in continuous domain for ease of presentation, but are discretized with a sampling time of $T_s = 0.01$s in the implementation. In both examples, the tracking reference is a sinusoid with a frequency of 30.1 rad/s.

Example 1: Consider the nominal plant and the modeling error

$$G_o(s) = \frac{s+1}{s+2}; \quad U_e(s) = 1.8\frac{s+11}{s+10} \tag{6.9}$$

Consider two weighting matrix designs for NO-ILC. Design 1 is with $Q_1 = I$, $R_1 = S_1 = 0$, and Design 2 is with $Q_2 = R_2 = I$, $S_2 = 0$, where I represents the identity matrix. Both designs in this case guarantee RMC against the modeling error $U_e(s)$. Considering the nominal performance for both designs, Design 1 has a faster convergence speed, since $R_1 < R_2$. However, Design 1 converges much slower in the presence of the modeling error as shown in Fig. 6.1(a).

Example 2: Consider the nominal plant and modeling error

$$G_o(s) = \frac{s+1}{s+2}; \quad U_e(s) = -0.2 \tag{6.10}$$

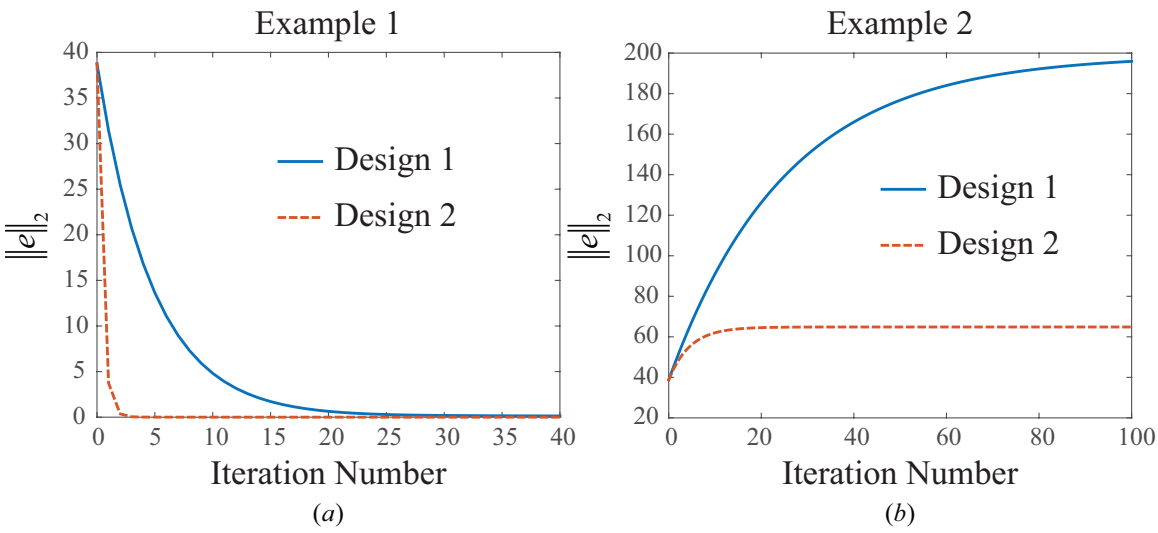

Figure 6.1: Two examples illustrating that better nominal performance does not necessarily mean better performance against model uncertainty

Consider two weighting matrix designs for NO-ILC. Design 1 is with $Q_1 = I$, $R_1 = 0$, $S_1 = 0.25I$, and Design 2 is with $Q_2 = I$, $R_2 = 0$, $S_2 = 0.5I$. Both designs in this case guarantee RMC against the modeling error $U_e(s)$. Considering the nominal performance for both designs, Design 1 has a smaller steady state error, since $S_1 < S_2$. However, Design 1 leads to a much larger steady state error when the modeling error is present as shown in Fig. 6.1(b).

The above two examples show that improving the nominal performance of NO-ILC does not necessarily lead to a better performance against model uncertainty. Therefore, the performance of the design that results from the optimization formulation developed in the previous section may have limitations. An alternative formulation is presented in this section that aims to maximize the performance of NO-ILC against model uncertainties.

6.2.2 Design Against Uncertainties

To ensure the robustness of NO-ILC against model uncertainty, the gray uncertainty region on Nyquist plot needs to lie inside the RMC disk over all frequencies.

This goal is the same as the one in the nominal performance based design. To maximize the convergence speed and minimize the steady state error against all possible model uncertainty, however, the specific goal of the optimization is modified. In particular, the following two terms need to be minimized at each frequency θ_i:

$$\mathrm{CR}_u := \left| \mathcal{Q}\left(e^{j\theta_i}\right) - \mathcal{L}\left(e^{j\theta_i}\right) G\left(e^{j\theta_i}\right) \right|^2 \tag{6.11}$$

$$\mathrm{SSE}_u := \left| \frac{1 - \mathcal{Q}\left(e^{j\theta_i}\right)}{1 - \mathcal{Q}\left(e^{j\theta_i}\right) + \mathcal{L}\left(e^{j\theta_i}\right) G\left(e^{j\theta_i}\right)} \right|^2 \tag{6.12}$$

where CR_u is the convergence rate and SSE_u is steady state error against the model uncertainty. Recall that $G\left(e^{j\theta_i}\right) = G_o\left(e^{j\theta_i}\right) U_e\left(e^{j\theta_i}\right)$. Even though $U_e\left(e^{j\theta_i}\right)$ is unknown, its range is known as the gray region illustrated in Fig. 4.18 at frequency θ_i. In this alternative formulation, this gray region is meshed uniformly with p points $\{U_{e,1}\left(e^{j\theta_i}\right), \cdots, U_{e,p}\left(e^{j\theta_i}\right)\}$ in addition to meshing the edges as in the previous formulation. Let

$$x_{ii} = \mathrm{Re}\{U_{e,ii}(e^{j\theta_i})\}, \quad y_{ii} = \mathrm{Im}\{U_{e,ii}(e^{j\theta_i})\}, \quad ii \in [1, p] \tag{6.13}$$

where $\mathrm{Re}\{\cdot\}$ and $\mathrm{Im}\{\cdot\}$ denote the real part and imaginary part of a complex number. For simplicity of notation, $\mathcal{Q}_i$, $\mathcal{L}_i$ and $G_{o,i}$ are used to denote $\mathcal{Q}\left(e^{j\theta_i}\right)$, $\mathcal{L}\left(e^{j\theta_i}\right)$ and $G_o\left(e^{j\theta_i}\right)$, respectively. Assuming $U_e\left(e^{j\theta_i}\right)$ has equal chance to lie anywhere inside the uncertainty region, minimizing Eq. (6.11) and Eq. (6.12) is the same as minimizing the following expressions:

$$\sum_{ii=1}^{p} \left(\mathcal{Q}_i - \mathcal{L}_i G_{o,i}\left(x_{ii} + jy_{ii}\right)\right)\left(\mathcal{Q}_i - \mathcal{L}_i G_{o,i}\left(x_{ii} - jy_{ii}\right)\right) \tag{6.14}$$

$$\sum_{ii=1}^{p} \frac{1 - \mathcal{Q}_i}{1 - \mathcal{Q}_i + \mathcal{L}_i G_{o,i}\left(x_{ii} + jy_{ii}\right)} \times \frac{1 - \mathcal{Q}_i}{1 - \mathcal{Q}_i + \mathcal{L}_i G_{o,i}\left(x_{ii} - jy_{ii}\right)} \tag{6.15}$$

Note the following relationship between r_i, $c_{x,i}$, $\mathcal{Q}_i$ and $\mathcal{L}_i G_{o,i}$:

$$\mathcal{Q}_i = \frac{c_{x,i}}{r_i}; \quad \mathcal{L}_i G_{o,i} = \frac{1}{r_i} \tag{6.16}$$

Plugging the above equations into Eq. (6.14) and (6.15) leads to the cost function for the optimal design against uncertainties at each frequency θ_i:

$$J_i = \sum_{ii=1}^{p} \frac{\left(x_{ii} - c_{x,i}\right)^2 + {y_{ii}}^2}{{r_i}^2} + \alpha_i \sum_{ii=1}^{p} \frac{\left(r_i - c_{x,i}\right)^2}{\left(x_{ii} + r_i - c_{x,i}\right)^2 + {y_{ii}}^2} \tag{6.17}$$

where $\alpha_i \geq 0$ is a tunable weighting factor.

The constraint formulations and the solution strategy are the same as the previous formulation. Hence, this design approach differs from the previous one in only two ways: 1) the uncertainty region is meshed in addition to the edges; and 2) a different cost function is used in the optimization.

If there is some prior knowledge about where $U_e\left(e^{j\theta_i}\right)$ is more likely to lie in the uncertainty region, weighting factors can be introduced in Eq. (6.14) and Eq. (6.15) to incorporate that knowledge.

6.3 Summary of Design Procedure

Step 1: Formulate the model uncertainty, pick m frequencies $\{\theta_1, \cdots, \theta_m\}$ with $m \geq N$. For each frequency θ_i, mesh the edges of the uncertainty region with k points $\{(a_1, b_1), \cdots, (a_k, b_k)\}$. Additionally, if designing for an optimal performance against uncertainties, mesh the uncertainty region with p points $\{(x_1, y_1), \cdots, (x_p, y_p)\}$ at each frequency θ_i, as well.

Step 2: For each frequency θ_i, solve the constrained optimization with the cost function of Eq. (6.5) for optimal nominal performance or Eq. (6.17) for optimal performance against uncertainties and constrains of Eq. (6.4), (6.3). Based on the

obtained radius r_i and center $c_{x,i}$ of the RMC disk at each frequency, determine $\left|W_1\left(e^{j\theta_i}\right)\right|$, $\left|W_2\left(e^{j\theta_i}\right)\right|$ and $\left|W_3\left(e^{j\theta_i}\right)\right|$.

Step 3: Solve the least squares problem as shown in Eq. (6.8), to obtain the weighting matrices Q, R and S.

6.4 Simulation Examples

Two simulation examples are used to demonstrate the effectiveness of the developed design methodologies. The first example compares the performances of the two design methodologies presented above. The second example focuses on the design for optimal performance under uncertainties and shows how the weighing term α affects the trade-off between convergence speed and steady state error. All the transfer functions are reported in continuous domain, but are discretized in the implementation with a sampling time of $T_s = 0.01$s. The number of total running steps is $N = 3000$.

6.4.1 Example 1

Consider the following nominal plant and modeling error:

$$G_o(s) = \frac{s+20}{s+5}; \quad U_e(s) = \frac{(0.19s+1)(0.033s+1)}{(0.08s+1)(0.05s+1)} \tag{6.18}$$

Let the upper and lower bounds on the Bode plot be

$$U_{e,\max}(s) = 3\frac{s+5}{s+10}; \quad U_{e,\min}(s) = 0.3\frac{s+20}{s+10} \tag{6.19}$$

The Bode plot of the real system $G(s) = G_o(s)U_e(s)$ is shown as the dotted red curve in Fig. 6.2. The nominal plant $G_o(s)$ is shown as the solid green curve. The upper and lower bounds of the uncertainty region are indicated as the dashed blue lines in Fig. 6.2 and the gray region indicates the uncertainty region.

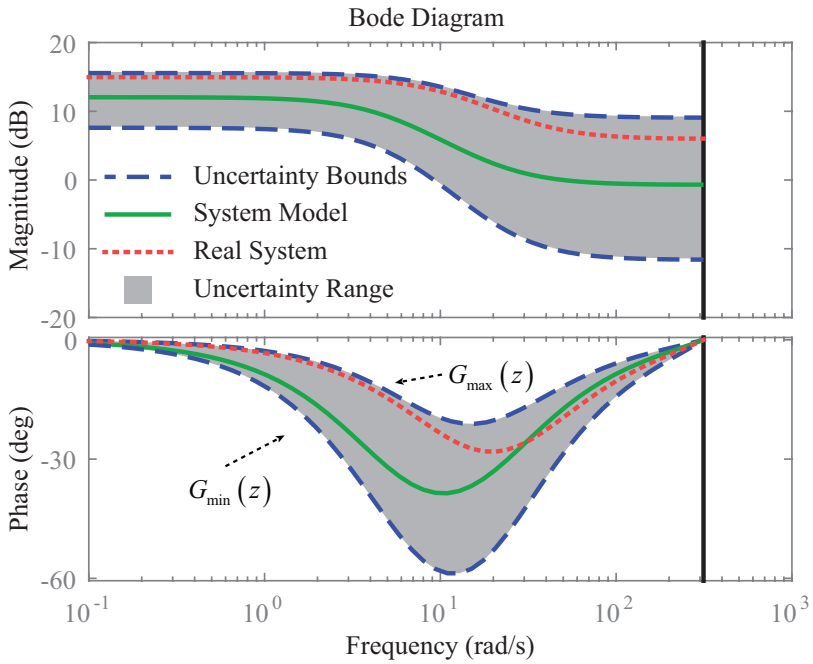

Figure 6.2: Bode plot of the real system, nominal model and uncertainty range

Design for Optimal Nominal Performance (Design 1): The frequency range of interest in this case is uniformly meshed into $m = 3000$ points $\{\theta_1, \cdots, \theta_m\}$ with $\theta_1 = 0$ and $\theta_m = \pi/T_s$ rad/s. For each frequency θ_i, the edges of the uncertainty region are meshed with $k = 100$ points, with 25 points on each edge. For example, the meshed points are shown in Fig. 6.3a at the frequency of 15 rad/s. For the optimization setup, the safety factor σ_i is set to 0.9 and the weighting factor α_i is set to 100 for all $i \in [1, m]$. At each frequency θ_i, the radius r_i and the center $c_{x,i}$ are optimized. As an example, the RMC disks obtained at 15 rad/s and 73 rad/s are shown as the green circles in Fig. 6.4a and Fig. 6.4b.

Design for Optimal Performance Under Uncertainties (Design 2): In this example, the number of the meshing points in the uncertainty region is picked as $p = 100$. As an example, the meshing of the uncertainty region at 15 rad/s is shown in Fig. 6.3. All the other settings remain the same as in Design 1. As an example, the RMC disks obtained at 15 rad/s and 73 rad/s are shown as the cyan circles in Fig. 6.4a and Fig. 6.4b.

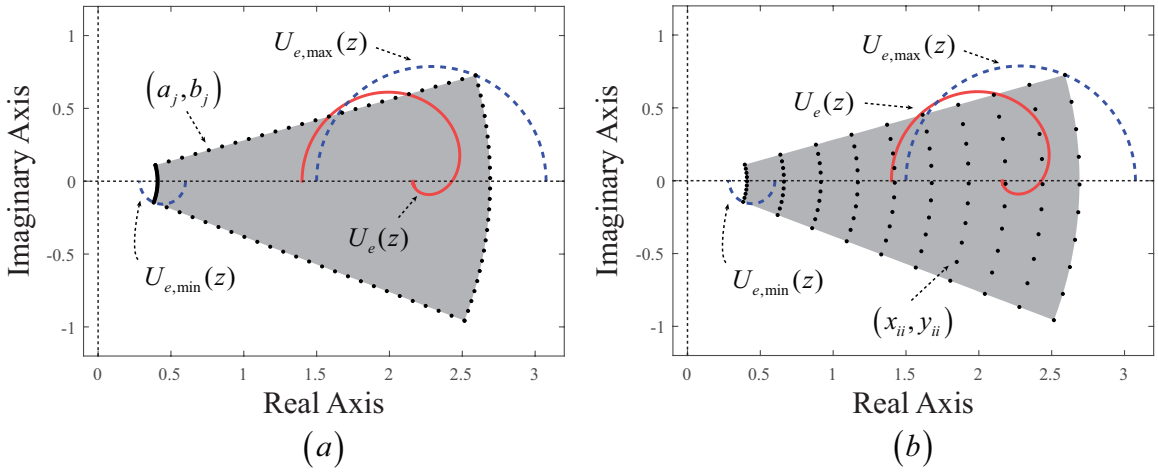

Figure 6.3: Mesh points of the (a) edges of uncertainty region and (b) uncertainty region at 15 rad/s

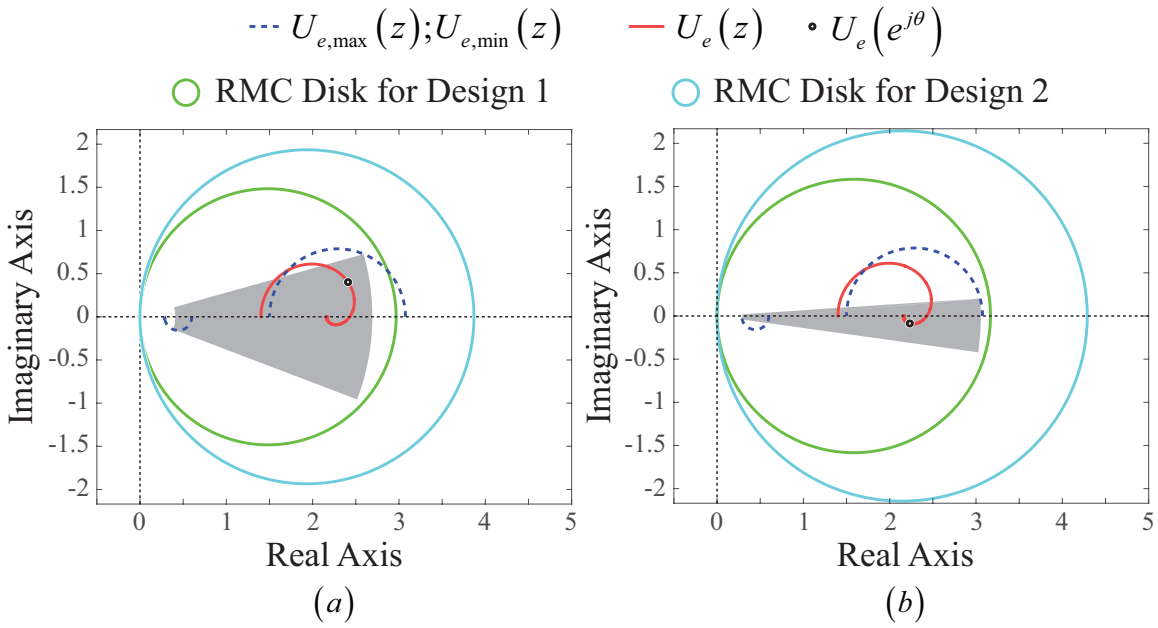

Figure 6.4: RMC disks for Design 1 and Design 2 at (a) 15 rad/s and (b) 73.2 rad/s

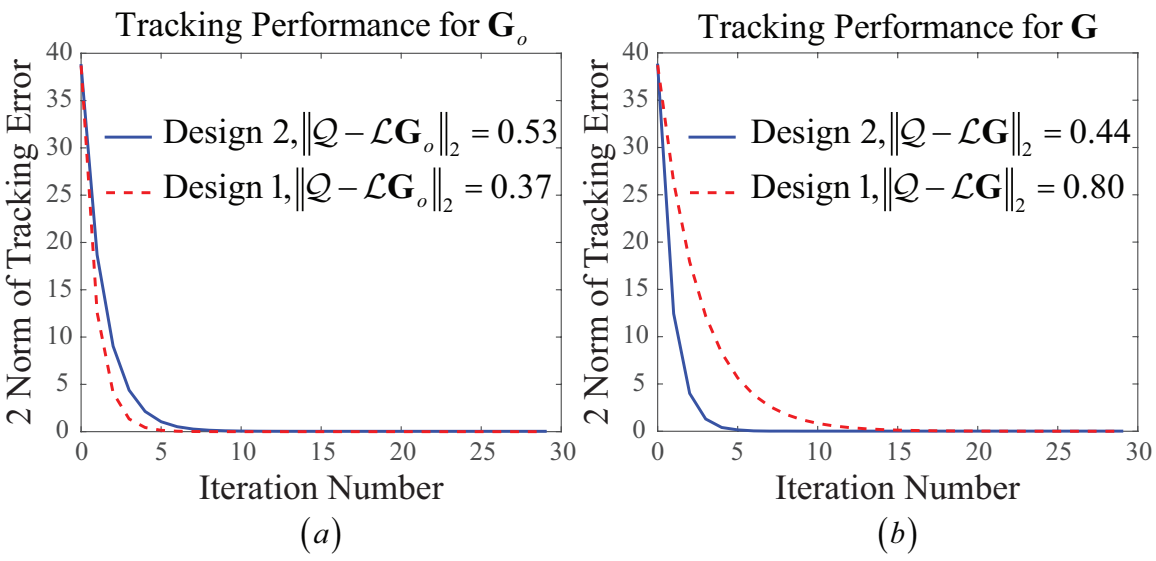

Figure 6.5: Tracking performance against (a) nominal plant and (b) real plant

The tracking reference is a sinusoid of 15 rad/s. Fig. 6.5a shows the tracking results for the nominal plant G_o, whereas Fig. 6.5b shows the tracking results for the real plant $\mathbf{G}_o$. For both cases, since the penalty for steady state error in the cost function is set to a large number ($\alpha_i = 100$) and since the model uncertainty is positive real (the phase of the uncertainty region never exceeds $[0, -\pi/2]$ in Fig. 6.2), the RMC disks generated by both design methods never go to the left half plane. This corresponds to a design with no Q-filter. As a result, zero steady state tracking error is achieved with both design formulations as shown in Fig. 6.5, and the difference between the two formulations manifests itself in the convergence speed.

With nominal performance being its focus, Design 1 always seeks the smallest disk that encloses the uncertainty region. Thus, the RMC disks obtained by Design 1 are smaller than those obtained by Design 2; see Fig. 6.4 for examples at two frequencies. As a result, Design 1 converges faster than Design 2 for the nominal plant as seen in Fig. 6.5a. However, better nominal performance does not necessarily mean better performance in the presence of uncertainties. Fig. 6.5b shows the tracking results of the two design methods for the real plant. Both methods ensure RMC as expected.

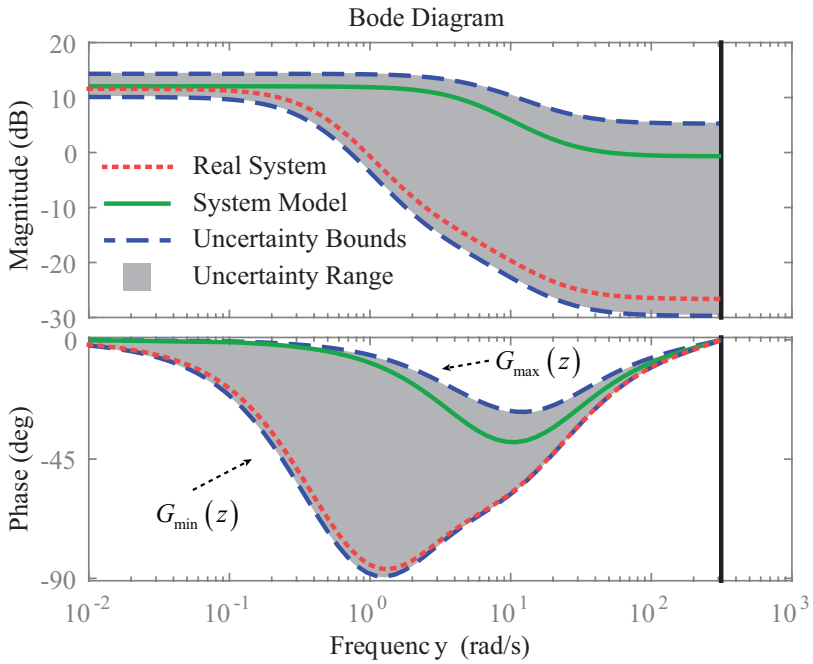

Figure 6.6: Bode plot of the real system, nominal model and uncertainty range

However, Design 2 converges faster than Design 1, which is consistent with the fact that Design 2 specifically targets optimal performance against uncertainties.

6.4.2 Example 2

In this example, the functionality of the weighting term α is illustrated. Consider the following nominal plant and modeling error:

$$G_o(s) = \frac{s+20}{s+5}; \quad U_e(s) = 0.95\frac{(0.45s+1)(0.45s+1)}{(1.5s+1)(2.5s+1)} \tag{6.20}$$

Let the upper and lower bounds on the Bode plot be

$$U_{e,\max}(s) = \frac{1.95s+13}{s+10}; \quad U_{e,\min}(s) = \frac{(3.6s+8)(4.5s+10)}{(15s+10)(25s+10)} \tag{6.21}$$

The Bode plot of the real system, system model and uncertainty region are shown in Fig. 6.6.

We consider the design for optimal performance under uncertainties (Design 2).

Similar to the previous example, the frequency range of interest is uniformly meshed into $m = 3000$ points $\{\theta_1, \ldots, \theta_2\}$ with $\theta_1 = 0$ and $\theta_m = \pi/T_s$ rad/s. For each frequency θ_i, the edges of the uncertainty region are meshed with $k = 100$ points, with 25 points on each edge, and the number of the meshing points in the uncertainty region is picked as $p = 100$. For the optimization setup, the safety factor σ_i i is set to 0.985 and the weighting factor α_i is picked from a list of $\{2, 4, 8, 16, 32\}$ for all $i \in [1, m]$.

In this case, the model uncertainty is still positive real, since the phase difference never exceeds $[0, -\pi/2]$ as shown in Fig. 6.6. However, the uncertainty region does get very close to the imaginary axis at the frequency around 1.5 rad/s; as an example, see the gray uncertainty region in Fig. 6.7 at 1.47 rad/s. To enclose this uncertainty region, the RMC disk can be picked either with a smaller radius but with larger area in the negative half plane (e.g., see the RMC disk for $\alpha = 2$ in Fig. 6.7), or with a larger radius but smaller area in the negative half plane (e.g., see the RMC disk for $\alpha = 32$ in Fig. 6.7). The RMC disks generated by different α values at this frequency are shown in Fig. 6.7 with a zoom-in view around the origin showing how much the RMC disk goes into the negative half plane for different α values.

The tracking reference is a sinusoid of 1.5 rad/s. For different values of α, the tracking results are shown in Fig. 6.8. All designs yield RMC, since the tracking differences $\mathbf{e}_i - \mathbf{e}_\infty$ are monotonic convergent as shown in Fig. 6.8b. As expected, larger α value corresponds to more penalization on the steady state error and therefore leads to smaller steady state error as shown in Fig. 6.8a, however, at the cost of slower convergence speed as shown in Fig. 6.8b.

6.5 Conclusion

This chapter contributes in two aspects to the NO-ILC literature. First, an optimization approach is developed for designing the NO-ILC weighting matrices that

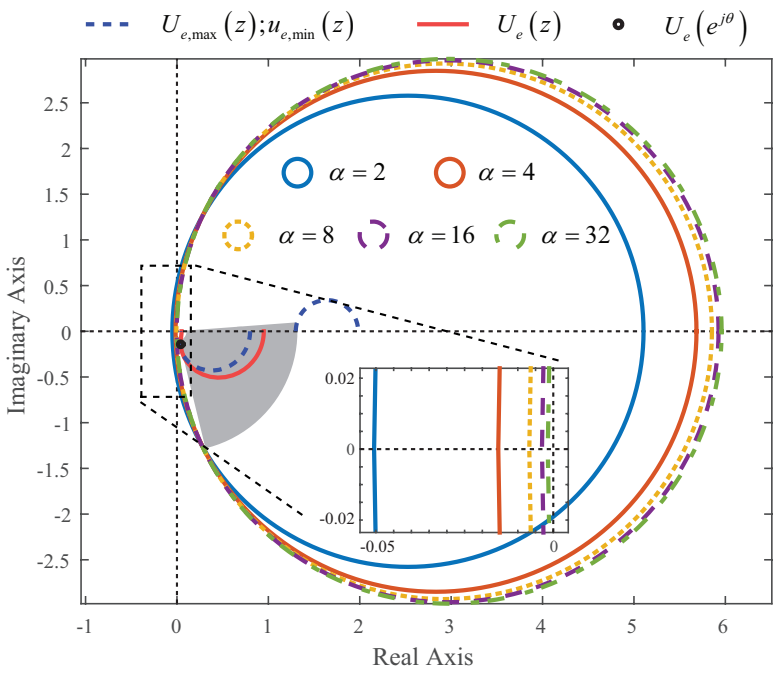

Figure 6.7: RMC disks for different α values at 1.47 rad/s

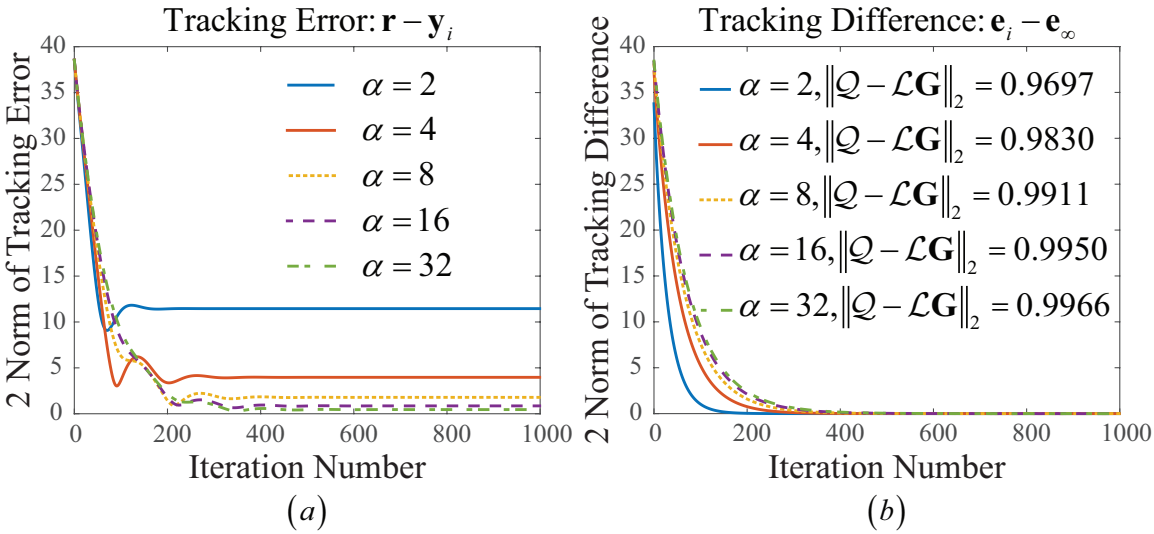

Figure 6.8: Design for optimal performance under uncertainties (a) tracking error and (b) tracking difference

eliminates the manual tuning process for filter designs and systematically achieves an optimal balance between robustness, convergence speed and steady state error. Second, two different optimization formulations are constructed. Both formulations aim for RMC, but the first one seeks to optimize the nominal performance, whereas the second one seeks to optimize the performance against uncertainties. The proposed design approach is shown through two demonstrative examples to be an effective, systematic procedure for designing NO-ILC.

CHAPTER VII

Concluding Remarks and Future Work

This thesis aims to answer the question of: Can we develop analysis and design tools that better characterize the allowable model uncertainties and better reveal the frequency domain properties of NO-ILC?

The objective of this research is to provide fundamental analysis tools for the frequency domain properties of Norm-Optimal Iterative Learning Control (NO-ILC), which leads to novel design methodologies for NO-ILC to compensate the trade-off between robustness, convergence speed and steady state error at different frequencies. The work presented in Chapters III to VI results in the following contributions to the NO-ILC literature:

- This work presents a new model uncertainty formulation for NO-ILC. Unlike the conventional uncertainty formulation, which leads to the conclusion that R does not affect the robustness (*Donkers et al.*, 2008; *Gorinevsky*, 2002), the new formulation used in this work yields that the robustness is affected by both R and S, but in different manners. This is partially based on the following publications:

  Ge, X., J. L. Stein, and T. Ersal (2016a), A frequency domain approach for designing filters for norm-optimal iterative learning control and its fundamental tradeoff between robustness, convergence speed

and steady state error, American Control Conference, pp. 384–391
Ge, X., J. L. Stein, and T. Ersal (2017a), Frequency domain analysis of robust monotonic convergence of norm-optimal iterative learning control, *IEEE Transactions on Control System Technology*, *accepted*

- Based on the above uncertainty formulation, this work both mathematically and graphically presents how the weighting terms in the cost function affect the robustness of NO-ILC. This leads to several new graphical design methodologies for the weighting matrices to achieve the RMC requirement. This is partially based on the following publications:

  Ge, X., J. L. Stein, and T. Ersal (2016a), A frequency domain approach for designing filters for norm-optimal iterative learning control and its fundamental tradeoff between robustness, convergence speed and steady state error, American Control Conference, pp. 384–391
  Ge, X., J. L. Stein, and T. Ersal (2017b), A frequency-dependent filter design approach for norm-optimal iterative learning control and its fundamental trade-off between robustness, convergence speed and steady state error, *ASME Journal of Dynamic Systems, Measurement and Control*, *submitted*

- An analytical equation is derived to quantitatively characterize the fundamental trade-off between robustness, convergence speed and steady state error of NO-ILC in frequency domain. This equation can be helpful during the design process to satisfy a desired robustness requirement while ensuring fast convergence and small steady state error at different frequencies. This equation also reveals the optimality of NO-ILC among general ILC updating laws in the scope of LTI

systems. And this is partially based on the following publications:

Ge, X., J. L. Stein, and T. Ersal (2016a), A frequency domain approach for designing filters for norm-optimal iterative learning control and its fundamental tradeoff between robustness, convergence speed and steady state error, American Control Conference, pp. 384–391

Ge, X., J. L. Stein, and T. Ersal (2017b), A frequency-dependent filter design approach for norm-optimal iterative learning control and its fundamental trade-off between robustness, convergence speed and steady state error, *ASME Journal of Dynamic Systems, Measurement and Control, submitted*

Ge, X., J. L. Stein, and T. Ersal (2017d), Optimality of norm-optimal iterative learning control, *ASME Journal of Dynamic Systems, Measurement and Control, to be submitted*

- Based on the analysis on allowable model uncertainty and fundamental trade-off for NO-ILC, two optimization based formulations are proposed to systematically design the weighting matrices for NO-ILC, which eliminate the manual tuning process and avoid unnecessarily conservative designs. And this is partially based on the following publications:

  Ge, X., J. L. Stein, and T. Ersal (2016b), Optimization based weighting matrices design for norm optimal iterative learning control, Dynamics Systems and Control Conference

  Ge, X., J. L. Stein, and T. Ersal (2017c), Optimization based weighting matrices design for norm optimal iterative learning control, *IEEE Transactions on Control System Technology, to be submitted*

Specifically, Chapter III proposes a novel model uncertainty formulation on Bode Plot and addresses the transformation of this uncertainty between the Bode and Nyquist plots. Then the validity of frequency domain RMC criterion is addressed and the need for new graphical design methodology is motivated. Based on the proposed model uncertainty formulation, Chapter IV presents two novel RMC analysis and design tools for NO-ILC, one with diagonal weighting matrices design and the other one with frequency dependent weighting matrices design. Both analysis methods offer graphical interpretations of the allowable model uncertainty region on the Nyquist plot and lead to novel design guidelines, which are less conservative compared with the traditional NO-ILC design methods. Chapter V develops an analytical equation that characterizes the fundamental trade-off of NO-ILC between robustness, convergence speed and steady state error at each frequency. Furthermore, it shows that NO-ILC is the optimal solution under the scope of general LTI ILC updating laws for LTI systems in terms addressing the trade-off between robustness, convergence speed and steady state error at each frequency. Chapter VI presents two different formulations for the design of NO-ILC weighting matrices as an optimization problem to eliminate the manual tuning process and avoid unnecessary conservative designs.

The developed analysis and design methodologies currently are for SISO systems. One potential interesting future research direction is to extend the current analysis and design tools to MIMO systems. As mentioned, NO-ILC is originally derived using the lifted representation. The current research adopts the transfer function representation to better address the frequency domain properties of NO-ILC. Another interesting potential research direction is to explore whether adopting the state-space representation in NO-ILC analysis/design would further reveal other properties of NO-ILC.

APPENDICES

APPENDIX A

PROOFS FOR PROPOSITIONS AND LEMMAS

Proof of of Proposition IV.1:

Proof. Because $0 < \alpha(\theta) \leq 1$ and $\left|U_e\left(e^{j\theta}\right)\right|^2 \geq 0$, to satisfy the criterion given by Eq. (4.2), $\mathrm{Re}\{U_e\left(e^{j\theta}\right)\}$ needs to be non-negative for all $\theta \in [0, 2\pi]$. If $\mathrm{Re}\{U_e\left(e^{j\theta}\right)\}$ is negative for any $\theta \in [0, 2\pi]$, Criterion (4.2) cannot be satisfied. □

Proof of Proposition IV.2:

Proof. If for λ_0 the NO-ILC is robust monotonic convergent, then $\mathrm{Re}\{U_e\left(e^{j\theta}\right)\} > 0$ for all $\theta \in [0, 2\pi]$ and the following inequality is valid:

$$\mathrm{CR}_0(\theta) = (\alpha_0(\theta))^2\left|U_e\left(e^{j\theta}\right)\right|^2 - 2\alpha_0(\theta)\,\mathrm{Re}\{U_e\left(e^{j\theta}\right)\} < 0 \tag{A.1}$$

where $\mathrm{CR}(\theta)$ stands for convergence ratio. Note that $\mathrm{CR}(\theta) > -1$ and $\mathrm{CR}(\theta) \in (-1, 0)$ for RMC. $\alpha_0(\theta)$ is defined as

$$\alpha_0(\theta) \triangleq \frac{\left|G_o\left(e^{j\theta}\right)\right|^2}{\left|G_o\left(e^{j\theta}\right)\right|^2 + \lambda_0} \tag{A.2}$$

If a $\lambda' > \lambda_0$ is chosen for NO-ILC, the RMC criterion becomes

$$\mathrm{CR}'(\theta) = (\alpha'(\theta))^2 \left|U_e\left(e^{j\theta}\right)\right|^2 - 2\alpha'(\theta)\,\mathrm{Re}\{U_e\left(e^{j\theta}\right)\} < 0 \tag{A.3}$$

where $\alpha'(\theta)$ is defined as

$$\alpha'(\theta) \triangleq \frac{\left|G_o\left(e^{j\theta}\right)\right|^2}{\left|G_o\left(e^{j\theta}\right)\right|^2 + \lambda'} \tag{A.4}$$

Because $\alpha_0(\theta) \in (0, 1]$, from Eq. (A.1) it can be shown that

$$-2\mathrm{Re}\{U_e\left(e^{j\theta}\right)\} < -\alpha_0(\theta)\left|U_e\left(e^{j\theta}\right)\right|^2 \tag{A.5}$$

Substituting Eq. (A.5) into CR′, the following inequality is obtained:

$$\mathrm{CR}'(\theta) < \alpha'(\theta)\left(\alpha'(\theta) - \alpha_0(\theta)\right)\left|U_e\left(e^{j\theta}\right)\right|^2 < 0 \tag{A.6}$$

Therefore, $\mathrm{CR}'(\theta) < 0$ for all $\theta \in [0, 2\pi]$. □

Proof of Lemma IV.3:

Proof. If $U_e\left(e^{\theta}\right)$ lies inside the RMC disk for all $\theta \in [0, 2\pi]$, this means Eq. (4.5) is valid; i.e.

$$a^2\left(x^2(\theta) + y^2(\theta)\right) - 2ax < 0 \tag{A.7}$$

Substituting the definitions of $x(\theta)$ and $y(\theta)$ into the above equation gives Eq. (A.8).

$$\left(\frac{a}{\alpha(\theta)}\right)^2 \left[(\alpha(\theta))^2\left|U_e\left(e^{j\theta}\right)\right|^2 - 2\alpha(\theta)\,\mathrm{Re}\{U_e\left(e^{j\theta}\right)\}\right] + 2a\left[\frac{a}{\alpha(\theta)} - 1\right]\mathrm{Re}\{U_e\left(e^{j\theta}\right)\} < 0, \forall\theta \in [0, 2\pi] \tag{A.8}$$

Note that with $\beta = 0$ the disk lies in the right half plane; thus $\mathrm{Re}\{U_e\left(e^{j\theta}\right)\} \geq 0$. Combing this observation with the fact that $1 > a \geq \alpha(\theta) > 0$, the following is obtained:

$$(\alpha(\theta))^2 \left|U_e\left(e^{j\theta}\right)\right|^2 - 2\alpha(\theta)\,\mathrm{Re}\{U_e\left(e^{j\theta}\right)\} < 0, \forall\theta \in [0, 2\pi] \tag{A.9}$$

The above inequality is exactly the same as the RMC Criterion (4.2). Therefore, the NO-ILC as described by Eq. (2.15) with $\beta = 0$ is robust monotonic convergent against the modeling error $U_e(z)$.

The above analysis shows that Eq. (4.5) is a sufficient condition for Criterion (4.2). In addition, as per the discussion after Eq. (4.5), a larger λ value enlarges the RMC region. Hence, using $\lambda' > \lambda_0$ would enlarge the RMC region. □

Proof of Proposition IV.4:

Proof. If the modeling error $U_e(z)$ can be tolerated with $\lambda = \lambda_0$ and $\beta = 0$, Eq. (4.7) holds with $\alpha(\theta) = \gamma(\theta)$ and can be written as Eq. (A.10).

$$\left[\frac{\alpha(\theta)}{\gamma(\theta)}\right]^2 \left[\gamma^2(\theta)\left|U_e\left(e^{j\theta}\right)\right|^2 - 2\frac{\gamma^2(\theta)}{\alpha(\theta)}\mathrm{Re}\{U_e\left(e^{j\theta}\right)\} + \frac{\gamma^2(\theta)}{\alpha^2(\theta)} - 1\right] + \left[\frac{\alpha(\theta)}{\gamma(\theta)}\right]^2 \left(1 - \frac{\gamma^2(\theta)}{\alpha^2(\theta)}\right) < 0, \forall\theta \in [0, 2\pi] \tag{A.10}$$

When λ is held at the same value and β is increased from 0, according to the definition of $\gamma(\theta)$ and $\alpha(\theta)$, the following always holds: $0 < \gamma(\theta) < \alpha(\theta) < 1$. Substituting these relationships into Eq. (A.10) implies Eq. (4.7), since the second term in Eq. (A.10) is positive. This means this modeling error can also be tolerated with $\lambda = \lambda_0$ and $\beta > 0$. □

Proof of Proposition IV.5:

Proof. If for λ_0 and β_0 the NO-ILC has RMC against $U_e(z)$, Eq. (A.11) holds

$$\mathrm{CR}_0(\theta) \triangleq \gamma_0^2(\theta)\left|U_e\left(e^{j\theta}\right)\right|^2 - 2\frac{\gamma_0^2(\theta)}{\alpha_0(\theta)}\mathrm{Re}\{U_e\left(e^{j\theta}\right)\} + \frac{\gamma_0^2(\theta)}{\alpha_0^2(\theta)} - 1 < 0, \forall\theta \in [0, 2\pi] \tag{A.11}$$

where $\alpha_0(\theta)$ and $\gamma_0(\theta)$ are defined in Eq. (4.3) and Eq. (4.6), respectively. Following the definition of $x(\theta)$ and $y(\theta)$ in Eq. (4.4), after some manipulation, Eq. (A.11) can be re-written into Eq. (A.12). Following the same argument as in **Proposition IV.1**, $x(\theta) - \left(\alpha_0^{-1}(\theta) - \gamma_0^{-1}(\theta)\right)$ needs to be non-negative for all $\theta \in [0, 2\pi]$.

$$\begin{aligned}\mathrm{CR}_0(\theta) = \gamma_0^2(\theta)&\left[\left(x(\theta) - \left(\frac{1}{\alpha_0(\theta)} - \frac{1}{\gamma_0(\theta)}\right)\right)^2 + y^2(\theta)\right] \\ &- 2\gamma_0(\theta)\left[x(\theta) - \left(\frac{1}{\alpha_0(\theta)} - \frac{1}{\gamma_0(\theta)}\right)\right] < 0, \forall\theta \in [0, 2\pi]\end{aligned} \tag{A.12}$$

If λ_0 is increased to λ' but β_0 retains its value, the convergence ratio, $\mathrm{CR}'(\theta)$, becomes Eq. (A.13):

$$\begin{aligned}\mathrm{CR}'(\theta) = (\gamma'(\theta))^2&\left[\left(x(\theta) - \left(\frac{1}{\alpha'(\theta)} - \frac{1}{\gamma'(\theta)}\right)\right)^2 + y^2(\theta)\right] \\ &- 2\gamma'(\theta)\left[x(\theta) - \left(\frac{1}{\alpha'(\theta)} - \frac{1}{\gamma'(\theta)}\right)\right]\end{aligned} \tag{A.13}$$

Note the following relationship:

$$\frac{1}{\alpha'(\theta)} - \frac{1}{\gamma'(\theta)} = \frac{1}{\alpha_0(\theta)} - \frac{1}{\gamma_0(\theta)} = -\frac{\beta_0}{|G_o(e^{j\theta})|^2} \tag{A.14}$$

From Eq. (A.12) it follows that

$$\frac{2}{\gamma_0(\theta)}\left(x(\theta) + \frac{\beta_0}{|G_o(e^{j\theta})|^2}\right) > \left(x(\theta) + \frac{\beta_0}{|G_o(e^{j\theta})|^2}\right)^2 + y^2(\theta) \tag{A.15}$$

Substituting Eq. (A.15) into Eq. (A.13) and knowing that $0 < \gamma'(\theta) < \gamma_0(\theta) \leq 1$

leads to Eq. (A.16) as shown in the next page. Therefore, $\mathrm{CR}'(\theta) < 0$ is true for any $\theta \in [0, 2\pi]$. This completes the proof of the argument that if the modeling error $U_e(z)$ can be tolerated with certain λ and β values, NO-ILC has RMC at least for the same $U_e(z)$ with a larger λ value.

$$\mathrm{CR}'(\theta) < \left[\left(x(\theta) + \frac{\beta_0}{|G_o(e^{j\theta})|^2}\right)^2 + y^2(\theta)\right]\gamma'(\theta)(\gamma'(\theta) - \gamma_0(\theta)) < 0, \forall\theta \in [0, 2\pi] \tag{A.16}$$

Reconsider $\mathrm{CR}_0(\theta)$ in Eq. (A.11); it can be re-written as

$$\mathrm{CR}_0(\theta) = \gamma_0^2(\theta)\left(x^2(\theta) + y^2(\theta)\right) - 2\frac{\gamma_0^2(\theta)}{\alpha_0(\theta)}x + \frac{\gamma_0^2(\theta)}{\alpha_0^2(\theta)} - 1 \tag{A.17}$$

If β_0 is increased to β' but λ_0 retains its value, the RMC criterion becomes the following, for all $\theta \in [0, 2\pi]$

$$\mathrm{CR}'(\theta) = (\gamma'(\theta))^2\left(x^2(\theta) + y^2(\theta)\right) - 2\frac{(\gamma'(\theta))^2}{\alpha_0(\theta)}x + \left(\frac{\gamma'(\theta)}{\alpha_0(\theta)}\right)^2 < 1 \tag{A.18}$$

Subtracting $\mathrm{CR}'(\theta)$ from $\mathrm{CR}_0(\theta)$ gives:

$$\mathrm{CR}'(\theta) - \mathrm{CR}_0(\theta) = \left(\left(\frac{\gamma'(\theta)}{\gamma_0(\theta)}\right)^2 - 1\right)(\mathrm{CR}_0(\theta) + 1) \tag{A.19}$$

Because $\mathrm{CR}_0(\theta) \in (-1, 0)$, the inequality $\mathrm{CR}'(\theta) < \mathrm{CR}_0(\theta) < 0$ is true for any $\theta \in [0, 2\pi]$. This completes the proof of the argument that if the modeling error $U_e(z)$ can be tolerated with certain λ and β values, NO-ILC still has RMC at least for the same $U_e(z)$ with a larger β value.

Note that it has been proved that:

- Increasing λ and retaining β will not degrade the RMC region.
- Increasing β and retaining λ will not degrade the RMC region.

If both λ and β are increased from λ_0 and β_0, the following statement follows immediately from the two statements above:

- Increasing both λ and β will not degrade the RMC region.

Combining the above three statements completes the proof. □

Proof of Lemma IV.6:

Proof. If $U_e\left(e^{\theta}\right)$ lies inside the RMC disk for all $\theta \in [0, 2\pi]$, this means Eq. (4.10) is valid. After some manipulations Eq. (4.10) leads to Eq. (A.20) for all $\theta \in [0, 2\pi]$. Since the terms T_2 and T_3 are positive, the term T_1 must be negative, which translates to Criterion (4.1) after plugging in the definition of $x(\theta)$, $y(\theta)$, $\alpha(\theta)$ and $\gamma(\theta)$.

$$T_1 + T_2 + T_3 < 0, \quad \forall \theta \in [0, 2\pi]$$

$$T_1 = \left[x(\theta) - \left(\frac{1}{\alpha(\theta)} - \frac{1}{\gamma(\theta)}\right)\right]^2 - \frac{2}{\gamma(\theta)}\left[x(\theta) - \left(\frac{1}{\alpha(\theta)} - \frac{1}{\gamma(\theta)}\right)\right] + y^2(\theta)$$

$$T_2 = \left[\left(\frac{1}{a} - \frac{1}{q}\right) - \left(\frac{1}{\alpha(\theta)} - \frac{1}{\gamma(\theta)}\right)\right]\left[\frac{2}{\gamma(\theta)} - \left(\frac{1}{\alpha(\theta)} - \frac{1}{\gamma(\theta)}\right) - \left(\frac{1}{a} - \frac{1}{q}\right)\right]$$

$$T_3 = \left[x(\theta) - \left(\frac{1}{a} - \frac{1}{q}\right)\right]\left(\frac{2}{\alpha(\theta)} - \frac{2}{a}\right) \quad \text{(A.20)}$$

The above analysis shows that Eq. (4.10) is a sufficient condition for Criterion (4.1). In addition, as per the discussion after Eq. (4.10), either a larger λ or a larger β value enlarges the RMC region, but in a different manner. Hence, using $\lambda' > \lambda_0$ or $\beta' > \beta_0$ would enlarge the RMC region. □

Proof of Proposition V.1:

Proof. Note that $\mathrm{RB}^{-1}(\theta)$ equals to $\left|G_o\left(e^{j\theta}\right)\mathcal{L}\left(e^{j\theta}\right)\right|$, which is the length of the red vector in Fig. 5.6. It is also easy to see that the length of the blue vector in Fig. 5.6 equals to the value of convergence ratio $\mathrm{CR}(\theta)$. From geometry, the following equation is true:

$$\left|G_o\left(e^{j\theta}\right)\mathcal{L}\left(e^{j\theta}\right)\right| + \left|1 - G_o\left(e^{j\theta}\right)\mathcal{L}\left(e^{j\theta}\right)\right| \geq 1, \forall\theta \in [0, 2\pi) \tag{A.21}$$

since the shortest distance between the two points in Fig. 5.6, (0,0) and (1,0), is the line that directly connects them, whose length is 1. The above inequality can be re-written into:

$$\frac{1}{\mathrm{RB}(\theta)} + \mathrm{CR}(\theta) \geq 1, \quad \forall\theta \in [0, 2\pi) \tag{A.22}$$

Substituting Eq. (5.20) into the above equation gives Eq. (5.21). This is completes the proof. □

Proof of Proposition V.2:

Proof. For simplicity, the $\left(e^{j\theta}\right)$ term will be omitted in the proof, i.e., $\mathcal{Q}$ and $G_o\mathcal{L}$ are used to denote $\mathcal{Q}\left(e^{j\theta}\right)$ and $G_o\left(e^{j\theta}\right)\mathcal{L}\left(e^{j\theta}\right)$. Note that the following relationship is true:

$$1 - |\mathcal{Q} - G_o\mathcal{L}| \leq |1 - (\mathcal{Q} - G_o\mathcal{L})|, \quad \forall\theta \in [0, 2\pi] \tag{A.23}$$

For a monotonic convergent ILC updating law, $|\mathcal{Q} - G_o\mathcal{L}| < 1$ for all $\theta \in [0, 2\pi]$. Therefore, the following is true:

$$\frac{1}{1 - |\mathcal{Q} - G_o\mathcal{L}|} \geq \frac{1}{|1 - (\mathcal{Q} - G_o\mathcal{L})|}, \quad \forall\theta \in [0, 2\pi] \tag{A.24}$$

Multiplying both sides by $|G_o\mathcal{L}|$ gives the following inequality for all $\theta \in [0, 2\pi]$:

$$\frac{|G_o\mathcal{L}|}{1 - |\mathcal{Q} - G_o\mathcal{L}|} \geq \frac{|G_o\mathcal{L}|}{|1 - \mathcal{Q} + G_o\mathcal{L}|} = \left|\frac{G_o\mathcal{L}}{1 - \mathcal{Q} + G_o\mathcal{L}}\right| \tag{A.25}$$

Adding SSE(θ), Eq. (5.27), to both sides of the above inequality gives:

$$\begin{aligned}\left|\frac{1 - \mathcal{Q}}{1 - \mathcal{Q} + G_o\mathcal{L}}\right| + \frac{|G_o\mathcal{L}|}{1 - |\mathcal{Q} + G_o\mathcal{L}|} \geq \\ \left|\frac{1 - \mathcal{Q}}{1 - \mathcal{Q} + G_o\mathcal{L}}\right| + \left|\frac{G_o\mathcal{L}}{1 - \mathcal{Q} + G_o\mathcal{L}}\right| \geq \\ \left|\frac{1 - \mathcal{Q} + G_o\mathcal{L}}{1 - \mathcal{Q} + G_o\mathcal{L}}\right| = 1\end{aligned} \tag{A.26}$$

Since $\mathrm{RB}^{-1}(\theta) = |G_o\mathcal{L}|$ and $\mathrm{CS}(\theta) = 1 - |\mathcal{Q} - G_o\mathcal{L}|$ according to their definitions Eq. (5.26), the above inequality can be re-written as Eq. (5.28). This is completes the proof. □

BIBLIOGRAPHY

BIBLIOGRAPHY

Ahn, H. S., K. Moore, and Y. Chen (2005), Schur stability radius bounds for robust iterative learning controller design, American Control Conference, pp. 178–183.

Ahn, H. S., Y. Chen, and K. L. Moore (2007a), Iterative learning control: brief survey and categorization., *IEEE Transactions on Systems Man and Cybernetics Part C Applications and Reviews*, *37*(6), 1099–1121.

Ahn, H. S., K. L. Moore, and Y. Chen (2007b), Stability analysis of discrete-time iterative learning control systems with interval uncertainty, *Automatica*, *43*(5), 892–902.

Ahn, H. S., K. L. Moore, and Y. Q. Chen (2007c), *Iterative learning control: robustness and monotonic convergence for interval systems*, Springer.

Altin, B., and K. Barton (2015), Learning control of linear iteration varying systems with varying references through robust invariant update laws, American Control Conference, pp. 4880–4885.

Amann, N., D. H. Owens, and E. Rogers (1996), Iterative learning control for discrete-time systems with exponential rate of convergence, *IEE Proceedings-Control Theory and Applications*, *143*(2), 217–224.

Arimoto, S., S. Kawamura, and F. Miyazaki (1984), Bettering operation of robots by learning, *Journal of Robotic systems*, *1*(2), 123–140.

Barton, K. L., and A. G. Alleyne (2008), A cross-coupled iterative learning control design for precision motion control, *IEEE Transactions on Control Systems Technology*, *16*(6), 1218–1231.

Barton, K. L., and A. G. Alleyne (2011), A norm optimal approach to time-varying ILC with application to a multi-axis robotic testbedl, *IEEE Transactions on Control Systems Technology*, *19*(1), 166–180.

Barton, K. L., D. J. Hoelzle, A. G. Alleyne, and A. J. W. Johnson (2011), Cross-coupled iterative learning control of systems with dissimilar dynamics: design and implementation, *International Journal of Control*, *84*(7), 1223–1233.

Bien, Z., and K. M. Huh (1989), Higher-order iterative learning control algorithm, pp. 105–112.

Bien, Z., and J. X. Xu (2012), *Iterative learning control: analysis, design, integration and applications*, Springer.

Bouakrif, F. (2011), Iterative learning control for strictly unknown nonlinear systems subject to external disturbances, *International Journal of Control, Automation and Systems*, *9*(4), 642.

Bouakrif, F., D. Boukhetala, and F. Boudjema (2013), Velocity observer-based iterative learning control for robot manipulators, *International Journal of Systems Science*, *44*(2), 214–222.

Bristow, D. A. (2008), Weighting matrix design for robust monotonic convergence in norm optimal iterative learning control, American Control Conference, pp. 4554–4560.

Bristow, D. A., and A. Alleyne (2006), A high precision motion control system with application to microscale robotic deposition, *IEEE Transactions on Control Systems Technology*, *16*(6), 1008–1020.

Bristow, D. A., M. Tharayil, and A. G. Alleyne (2006), A survey of iterative learning control: A learning-based method for high-performance tracking control, *IEEE Control Systems Magazine*, *26*(3), 96–114.

Chen, Y., and K. L. Moore (2002a), An optimal design of PD-type iterative learning control with monotonic convergencel, Proceedings of International Symposium on Intelligent Control, pp. 55–60.

Chen, Y., and K. L. Moore (2002b), Harnessing the nonrepetitiveness in iterative learning control, Conference on Decision and Control, pp. 3350–3355.

Chen, Y., Z. Gong, and C. Wen (1998), "Analysis of a high-order iterative learning control algorithm for uncertain nonlinear systems with state delays, *34*(3), 345–353.

Chi, R., Z. Hou, and J. X. Xu (2008), Adaptive ILC for a class of discrete-time systems with iteration-varying trajectory and random initial condition, *Automatica*, *44*(8), 2207–2213.

Chien, C. J., and C. Y. Yao (2004), Iterative learning of model reference adaptive controller for uncertain nonlinear systems with only output measurement, *Automatica*, *40*(5), 855–864.

Chien, C. J., Z. Hou, and J. X. Xu (2008), A combined adaptive law for fuzzy iterative learning control of nonlinear systems with varying control tasks, *IEEE Transactions on Fuzzy Systems*, *16*(1), 40–51.

Choi, J. Y., and J. S. Lee (2000), Adaptive iterative learning control of uncertain robotic systems, *IEE Proceedings-Control Theory and Applications*, *147*(2), 217–223.

Cichy, B., K. Gakowski, E. Rogers, and A. Kummert (2011), An approach to iterative learning control for spatio-temporal dynamics using nD discrete linear systems models, Multidimensional Systems and Signal Processing, pp. 83–96.

Cichy, B., K. Gakowski, and E. Rogers (2014), 2D systems based robust iterative learning control using noncausal finite-time interval data, *Systems & Control Letters*, *64*, 36–42.

De Roover, D., and O. H. Bosgra (2000), Synthesis of robust multivariable iterative learning controllers with application to a wafer stage motion system, *International Journal of Control*, *73*(10), 968–979.

Donkers, T., J. Van De Wijdeven, and O. Bosgra (2008), Robustness against model uncertainties of norm optimal iterative learning control, American Control Conference, pp. 4561–4566.

Ersal, T., M. Brudnak, A. Salvi, Y. Kim, J. B. Siegel, and J. L. Stein (2014), An iterative learning control approach to improving fidelity in Internet-Distributed Hardware-in-the-Loop Simulation, *Journal of Dynamic Systems, Measurement, and Control*, *136*(6), 061,012.

French, M., and E. Rogers (2000), Non-linear iterative learning by an adaptive Lyapunov technique, *International Journal of Control*, *73*(10), 840–850.

Freudenberg, J., and D. Looze (1985), Right half plane poles and zeros and design tradeoffs in feedback systems, *IEEE Transactions on Automatic Control*, *30*(6), 555–565.

Gao, X., and S. Mishra (2014), An iterative learning control algorithm for portability between trajectories, American Control Conference, pp. 3808–3813.

Ge, X., M. J. Brudnak, J. L. Stein, and T. Ersal (2014), A norm optimal iterative learning control framework towards Internet-Distributed Hardware-in-the-Loop simulation, American Control Conference, pp. 3802–3807.

Ge, X., J. L. Stein, and T. Ersal (2016a), A frequency domain approach for designing filters for norm-optimal iterative learning control and its fundamental tradeoff between robustness, convergence speed and steady state error, American Control Conference, pp. 384–391.

Ge, X., J. L. Stein, and T. Ersal (2016b), Optimization based weighting matrices design for norm optimal iterative learning control, Dynamics Systems and Control Conference.

Ge, X., J. L. Stein, and T. Ersal (2017a), Frequency domain analysis of robust monotonic convergence of norm-optimal iterative learning control, *IEEE Transactions on Control System Technology*, *accepted*.

Ge, X., J. L. Stein, and T. Ersal (2017b), A frequency-dependent filter design approach for norm-optimal iterative learning control and its fundamental trade-off between robustness, convergence speed and steady state error, *ASME Journal of Dynamic Systems, Measurement and Control*, *submitted*.

Ge, X., J. L. Stein, and T. Ersal (2017c), Optimization based weighting matrices design for norm optimal iterative learning control, *IEEE Transactions on Control System Technology*, *to be submitted*.

Ge, X., J. L. Stein, and T. Ersal (2017d), Optimality of norm-optimal iterative learning control, *ASME Journal of Dynamic Systems, Measurement and Control*, *to be submitted*.

Goldsmith, P. B. (2002), On the equivalence of causal LTI iterative learning control and feedback control, *Automatica*, *38*(4), 703–708.

Gorinevsky, D. (2002), Loop shaping for iterative control of batch processes, *IEEE Control Systems Magazine*, *22*(6), 55–65.

Gunnarsson, S., and M. Norrlof (2001), On the design of ILC algorithms using optimization, *Automatica*, *37*(12), 2011–2016.

Harte, T. J., J. Hatonen, and D. H. Owens (2005), Discrete-time inverse model-based iterative learning control: stability, monotonicity and robustness, *International Journal of Control*, *78*(8), 577–586.

Hatonen, J., D. H. Owens, and K. Feng (2006), Basis functions and parameter optimisation in high-order iterative learning control, *Automatica*, *42*(2), 297–294.

Heinzinger, G., D. Fenwick, D. Paden, and F. Miyazaki (1992), Stability of learning control with disturbances and uncertain initial conditions, *IEEE Transactions on Automatic Controll*, *37*(1), 110–114.

Hladowski, L., K. Galkowski, Z. Cai, E. Rogers, C. T. Freeman, and P. L. Lewin (2010), Experimentally supported 2D systems based iterative learning control law design for error convergence and performance, *Control Engineering Practice*, *18*(4), 339–348.

Janssens, P., G. Pipeleers, and J. Swevers (2013), A data-driven constrained norm-optimal iterative learning control framework for LTI systems, *IEEE Transactions on Control Systems Technology*, *21*(2), 546–157.

Kurek, J. E., and M. B. Zaremba (1993), Iterative learning control synthesis based on 2-D system theory, *IEEE Transactions on Automatic control*, *38*(1), 121–125.

Lee, J. H., and K. S. Lee (2007), Iterative learning control applied to batch processes: an overview, *Control Engineering Practice*, *15*(10), 1306–1318.

Lee, J. H., K. S. Lee, and W. C. Kim (2000), Model-based iterative learning control with a quadratic criterion for time-varying linear systems, *Automatica*, *36*(5), 647–657.

Lee, K. S., W. C. Kim, and J. H. Lee (1996), Model-based iterative learning control with a quadratic criterion of linear batch process, *Journal of Control, Robotics and Systems*, *2*(3), 148–157.

Li, Y., Y. Q. Chen, H. S. Ahn, and G. Tian (2013), A survey on fractional-order iterative learning control, *Journal of Optimization Theory and Applications*, *151*(1), 127–140.

Liu, C., J. Xu, and J. Wu (2009a), Iterative learning control for network systems with communication delay or data dropout, IEEE Conference on Decision and Control, pp. 4858–4863.

Liu, C., J. Xu, J. Wu, and Y. Tan (2009b), On iterative learning control with high-order internal models, IEEE International Conference on Control and Automation, pp. 1565–1570.

Longman, R. W. (2000), Iterative learning control and repetitive control for engineering practice, *International Journal of Control*, *73*(10), 930–954.

Madady, A. (2008), PID type iterative learning control with optimal gains, *International Journal of Control, Automation, and Systems*, *6*(2), 194–203.

Mishra, S., J. Coaplen, and M. Tomizuka (2007), Precision positioning of wafer scanners segmented iterative learning control for nonrepetitive disturbances, *IEEE control systems*, *27*(4), 20–25.

Moore, K. L., and Y. Chen (2002), On monotonic convergence of high order iterative learning update laws, IFAC Proceedings Volumes, pp. 19–24.

Moore, K. L., M. Ghosh, and Y. Q. Chen (2007), Spatial-based iterative learning control for motion control applications, *Meccanica*, *42*(2), 167–175.

Norrlof, M. (2002), An adaptive iterative learning control algorithm with experiments on an industrial robot, *IEEE Transactions on Robotics and Automation*, *18*(2), 245–251.

Norrlof, M., and S. Gunnarsson (2002a), Time and frequency domain convergence properties in iterative learning control, *International Journal of Control*, *75*(14), 1114–1126.

Norrlof, M., and S. Gunnarsson (2002b), Disturbance aspects of high order iterative learning control, pp. 13–18.

Norrlof, M., and S. Gunnarsson (2005), A note on causal and CITE iterative learning control algorithms, *Automatica*, *41*(2), 345–350.

Oh, S. R., Z. Bien, and I. H. Suh (1988), An iterative learning control method with application to robot manipulators, *IEEE Journal on Robotics and Automation*, *4*(5), 508–514.

Owens, D. H. (2016), *Iterative learning control*, Springer London.

Owens, D. H., and S. Daley (2008), Iterative learning control - Monotonicity and optimization, *International Journal of Applied Mathematics and Computer Science*, *18*(3), 279–293.

Owens, D. H., and K. Feng (2006), Parameter optimization in iterative learning control, *International Journal of Control*, *76*(11), 1059–1069.

Owens, D. H., N. Amann, E. Rogers, and M. French (2000), Analysis of linear iterative learning control schemes-a 2D systems/repetitive processes approach, *Multidimensional Systems and Signal Processing*, *11*(1-2), 125–177.

Owens, D. H., J. Hatonen, and S. Daley (2009), Robust monotone gradient-based discrete-time iterative learning control, *International Journal of Robust and Nonlinear Control*, *19*(6), 634–661.

Pan, Y. J., H. J. Marquez, and T. Chen (2006), Sampled data iterative learning control for a class of non-linear networked control systems, American Control Conference, p. 6.

Phan, M. Q., and R. W. Longman (2002), Higher-order iterative learning control by pole placement and noise filtering, IFAC Proceedings Volumes, pp. 25–30.

Sahoo, S. K., S. K. Panda, and J. X. Xu (2007), Application of spatial iterative learning control for direct torque control of switched reluctance motor drive, Power Engineering Society General Meeting, pp. 1–7.

Shi, J., F. Gao, and T. J. Wu (2005), Robust design of integrated feedback and iterative learning control of a batch process based on a 2D Roesser system, *Journal of Process Control*, *15*(8), 907–924.

Sun, M., and D. Wang (2001), Initial condition issues on iterative learning control for non-linear systems with time delayl, *International Journal of Systems Science*, *32*(11), 1365–1375.

Sun, M., and D. Wang (2003), Initial shift issues on discrete-time iterative learning control with system relative degree, *IEEE Transactions on Automatic Control*, *48*(1), 144–148.

Tayebi, A. (2004), Adaptive iterative learning control for robot manipulators, *Automatica*, *40*(7), 1195–1203.

Van De Wijdeven, J., T. Donkers, and O. Bosgra (2009), Iterative learning control for uncertain systems: robust monotonic convergence analysis, *Automatica*, *45*(10), 2383–2391.

Van Zundert, J., J. Bolder, and T. Oomen (2015), Iterative learning control for varying tasks: Achieving optimality for rational basis functions, American Control Conference, pp. 3570–3575.

Wang, D. (1998), Convergence and robustness of discrete time nonlinear systems with iterative learning control, *Automatica*, *34*(11), 1445–1448.

Wang, Y., F. Gao, and F. J. Doyle (2009), Survey on iterative learning control, repetitive control, and run-to-run control, *Journal of Process Control*, *19*(10), 1589–1600.

Wang, Y. C., C. J. Chien, and C. C. Teng (2004), Direct adaptive iterative learning control of nonlinear systems using an output-recurrent fuzzy neural network, *IEEE Transactions on Systems, Man, and Cybernetics, Part B*, *34*(3), 1348–1359.

Xu, J. X. (1997), Analysis of iterative learning control for a class of nonlinear discrete-time systems, *Automatica*, *33*(10), 1905–1907.

Xu, J. X. (2011), A survey on iterative learning control for nonlinear systems, *International Journal of Controls*, *84*(7), 1275–1294.

Xu, J. X., and Y. Tan (2003), *Linear and nonlinear iterative learning control*, Springer.

Xu, J. X., and J. Xu (2004), On iterative learning from different tracking tasks in the presence of time-varying uncertainties, *IEEE Transactions on Systems, Man, and Cybernetics, Part B (Cybernetics)*, *34*(1), 589–597.

Xu, J. X., and R. Yan (2005), On initial conditions in iterative learning control, *IEEE Transactions on Automatic Control*, *50*(9), 1349–1354.

Xu, J. X., S. K. Panda, and T. H. Lee (2007), *Real-time iterative learning control: design and applications*, Springer.

Yin, C., J. X. Xu, and Z. Hou (2010), A high-order internal model based iterative learning control scheme for nonlinear systems with time-iteration-varying parameters, *IEEE Transactions on Automatic Control*, *55*(11), 2665–2670.